

**Vortex states in
superconducting/ferromagnetic hybrid
systems**

Dissertation

zur Erlangung des Doktorgrades der Naturwissenschaften
(Dr. rer. nat.)

der

Naturwissenschaftlichen Fakultät II
Chemie, Physik und Mathematik

der Martin-Luther-Universität
Halle-Wittenberg

vorgelegt von

Herrn Björn Niedzielski

Gutachter:

1. Prof. Dr. Jamal Berakdar
2. Prof. Dr. Steffen Trimper
3. Prof. Dr. habil. Maciej Krawczyk

Datum der öffentlichen Verteidigung: 28.11.2023

Contents

| | |
|--|-----------|
| Abbreviations and Notations | v |
| 1 Introduction | 1 |
| 2 Theoretical background | 5 |
| 2.1 London theory | 5 |
| 2.2 Ginzburg-Landau theory | 7 |
| 2.3 Type-II superconductors | 11 |
| 2.3.1 Structure of a vortex | 13 |
| 2.3.2 Field of a vortex | 15 |
| 2.4 Time-dependent Ginzburg-Landau theory | 18 |
| 2.5 Validity of the Ginzburg-Landau theory | 20 |
| 2.6 Micromagnetism | 22 |
| 2.6.1 Exchange interaction | 22 |
| 2.6.2 Magnetic anisotropy | 23 |
| 2.6.3 Zeeman energy | 24 |
| 2.6.4 Magnetostatic self-energy | 24 |
| 2.6.5 Landau-Lifschitz-Gilbert equation | 25 |
| 2.6.6 Spin waves | 26 |
| 3 Numerical procedure | 29 |
| 4 Controlled vortex formation at nanostructured superconductor/ferromagnetic junctions | 32 |
| 4.1 Simulation details | 33 |
| 4.2 Results and discussion | 35 |
| 5 Supercurrent induced by chiral coupling in multiferroic/superconductor nanostructures | 42 |
| 5.1 Methods | 43 |
| 5.2 Results | 46 |
| 5.2.1 Vortex dynamics for zero SOC | 46 |
| 5.2.2 Vortex dynamics in the presence of SOC | 47 |
| 6 Magnon-fluxon interaction in coupled superconductor/ferromagnet hybrid systems | 55 |
| 6.1 Methods | 55 |
| 6.2 Results and discussion | 58 |
| 6.3 Effect of the thickness of the wave guide | 60 |

| | | |
|----------|---|------------|
| 6.4 | Disordered vortex lattice | 63 |
| 6.4.1 | Variations in field strength | 63 |
| 6.4.2 | Variations in field position | 65 |
| 6.5 | Summary and comparison with experiment | 69 |
| 7 | Temperature-driven vortex dynamics | 70 |
| 7.1 | Setup | 70 |
| 7.2 | Results | 72 |
| 7.2.1 | Temperature induced vortex motion | 72 |
| 7.2.2 | Current induced vortex motion | 74 |
| 7.2.3 | Temperature induced vortex motion – interpretation in terms of electric potentials | 77 |
| 7.3 | Outlook | 81 |
| 8 | Summary and outlook | 82 |
| | Bibliography | 86 |
| | Curriculum Vitae | 105 |
| | List of Publications | 106 |
| | Acknowledgements | 107 |
| | Eidesstattliche Erklärung | 109 |

List of Figures

| | | |
|-----|---|----|
| 2.1 | Spatial profile of an isolated vortex | 15 |
| 2.2 | Schematic of supercurrent flow in a thin film of arbitrary shape | 16 |
| 2.3 | Damped precessional motion of a magnetic moment on the Bloch sphere . | 26 |
| 2.4 | Schematic of spin wave propagation in a waveguide of backward volume magnetostatic spin wave configuration | 27 |
| 4.1 | Setup of a FM/SC hybrid system in free space with open boundary conditions for the stray fields | 34 |
| 4.2 | Equilibrium state of a FM/SC bilayer where the FM consists of two domains of opposite magnetization direction | 36 |
| 4.3 | Equilibrium state of a FM/SC bilayer where the FM consists of four domains of opposite magnetization direction | 38 |
| 4.4 | FM/SC bilayer-system with a ferromagnetic bottom layer of side length $a = 1\mu\text{m}$ and a rotation of 45° with respect to the superconducting top layer | 39 |
| 4.5 | Vortex arrangement in a quadratic SC under uniform external field | 40 |
| 4.6 | Combined effect of magnetic stray fields and external magnetic field on a quadratic SC | 41 |
| 5.1 | Setup for the investigation of SOC-induced vortex pinning in a multiferroic/SC bilayer | 43 |
| 5.2 | Time evolution of current-driven vortices in a quadratic thin film | 47 |
| 5.3 | Mean voltage versus winding number in a proximity-coupled multiferroic/SC bilayer. Influence of different magnetic textures on the vortex dynamics | 49 |
| 5.4 | Mean voltage versus phase shift φ of the spin spiral in a proximity-coupled multiferroic/SC bilayer | 50 |
| 5.5 | Depinning current versus winding number in a proximity-coupled multiferroic/SC bilayer | 51 |
| 5.6 | Spatial profile of the SOC-induced supercurrent density in a proximity-coupled multiferroic/SC bilayer | 52 |
| 5.7 | Anisotropy of the current transport in a proximity-coupled multiferroic/SC bilayer | 53 |
| 6.1 | Schematic of a FM/SC bilayer for the investigation of magnon-fluxon interaction | 56 |
| 6.2 | Comparison between the stray field of a regular Abrikosov lattice and the field of an arrangement of ferromagnetic nanocubes | 57 |
| 6.3 | Magnonic dispersion modulated by the stray field of a superconducting vortex lattice | 59 |

| | | |
|------|--|----|
| 6.4 | Magnonic dispersion under the influence of an artificial vortex lattice . . . | 60 |
| 6.5 | Dependence of the magnonic dispersion on the wave guide thickness . . . | 61 |
| 6.6 | Dependence of the magnonic dispersion on the wave guide thickness (logarithmic color scale) | 62 |
| 6.7 | Setup to investigate effects of an imperfect vortex lattice on the magnonic dispersion. | 64 |
| 6.8 | Band diagram and magnonic modes under a perfectly structured vortex lattice | 66 |
| 6.9 | Band diagram and magnonic modes under a disordered vortex lattice. Disorder is introduced by randomizing the field amplitudes of individual vortices | 67 |
| 6.10 | Band diagram and magnonic modes under a disordered vortex lattice. Disorder is introduced by randomizing the position of individual vortices . | 68 |
| 7.1 | Setup for the investigation of temperature-induced vortex motion | 71 |
| 7.2 | Deflection of a vortex due to a nearby hot spot | 73 |
| 7.3 | Time dependent deflection of a vortex due to an external current | 75 |
| 7.4 | Time evolution of the electric potentials ϕ_1 , ϕ_2 and ϕ_{tot} due to an external current | 76 |
| 7.5 | Time evolution of the electric potentials ϕ_1 , ϕ_2 and ϕ_{tot} due to a nearby hot spot | 77 |
| 7.6 | Dependence of the temperature driven vortex deflection on the sample width | 80 |

Abbreviations and Notations

| | |
|-------|---|
| SC | Superconductor |
| FM | Ferromagnet |
| SOC | Spin-Orbit-Coupling |
| GL | Ginzburg-Landau |
| TDGL | Time-dependent Ginzburg-Landau |
| LLG | Landau-Lifshitz-Gilbert |
| BCS | Bardeen-Cooper-Schrieffer |
| FEM | Finite Element Method |
| VAV | Vortex-Antivortex |
| FFT | Fast Fourier Transform |
| BZ | Brillouin Zone |
| BVMSW | Backward volume magnetostatic spin wave |

Latin Letters

| | |
|------------------|--|
| T_c | Critical temperature of the superconductor |
| T_0 | Constant temperature at which the superconductor is held |
| \bar{t} | reduced temperature |
| B_{cth} | Thermodynamic critical field |
| m_s | Mass of a Cooper pair |
| q_s | Charge of a Cooper pair |
| n_s | Cooper pair density |
| \mathbf{j}_s | Supercurrent density |
| \mathbf{j}_e | Density of an external electric current |
| \mathbf{v}_s | Superfluid velocity |
| v_f | Fermi velocity |

| | |
|---------------------------|--|
| l | Electronic mean free path |
| \mathbf{A}_s | Magnetic vector potential of the superconductor |
| \mathbf{A}_{FM} | Magnetic vector potential of the ferromagnet |
| \mathbf{A}_e | Vector potential of the external magnetic field |
| \mathbf{B}_s | Magnetic flux density of the superconductor |
| \mathbf{B}_{FM} | Magnetic flux density of the ferromagnet |
| \mathbf{H}_e | External magnetic field |
| \mathbf{B}_e | Magnetic flux density of the external magnetic field |
| \mathbf{B}_v | Magnetic flux density associated with a superconducting vortex lattice |
| \mathbf{B}_{SOC} | Magnetic flux density associated with interfacial Rashba spin-orbit coupling |
| A | Exchange constant |
| \mathbf{n} | Surface normal |
| n | scaling parameter |
| M_s | Saturation magnetization |
| \mathbf{m} | Normalized magnetization |
| m | winding number of the spin spiral of TbMnO_3 |
| D | Diffusion coefficient |
| $\hat{\mathbf{D}}$ | Kinetic momentum operator |
| a_{VL} | Lattice parameter of the Abrikosov vortex lattice |
| $\langle U \rangle_{x,y}$ | Mean voltage across the superconducting sample |
| \mathbf{F}_L | Lorentz force acting on a superconducting vortex |

Greek Letters

| | |
|-----------------------|--|
| α | Temperature dependent Ginzburg-Landau coefficient |
| α_s | Spin-orbit parameter |
| β | Constant Ginzburg-Landau coefficient |
| Ψ | Macroscopic wave function |
| Ψ^* | Complex conjugate of the macroscopic wave function |
| Ψ_0 | Amplitude of the macroscopic wave function |
| θ | Phase of the macroscopic wave function |
| λ_{GL} | Ginzburg-Landau penetration depth |
| λ_{L} | London penetration depth |
| ξ_{GL} | Ginzburg-Landau coherence length |
| ξ_0 | BCS coherence length |
| κ | Ginzburg-Landau parameter |
| ϕ | Electric scalar potential |
| Φ | Magnetic flux |
| Φ_0 | Magnetic flux quantum |
| σ | Electrical conductivity |
| Ω | Sample volume |
| $\partial\Omega$ | Boundary of the sample volume |
| Γ | Magnetic damping coefficient |
| γ | Gyromagnetic ratio |
| μ_0 | Vacuum permeability |
| $\eta_{1,2,3}$ | Scaling parameters |

1 Introduction

The property of an electrical conductor to carry electric current without Ohmic resistance and Joule heating is called superconductivity. It is a state of matter that arises in many elemental metals and alloys at temperatures close to absolute zero. From a technological point of view, superconductivity is highly interesting, with excellent potential for energy-efficient and innovative future applications. However, the need for cryogenic cooling, expensive fabrication costs, and a lack of understanding of the underlying physical processes are severe obstacles for industrial mass production of superconducting technology.

This research aims at investigating the behavior of so-called type-II superconductors (SCs) in confined nanosystems and in close vicinity to ferromagnetic materials. Of particular interest are the dynamics of superconducting vortices – whirls of supercurrent that arise in SCs in the presence of magnetic fields. The behavior of vortices is crucial for the electromagnetic properties of the SC and hence for the efficiency of superconducting devices. In this work, it is investigated how these topologically protected current whirls behave in confined nanostructures and how their interaction with a nearby ferromagnet (FM) can be utilized to control the information transfer through FM/SC hybrid systems. Additionally, some problems of fundamental interest will be addressed as well, e.g., spin-orbit-coupling (SOC) induced vortex pinning and vortex motion in the presence of temperature gradients.

Superconductivity in ultracold electric conductors is a phenomenon that has been known for over one hundred years. It was first discovered in 1911 by Heike Kamerlingh Onnes, a pioneer in the field of cryogenic gases, who observed a sudden disappearance of electrical resistance in mercury as the material is cooled to temperatures below 4.2 K [1]. Onnes immediately saw the potential of his discovery, and it did not take long to realize that the phenomenon, which he called "superconductivity", was not unique to mercury. In fact, the so-called critical temperature T_c at which the conductor loses electrical resistance turned out to be a material constant, and superconductivity was confirmed for many elemental metals. Moreover, in 1933 It was found by W. Meißner and R. Ochsenfeld that SCs are not only perfect conductors but also perfect diamagnets, which means they expel magnetic fields completely from their interior [2].

The discovery of the Meißner-Ochsenfeld effect, often called the Meißner effect, was an important milestone on the way to a better understanding of superconductivity. In particular, it was found that the perfect expulsion of magnetic fields is not a mere consequence of perfect conductivity, as one would expect from classical electrodynamics. The Meißner effect appears, irrespective of whether the material is cooled under an applied magnetic field or the field is applied after the superconducting transition. The final state is independent of the system's history, i.e., superconductivity is a distinct thermodynamic state. Experimentally, one finds that screening of SCs is limited, and a sufficiently strong field drives the material to the normal conducting state. The associated magnetic field

is called the thermodynamic critical field, and its temperature dependence can be well approximated by $H_{\text{cth}}(T) = H_{\text{cth}}(0)(1 - T/T_c)$. Strong electric currents have the same effect on the SC as H_{cth} , i.e., a critical current density j_c can destroy the superconducting state.

In 1935 the two brothers Fritz and Heinz London developed the first phenomenological theory, which was able to describe superconductivity's main aspects – zero electrical resistance and perfect diamagnetism [3]. In 1950 V. L. Ginzburg and L. D. Landau presented their own approach to the problem, the Ginzburg-Landau (GL) theory [4], which was later utilized by A. A. Abrikosov to predict the existence of type-II SCs [5]. Despite being a great success, the London theory and its generalizations did not provide insight into the microscopic processes of the phenomenon of superconductivity. It took another 22 years for the next breakthrough to happen. In 1957 J. Bardeen, L. Cooper, and J. Schrieffer developed the first microscopic theory explaining superconductivity in elemental metals [6]. The celebrated BCS theory is based on the idea that electrons form bound pairs, so-called Cooper pairs when the material is cooled below its critical temperature. The attractive interaction between the negatively charged electrons is mediated by vibrations of the atomic lattice, so-called phonons. Through their bosonic nature, all the Cooper pairs can occupy the same quantum state and form a pair-correlated condensate. This "macroscopic quantum state" can not be easily destroyed by scattering events between electrons and lattice atoms. For this reason, electric transport becomes effectively lossless. The validity of the BCS theory has been proven in many experiments [7–10], and the riddle of superconductivity seemed to be solved. However, in 1986 a new class of cuprate SCs was discovered with a critical temperature of about $T_c \approx 30$ K [11]. These high-temperature SCs possess a pair binding mechanism that differs from that of conventional BCS-SCs. For this reason, they are also called unconventional SCs. In the following years, more exotic SCs were found, e.g., heavy fermion SCs [12], Iron Pnictides [13], organic SCs [14] and spin-triplet SCs [15]. The microscopic origin of unconventional superconductivity is an open question until today (see, e.g., [16,17]). One of the most exciting discoveries of the last years was the appearance of superconductivity in various hydrogen-rich compounds. Under sufficient pressure, these materials can have very high critical temperatures of up to $T_c = 260$ K [18,19]. With this discovery, room-temperature superconductivity seems to be closer at hand than ever. Yet, there are still many problems to be solved until superconducting technology can become part of everyday life.

The development of highly energy-efficient, environment-friendly electric devices is the main goal of the superconducting industries. Magnetic resonance imaging, high-field magnets in particle accelerators, and SQUIDS (superconducting quantum interference devices) as ultra-sensitive magnetic field detectors are technologies that are already well established [20]. The ever-growing need for industrial know-how is followed by a rapidly evolving body of scientific literature ranging from fundamental research to device fabrication methods. Over the last decades, computer-based research has become more important than ever to solve the theoretical models of increasing complexity, evaluate large amounts of data, and find new superconducting materials [21]. Especially, large-scale simulations of mesoscopic SCs coupled with FMs are highly demanding and rarely to be found in the literature. Such systems are highly interesting since geometric confinement and the presence of a FM can lead to superconducting states that can not appear

under normal conditions [22–25]. On the other hand, the superconducting component can also be utilized to control the information transfer through the FM, making FM/SC hybrids attractive for applied research.

This theoretical study aims to provide novel ways to control and utilize superconducting vortices in electromagnetically coupled FM/SC bilayers. The main tools for this task will be the time-dependent Ginzburg-Landau (TDGL) equations of superconductivity and the Landau-Lifschitz-Gilbert (LLG) equation of micromagnetism. These equations are to be solved numerically and selfconsistently to simulate the FM/SC system under various conditions. Specifically, the following questions will be addressed:

- How can a structured FM be used to control superconducting vortices in confined nanosystems;
- How does interfacial Rashba SOC affect the vortex dynamics in a proximity-coupled FM/SC bilayer;
- How can the vortices be utilized to modify the magnonic information transfer through a FM/SC hybrid structure;
- How does local heating of the material affect nearby vortices.

Finding answers to these questions provides better insight into the rich physics of superconducting vortex matter – a subject that, despite being under investigation for over 50 years, is not fully understood yet. Also, applied research could benefit from the here-presented findings since all known high-T_c SCs are of type II. Controlling the vortex dynamics in these materials is crucial for the industrial mass production of energy-efficient, reliable, and inexpensive superconducting devices.

In this work, the focus lies on a phenomenological description of the SC and FM. That means the system constituents are characterized by appropriate macroscopic order parameters. In contrast, the microscopic processes that lead to the appearance of superconducting- and ferromagnetic order are not studied here. The use of a macroscopic model for FM/SC hybrids leads to results of quite general nature, valid for a large class of materials. However, this study is still restricted to s-wave SCs described by the conventional TDGL-formalism. The phenomenological description of exotic SCs requires using a generalized GL-model (e.g., [26]). In addition, the chosen theoretical framework is only valid within certain limits, which will be specified later. It should also be mentioned that, in most cases, the quality of the used samples is artificially high – most of the here-introduced systems consist of perfectly homogeneous materials without impurities or geometric deformations. Furthermore, only a limited number of selected material parameters is considered. In real materials, these parameters may vary, even between different samples of the same material [27]. Finally, research limitations are also set by the availability of computational resources entailing certain simplifications of the models to reduce computational effort. These simplifications and their impact on the results will be addressed in the main body of the text.

This thesis is organized as follows. Chapter 2 presents the theoretical framework for a mean-field description of the SC and FM. That includes an introduction to the TDGL theory and micromagnetism and a short review of the fundamental properties of SCs and FMs. Chapter 3 introduces the solution methods for the TDGL equations and the LLG

equation. The basic idea for calculating spin wave spectra of magnonic waveguides is also presented. Chapter 4 describes how vortices behave under geometrical confinement and in the vicinity of a patterned FM. Chapter 5 deals with the problem of proximity-induced supercurrent generation in coupled multiferroic/SC nanostructures. Chapter 6 addresses the third research question, i.e., how superconducting vortices can be utilized to modify the magnonic information transfer through FM/SC hybrid systems. The effect of a local hot spot on an isolated vortex is discussed in Chapter 7. Finally, Chapter 8 provides a summary of the obtained results.

2 Theoretical background

This section introduces two of the most commonly used theoretical models of superconductivity, namely the London theory and the GL theory. Both models are phenomenological in nature, which means they do not relate to the microscopic processes that lead to the formation of the superconducting state. Instead, superconductivity is described on a mesoscopic level and with the aid of conventional electrodynamics. Although the main tool for this research project will be the TDGL theory, it is worth introducing the London approach as well since it can be considered a precursor for the more advanced GL model. For computer simulations on systems of mesoscopic size, a phenomenological approach is advantageous since the use of microscopic theories becomes very involved. In addition, as already mentioned, in high-Tc materials, the microscopic origin of superconductivity is still not fully understood, and a complete microscopic theory is currently not existing for these materials. Furthermore, on a macroscopic scale, most known SCs behave very similarly under the influence of external magnetic fields. For this reason, the London theory and the GL equations are well-established and commonly used in various situations. Here only a rough overview of these models is given. For more information on the London theory and its extensions, see the standard literature, e.g., [28, 29].

2.1 London theory

The London theory was developed by F. London and H. London in 1935 [3]. It was the first successful attempt to formulate a model for the two most important phenomena connected with superconductivity - perfect diamagnetism and lossless current transport. Although the London brothers did not give a rigorous derivation of their equations, it is possible to obtain them from classical Drude theory. This simple model treats the conduction electrons as classical particles moving through the crystal lattice and scattering by collisions with the metal ions. Within this picture, the electrical response of a normal metal to an applied electric field can be formulated as a force-balance equation

$$m_e \frac{\partial \mathbf{v}}{\partial t} = q_e \mathbf{E} - \frac{m_e}{\tau} \mathbf{v}. \quad (2.1)$$

Here m_e and q_e are the mass and charge of an electron. The first term on the right side corresponds to the accelerating force that acts upon an electron in an electric field. The second term is a friction force that counteracts the acceleration and leads to a steady state motion of the electrons. Thereby, τ is the mean flight time between two scattering events. Despite its simplistic nature, the Drude model is able to qualitatively explain Ohm's law. This can be seen by considering the case $\partial \mathbf{v} / \partial t = 0$. By expressing the electric current in terms of the electronic number density n_e and mean velocity \mathbf{v} , one

obtains $\mathbf{j} = n_e q_e \mathbf{v}$ and consequently

$$\mathbf{j} = \sigma \mathbf{E}, \quad \sigma = \frac{q_e^2 n_e \tau}{m_e}, \quad (2.2)$$

i.e., a linear relation between current density and applied electric field. If a perfect conductor is considered, this relation no longer holds since the electrical conductance σ becomes infinite as $\tau \rightarrow \infty$. However, in this limit equation (2.1) reduces to

$$\frac{\partial \mathbf{j}_s}{\partial t} = \frac{1}{\Lambda} \mathbf{E}, \quad \Lambda = \frac{m_s}{n_s q_s^2} \quad (2.3)$$

allowing a persistent supercurrent flow over arbitrary times if $\mathbf{E} = 0$. The coefficient Λ is known as the London coefficient and contains the number density n_s , charge q_s , and mass m_s of the superconducting electrons. Originally it was believed that these quantities were the same as those for the normal conduction electrons. But since the advent of the BCS theory, it is known that $m_s = 2m_e$, $q_s = 2q_e$ and $n_s = 0.5n_e$, i.e., the superconducting electrons are bound pairs of electrons. Since the property (2.3) only holds for temperatures $T < T_c$, it implies that the number density n_s has to become zero at $T = T_c$ and finite for $T < T_c$.

Taking the curl of (2.3) yields the second London equation

$$\Delta \mathbf{B} = \frac{\mu_0}{\Lambda} \mathbf{B}, \quad (2.4)$$

where Maxwells equations

$$\nabla \cdot \mathbf{E} = 0 \quad (2.5)$$

$$\nabla \cdot \mathbf{B} = 0 \quad (2.6)$$

$$\nabla \times \mathbf{E} = - \frac{\partial \mathbf{B}}{\partial t} \quad (2.7)$$

$$\nabla \times \mathbf{B} = \mu_0 \mathbf{j} + \frac{1}{c^2} \frac{\partial \mathbf{E}}{\partial t} \quad (2.8)$$

as well as the vector identity $\nabla \times \nabla \times \mathbf{B} = -\Delta \mathbf{B} + \nabla(\nabla \cdot \mathbf{B})$ were used. In the derivation, the effect of displacement currents is not considered, and charge neutrality is assumed. Equation (2.4) has the form of a screening equation and describes the exponential decay of magnetic fields in the superconducting material, i.e., the Meißner effect. In the original paper of F. London and H. London, it was shown that the other quantities \mathbf{j} and \mathbf{E} are screened from the interior of the SC in the same way as \mathbf{B} [3]. The characteristic length over which the fields decay is called the London penetration depth

$$\lambda_L = \sqrt{\frac{\Lambda}{\mu_0}}. \quad (2.9)$$

Experimentally, one finds $\lambda_L(\bar{t}) = \lambda_L(0)(1 - \bar{t}^4)^{-1/2}$ where $\bar{t} = T/T_c$ is the reduced temperature and $\lambda_L(0)$ the value of λ_L for $\bar{t} = 0$ (Gorter-Casimir-model) [30]. This model adequately describes the disappearing of n_s and the diverging penetration depth at $T = T_c$. Equations (2.3) and (2.4) contain the main aspects of macroscopic SCs. It

is also possible to combine them into a single equation by expressing \mathbf{E} and \mathbf{B} in terms of their electromagnetic potentials. In this way, and by setting the scalar potential ϕ to zero, one obtains

$$\mathbf{j}_s = -\frac{1}{\Lambda} \mathbf{A}. \quad (2.10)$$

A linear relation between supercurrent density and magnetic vector potential is also predicted by the BCS theory, and it appears in other phenomenological theories as well. However, (2.10) is not gauge invariant and only compatible with (2.3) if $\nabla \cdot \mathbf{A}$ is valid. This condition, called London-gauge, is necessary to ensure $\nabla \cdot \mathbf{j}_s = 0$.

A more general form of the London equations can be derived from quantum mechanical principles, as was done by F. London in 1950 [31]. The idea is that the ensemble of superconducting electrons forms a quantum-mechanically correlated state that can be described by a macroscopic wave function $\Psi(\mathbf{r}, t) = \Psi_0(\mathbf{r}, t)e^{i\theta(\mathbf{r}, t)}$. Here $n_s = \Psi_0^2$ is the density of superconducting charge carriers. When this wave function is inserted into the Schrödinger equation, one obtains the standard quantum mechanical expression for the current density

$$\mathbf{j}_s = \frac{q_s}{m_s} n_s (\hbar \nabla \theta - q_s \mathbf{A}). \quad (2.11)$$

It can be easily seen that for a space-independent phase, the expression (2.11) becomes identical to (2.10). But in contrast to the old expression, the new form of the supercurrent density is gauge invariant. By taking the curl of (2.11), one gets the second London equation (2.4) again. A slightly modified form of the first London equation can also be obtained from the quantum mechanical treatment of the SC. But the derivation is not laid out here since it does not add to the discussion.

Although the London theory has the advantage of being valid for all temperatures $T < T_c$, it is based on the assumption of a homogeneous condensate n_s . In many situations, this assumption is not justified, e.g., at SC/normal metal interfaces or in type-II SCs where the presence of vortices leads to strong spatial variations of $n_s(\mathbf{r})$. In such situations, it is necessary to use a more general approach, like the GL theory.

2.2 Ginzburg-Landau theory

The second famous mean field theory of superconductivity was developed in 1950 by V. L. Ginzburg and L. D. Landau [4]. Like the London theory, the GL-model relies on the existence of a macroscopic wave function $\Psi(\mathbf{r}) = \Psi_0(\mathbf{r})e^{i\theta(\mathbf{r})}$ which describes the entire pair-correlated electronic system of the SC. In fact, the GL theory can be seen as a generalized London theory for situations where the superconducting condensate is non-homogeneous, e.g., due to strong external magnetic fields or material defects. However, given its highly phenomenological nature, and rather intuitive derivation, the classic GL theory was initially treated with skepticism. Only in 1959 was it shown by Gor'kov that the GL-equations can be derived from the microscopic BSC theory under the condition that $T \lesssim T_c$ [32]. With its new microscopic interpretation, GL theory became one of the most important tools for the theoretical investigation of superconductivity. Over the last decades, it was not only extended in various ways [33–39], it also found

applications in other areas of condensed matter physics. For example, it is an effective tool to describe the dynamics of nonlinear waves, superfluids, liquid crystals, and strings in field-theory [40].

In the framework of Landau's theory of second-order phase transitions, the occurrence of superconductivity in a metal at $T < T_c$ can be characterized as a phase transition of second order. Thereby it is assumed that the macroscopic wave function undergoes a continuous change at the critical temperature with $\Psi = 0$ for $T > T_c$ and $\Psi \neq 0$ for $T < T_c$. In this way, the wave function can be utilized as an order parameter of the system where $n_s = |\Psi|^2$ corresponds to the density of superconducting charge carriers. The phase θ by itself is no observable, and the physical state of the system is unaffected by arbitrary changes of the form $\Psi \rightarrow \Psi e^{i\chi}$ with $\chi(\mathbf{r}, t)$ being a continuously differentiable scalar field. Although not uniquely defined, the mere existence of a global phase can be seen as a type of order that is not present if the system is in the normal state. In Landau's theory of phase transitions, the appearance of a new, ordered phase is connected with a change of certain symmetries in the system. In the case of superconductivity, it is the gauge symmetry that is broken, as explained further down below.

Starting point for the development of the GL theory is the idea that close to the critical temperature T_c , the order parameter becomes small, and it is allowed to express the free energy density of the system in a series expansion of the form [4]

$$f = f_n + \alpha(T)|\Psi|^2 + \frac{\beta(T)}{2}|\Psi|^4. \quad (2.12)$$

In order for the system to develop a stable equilibrium, the functional derivatives $\delta f / \delta \Psi = 0$ and $\delta^2 f / \delta^2 \Psi > 0$ have to hold true. At temperatures above T_c , the free energy of the system has its normal-state value $f = f_n$. If the system is cooled below its critical temperature, the ordered phase with $\Psi \neq 0$ is energetically favorable and $f < f_n$. By evaluating (2.12) under these conditions, one finds $\alpha < 0$ for $T < T_c$ and $\alpha \geq 0$ for $T \geq T_c$. That allows approximating the true temperature dependence close to the critical temperature as $\alpha(T) \approx \alpha_0(T - T_c)$ with $\alpha_0 > 0$. The second condition for thermodynamic stability is that $\beta > 0$ for all temperatures. The equilibrium state which minimizes (2.12) is then

$$\Psi = \sqrt{\frac{-\alpha}{\beta}} e^{i\theta} = \Psi_\infty e^{i\theta}. \quad (2.13)$$

Here Ψ_∞ is the theoretical order parameter value inside an infinitely large SC. Apparently, the solution is only determined up to a global phase factor θ , and all solutions on the circle (2.13) in the complex plane are physically equivalent. This situation resembles the breaking of rotational symmetry when a FM is cooled down below its Curie temperature. In the paramagnetic phase, the magnetization displays rotational symmetry since the magnetic moments of the material are randomly distributed and cancel each other. However, below the Curie temperature, the magnetic moments reorient along a direction that is chosen randomly. Rotations of the system around that direction do not change the state of the system and do not cost energy. These excitations are also known as Goldstone modes. The Goldstone modes of the SC are associated with rotations of the global phase. This analogy is often referred to as the breaking of gauge symmetry at the phase transition into the superconducting state, even though the gauge invariance

of the theory is always intact [41]. If (2.13) is inserted into the expression of the free energy (2.12), one obtains

$$f - f_n = -\frac{B_{\text{cth}}^2(T)}{2\mu_0} = -\frac{\alpha^2}{2\beta} = -\frac{\alpha_0^2}{2\beta} T_c^2 \left(1 - \frac{T}{T_c}\right)^2 < 0, \quad (2.14)$$

i.e., the energy difference between the superconducting and the normal conducting phase. The generation of supercurrents in response to an external magnetic field is associated with a gain in kinetic energy. Therefore (2.14) can be expressed in terms of the thermodynamic critical field B_{cth} that destroys superconductivity. The prediction of the correct temperature dependence of the critical field was one of the first successes of the theory.

In cases where the order parameter can no longer be assumed uniform, it is necessary to add more terms to the free energy expression (2.12). In order to take gradients of Ψ and magnetic fields into account, Landau proposed the following form of the total free energy [4]

$$f - f_n = \alpha(T)|\Psi|^2 + \frac{\beta}{2}|\Psi|^4 + \frac{1}{2m_s} \left| \frac{\hbar}{i} \nabla \Psi - q_s \mathbf{A} \right|^2 + \frac{\mathbf{B}^2}{2\mu_0}. \quad (2.15)$$

Again, the first two terms correspond to the condensation energy of the superconducting electrons. The next term can be written as $|\hat{\mathbf{D}}\Psi|^2/2m_s = \mathbf{p}^2/2m_s$ and corresponds to the kinetic energy of flowing supercurrents. The last term is the field energy density associated with the magnetic flux density $\mathbf{B} = \nabla \times \mathbf{A} = \mathbf{B}_e + \mathbf{B}_s$. Thereby $\mathbf{B}_e = \nabla \times \mathbf{A}_e$ corresponds to an external magnetic field, and $\mathbf{B}_s = \nabla \times \mathbf{A}_s$ is the superconducting stray field, i.e., in the Meißner phase $\mathbf{B}_s = -\mathbf{B}_e$. One can again express $\Psi = \Psi_0 e^{i\theta}$ in terms of its amplitude and phase to get an equivalent form of (2.15)

$$f - f_n = \alpha(T)\Psi_0^2 + \frac{\beta}{2}\Psi_0^4 + \frac{\hbar^2 |\nabla \Psi_0|^2}{2m_s} + \frac{\Psi_0^2}{2m_s} (\hbar \nabla \theta - q_s \mathbf{A})^2 + \frac{\mathbf{B}^2}{2\mu_0}. \quad (2.16)$$

Apparently, deformations of the order parameter increase the total energy of the system, and it is, therefore, unfavorable to allow spatial variations of Ψ_0 or θ on an arbitrarily small length scale. Instead, the order parameter possesses a certain stiffness, and Ψ can only vary over a characteristic length scale ξ_{GL} , which is introduced below. The gauge invariant phase gradient has the form of a supervelocity $m_s \mathbf{v}_s = (\hbar \nabla \theta - q_s \mathbf{A})$ and is connected to flowing supercurrents. A functional derivative of $f[\Psi, \mathbf{A}]$ with respect to Ψ^* and \mathbf{A} yields the well known GL-equations

$$0 = \Psi (\beta |\Psi|^2 - |\alpha(T)|) + \frac{1}{2m_s} \left(\frac{\hbar}{i} \nabla - q_s \mathbf{A} \right)^2 \Psi \quad (2.17)$$

$$\frac{1}{\mu_0} \nabla \times \nabla \times \mathbf{A} = \mathbf{j}_s = i \frac{q_s \hbar}{2m_s} (\Psi \nabla \Psi^* - \Psi^* \nabla \Psi) - \frac{q_s^2}{m_s} |\Psi|^2 \mathbf{A} \quad (2.18)$$

The first GL-equation (2.17) resembles the Schrödinger equation of a charged particle in a magnetic field. However, the equation is nonlinear in Ψ , and the cubic term acts as a repulsive potential of Ψ onto itself. Therefore the wave function tends to avoid

the accumulation of superconducting charge. This tendency is counterbalanced by the negative pair binding potential $-|\alpha(T)|$. The interplay between these terms and the magnetic vector potential \mathbf{A} shapes the energy landscape of the SC, as described by (2.15). The nonlinear Schrödinger equation also appears in many other areas of physics like fluid dynamics, optics, and Bose-Einstein condensation (see [42] and references therein). However, nontrivial analytical solutions can only be found by simplifying the model, e.g., by neglecting the nonlinear term in the limit $T \lesssim T_c$ where $|\Psi|^2 \ll 1$ [5]. The expression on the right hand side of (2.17) should be understood as an operator expression $\hat{\mathbf{D}}^2 \Psi$ which evaluates to

$$(a\nabla + b\mathbf{A})^2 \Psi = a^2 \Delta \Psi + 2ab \nabla \Psi \cdot \mathbf{A} + ab \Psi \nabla \cdot \mathbf{A} + b^2 \mathbf{A}^2 \Psi. \quad (2.19)$$

In the derivation of (2.17) the boundary condition

$$\left(\hat{\mathbf{D}} \Psi \right) \cdot \mathbf{n} = 0, \quad \text{on} \quad \partial \Omega_{\text{SC}} \quad (2.20)$$

was applied where \mathbf{n} is the outer surface normal of the superconducting domain boundary Ω_{SC} . This boundary condition is valid for SC/insulator interfaces. A generalization of (2.20) can be obtained by setting $\hat{\mathbf{D}} \Psi \cdot \mathbf{n} = i\hbar \Psi / b$ [43]. This form considers the superconducting proximity effect at SC/normal metal interfaces. The parameter b is called the extrapolation length and states how far superconductivity can penetrate into the adjacent metal. For normal metals one has $b > 0$ whereas for insulators $b \rightarrow \infty$ leading to (2.20). For FMs, the extrapolation length goes to zero, which enforces $\Psi = 0$ and $\hat{\mathbf{D}} \Psi \cdot \mathbf{n} = 0$. The boundary condition $\Psi = 0$ on its own is not a valid choice since it can lead to unphysical solutions for certain geometries of the SC [3]. It should be noted that all the above-mentioned boundary conditions lead to $\mathbf{j}_s \cdot \mathbf{n}$, which means supercurrents can not cross the surface of the SC.

The second GL-equation is Ampère's law for a stationary supercurrent. The derivation of this equation from the free energy density (2.15) requires setting a boundary condition for $\mathbf{B} = \nabla \times \mathbf{A}$. For homogeneous external magnetic fields, two choices are valid. For example, if a finite-sized SC in free space is considered, it is possible to use open boundary conditions. Thereby $\mathbf{B} = \mathbf{B}_e$ is set at large distances from the SC. In this way, the interaction of the SC with its own stray field is adequately taken into account, and demagnetization effects due to sample geometry are also considered. From a numerical standpoint, operating with open boundary conditions is highly demanding and often only applicable to stationary systems. A more common choice is to set $\mathbf{B} \times \mathbf{n} = \mathbf{B}_e \times \mathbf{n}$ at the surface of the SC, which is essentially the same as

$$\mathbf{B}_s \times \mathbf{n} = 0, \quad \text{on} \quad \partial \Omega_{\text{SC}}. \quad (2.21)$$

This boundary condition is applicable if demagnetizing effects can be neglected, e.g., for very long superconducting prisms.

For non-homogeneous external fields, e.g., generated by a current-driven coil, the right side of equation (2.18) needs to be supplemented with an additional term $\mathbf{j}_e = \nabla \times \mathbf{B}_e / \mu_0$. Also in this case, open boundary conditions are valid with $\mathbf{B} = 0$ at large distances.

The expression of \mathbf{j}_s in (2.18) is identical to the supercurrent density derived from the London theory. Also, in the limit of a homogeneous order parameter distribution,

(2.18) and (2.4) have an identical form, which can be easily verified by applying the curl-operator to (2.18). Therefore, for constant n_s , the two models lead to the same results. Given this similarity, one can easily find an expression for the magnetic penetration depth in the GL theory. By replacing the particle density n_s in (2.9) with $|\Psi_\infty(T)|^2 = \alpha(T)/\beta$ one obtains

$$\lambda_{\text{GL}}(T) = \sqrt{\frac{m_s \beta}{q_s^2 \mu_0 |\alpha(T)|}} = \frac{\lambda_L(0)}{2} \frac{1}{\sqrt{1 - \bar{t}}} \quad (2.22)$$

This result is formally identical to (2.9) for $T \lesssim T_c$. The second equality was derived by utilizing $1 - \bar{t}^4 \approx 4(1 - \bar{t})$ for $\bar{t} \lesssim 1$. The GL-penetration depth is a material parameter that is usually taken from experiments. It is known that λ_{GL} depends not only on the material and sample composition [44] but also on the geometry of the SC [45], i.e., in thin films, the effective penetration depth has the form $\lambda_{\text{eff}} = 2\lambda_{\text{GL}}^2/d$ with film thickness d .

The second important length scale in the GL-formalism is the GL-coherence length ξ_{GL} , which indicates the spatial scale over which the order parameter can effectively change. Naturally, it is connected with the stiffness term in (2.16) and appears when the equation is normalized by dividing by $|\alpha|$. In the absence of magnetic fields, the normalized energy density takes on the form

$$\frac{f}{|\alpha|} = \frac{f_n}{|\alpha|} + \Psi_0^2 \left(-1 + \frac{1}{2} \frac{\Psi_0^2}{|\Psi_\infty|^2} \right) + \xi_{\text{GL}}(T)^2 |\nabla \Psi_0|^2, \quad (2.23)$$

with

$$\xi_{\text{GL}}(T) = \sqrt{\frac{\hbar^2}{2m_s |\alpha(T)|}} = \xi_{\text{GL}}(0) \frac{1}{\sqrt{1 - \bar{t}}}. \quad (2.24)$$

Like the GL penetration depth, the coherence length diverges at the critical temperature. With the above definitions, it is now possible to express the thermodynamic critical field in terms of the characteristic length scales.

$$B_{\text{cth}} = \frac{\hbar}{\sqrt{2} q_s \lambda_{\text{GL}} \xi_{\text{GL}}}. \quad (2.25)$$

Since λ_{GL} and ξ_{GL} show the same temperature dependence near T_c their ratio

$$\kappa = \frac{\lambda_{\text{GL}}}{\xi_{\text{GL}}} = \sqrt{\frac{m_s^2 \beta}{\mu_0 \hbar^2 q_s^2}} \quad (2.26)$$

is a temperature-independent material parameter called GL parameter. The important meaning of κ for the response of a SC to external magnetic fields will become evident in the context of type-II SCs.

2.3 Type-II superconductors

In 1950, Ginzburg and Landau predicted that the surface energy of an interface between superconducting and normal conducting material could become negative for sufficiently

high values of κ [4]. For such a SC it is, therefore, energetically advantageous to allow the formation of normal conducting domains inside the material. Due to this tendency of proliferating normal metal/SC interfaces, this new class of materials was expected to display a certain instability of the normal phase. Some years later, a correct interpretation of this phenomenon was given by A.A. Abrikosov in his famous work about so-called type-II SCs [5]. Up to this point, it was only known that SCs show the conventional Meißner effect and expel magnetic fields from their interior for $B < B_{\text{cth}}$.

For sufficiently small magnetic fields, type-II SCs behave exactly the same as type-I SCs. The predicted phase instability comes into play when the external magnetic field is increased above the value B_{c1} . At this so-called lower critical field, the magnetic response of the SC changes, and magnetic fields are no longer screened perfectly. More precisely, it was shown by Abrikosov that for materials with $\kappa \geq 1/\sqrt{2}$, the magnetic flux can enter the SC in quantized amounts $\Phi_0 = 2\pi\hbar/q_s$ once the magnetic field exceeds the value B_{c1} . In this new state, the magnetic field is threading the material along channels of weakened superconductivity, called vortices or fluxons. Each vortex corresponds to a normal conducting tube surrounded by a whirl of supercurrents, and each vortex carries exactly one quantum of magnetic flux. The tendency to form these normal conducting regions is a natural consequence of the negative interface energy of type-II materials. It is counterbalanced by the positive energy related to gradients in the order parameter amplitude n_s and phase θ . The exact condition under which a vortex can form is, therefore, dependent on the topography of the energy landscape of the SC. Material composition and geometry of the sample also play an important role in the problem of vortex formation.

The field interval $B_{c1} < B_e < B_{c2}$ over which vortex states appear is also known as the Shubnikov phase, and B_{c2} is called the upper critical field. In the framework of conventional GL theory, the values of B_{c1} and B_{c2} can be estimated analytically [28], although in general, they need to be calculated numerically by solving the GL-equations. For high magnetic fields $B_e > B_{c2}$, the SC becomes normal conducting again. To some extent, this is because of the pair-breaking effect of the flowing supercurrents. But also, the high number of increasingly overlapping vortex cores reduces the order parameter. The gradual reduction of superconductivity at B_{c2} comes along with a second-order phase transition into the resistive state. This is in contrast to the sharp first-order phase transition of type-I materials at B_{cth} .

In general, the number of vortices in the sample increases with the strength of the applied magnetic field. It is, therefore, natural to ask how these objects interact with each other and how they arrange when the SC is in equilibrium. This question was first addressed by A.A. Abrikosov in 1957, and he predicted a simple cubic vortex lattice to be the state of lowest energy [5]. However, a more detailed analysis of this problem reveals that vortices have a greater tendency to arrange in a hexagonal lattice, called the Abrikosov lattice. Qualitatively this behavior can be understood from classical electrodynamics. From an electromagnetic point of view, vortices behave similarly to little bar magnets. The current loops around each fluxon generate a magnetic moment that is aligned with the direction of the external magnetic field. Bringing magnetic moments of such orientation in close vicinity to each other is energetically unfavorable. Therefore, under normal conditions, vortices have a strong tendency to repel each other. The state which minimizes the interaction energy between neighbored fluxons corresponds to a

hexagonal lattice. For such a crystal, the field-dependent lattice constant can be calculated as $c_h = 1.075\sqrt{\Phi_0/B_e}$, whereas for a cubic lattice, one finds $c_c = \sqrt{\Phi_0/B_e}$ [28]. That means, in a cubic lattice, the distance between vortices is slightly smaller and the interaction energy larger.

In a real SC, the vortex lattice often deviates from a perfectly hexagonal structure. The reason for this discrepancy between theory and experiment is the existence of inhomogeneities in the material. For example, variations in the electronic mean free path l also affect the critical temperature T_c as well as λ_{GL} and ξ_{GL} [44]. That, in return, makes some places in the material energetically more favorable for vortex accumulation than others. In particular, vortices occupy places with reduced order parameter density since such a combination of vortex and defect allows the SC to save the condensation energy required for the generation of the vortex core [29]. Also, locations of reduced sample thickness attract vortices since, in this way, the supercurrent threading the material, and the associated kinetic energy, can be reduced. A consequence of such material imperfections is the distortion of the vortex lattice. Material defects that can bind vortices are also called pinning centers. Depending on the strength and overall distribution of material defects, the vortex lattice can be kept static in the presence of a transport current. In the absence of pinning centers, a current density \mathbf{j}_e injected into the SC will impose a Lorentz force density

$$\mathbf{F}_L = \mathbf{j}_e \times \mathbf{B} \quad (2.27)$$

onto each vortex (see e.g [29]). This force deflects the vortices, giving them velocities of up to several km/s [46, 47]. A moving vortex thereby generates an electric field counteracting the imposed bias voltage. As a consequence, the flux flow state of the SC is characterized by a finite electrical resistance and unwanted energy dissipation. In extreme cases, the generated heat can even transit the SC back into the normal conducting state. The vortex motion itself is viscous, meaning that once the electric current is switched off, the SC quickly returns to equilibrium. In superconducting devices, the motion of vortices is often highly undesirable, and much research was performed to understand how the pinning properties of SCs can be optimized. [48–52]. In high-temperature SCs the problem of flux motion becomes even more involved since thermal fluctuations deteriorate the pinning properties of the material even further. In addition, the combination of material properties and defects can lead to the appearance of various vortex phases, including vortex crystals, liquids, and glassy phases [53]. The problem of vortex pinning will be addressed again in Chapter 5.

2.3.1 Structure of a vortex

Before it is discussed how the stray field of a superconducting vortex can be calculated, it is worth taking a closer look at the spatial structure of such an entity. In Fig. 2.1, a vortex-solution of the classic GL-equations in a bulk SC with $\xi_{GL} = 150$ nm and $\lambda_{GL} = 450$ nm is shown. In this particular case, only one fluxon is present in the system, and the external magnetic field is set to zero. As one can see, a regular Abrikosov-vortex has cylindrical symmetry, and the order parameter is suppressed at its center. However, the defining property of a vortex is its distinct phase profile which demands that $\oint_C \nabla\theta \cdot d\mathbf{l} = 2\pi$ (cf. Fig. 2.1(b)). Here C is an arbitrary closed path around

the phase singularity at the vortex core. The condition of a constant winding number gives the vortex state a high degree of stability, which means smooth deformations of the phase field can not destroy it. In terms of classical field theory, one can say that the vortex experiences topological protection, and the winding number of the phase field is a topological invariant. However, for the following discussion, the topological aspects of superconductivity are not of importance. For further information on this topic, see, e.g., [54] and references therein. Close to the vortex center, the phase gradient can be approximated by $\nabla\theta = \mathbf{e}_\varphi/r$, which means that the corresponding superfluid velocity takes on very large values. Still, the supercurrent density is finite since $\mathbf{j}_s \sim n_s \mathbf{v}_s$ with $n_s = 0$ at the vortex core. The spatial distribution of \mathbf{j}_s is shown in Fig. 2.1 (c). The circular supercurrents around the vortex core give rise to a magnetic field with flux $\int_F \mathbf{B} \cdot d\mathbf{F} = \Phi_0$ where F is a slice through the vortex in a quasi-infinite sized SC. In small-sized SCs, this property has the more general form of

$$\frac{m_s}{q_s} \oint_{\partial F} \mathbf{v}_s \cdot d\mathbf{l} + \int_F \mathbf{B} \cdot d\mathbf{F} = n\Phi_0, \quad n = 0, 1, 2, \dots \quad (2.28)$$

where the quantity on the left side is called fluxoid. The existence of this quantization condition is another aspect of the macroscopic quantum nature of SCs. Its experimental confirmation by Doll and Näbauer [9] and Deaver and Fairbank [10] in 1961 also verified that $q_s = 2q_e$, as predicted by the BCS-theory.

In Fig. 2.1 (e), the radial profile of a vortex is shown. It should be noted that here $\Psi_0 = |\Psi|$ is plotted whereas in (a), $n_s = |\Psi|^2$ is shown. In principle, one can operate with either of these quantities, but it is conventional to use n_s for numerical investigations of SCs. In contrast to the Cooper pair density, the actual amplitude of the wave function is not differentiable at the core of the vortex. Furthermore, Ψ_0 rapidly rises to unity over the length scale ξ_{GL} giving the vortex a diameter of approximately $2\xi_{\text{GL}}$. Depending on material composition and temperature, the normal conducting core can extend to a few nm (like in YBCO and other high- T_c materials [28, 55]) up to several hundred nanometers (e.g., in clean Nb at $T \lesssim T_c$ [28]). The supercurrent density and magnetic flux density have a similar behavior outside the vortex where they diminish over the characteristic length scale λ_{GL} . Inside the vortex, \mathbf{j}_s goes to zero, whereas \mathbf{B}_s reaches its maximum. The displayed behavior is typical for vortices in a perfectly clean bulk material. At surfaces, the magnetic flux density adopts a more complicated form, and the magnetic field spreads like a flower giving rise to nonzero x- and y-components (cf. Fig. 2.2). Material defects can also change the flow of \mathbf{j}_s leading to vortex bending and the formation of complicated filamentary structures in extended SCs [56–58].

In many situations, the external magnetic field is homogeneous, and all vortices have equally oriented magnetic moments. If the external field is inhomogeneous, e.g., in the vicinity of a FM, the vortices try to align locally with the external field. In this way, vortices of opposite polarity can appear in the same sample, and one speaks of vortices and antivortices [59–65]. Due to their opposite polarity, these vortex-antivortex (VAV) pairs attract each other, and they have a high tendency to annihilate. In certain cases, the external magnetic field also allows the formation of closed vortex loops and semi-loops [66–68]. The research in superconducting vortex dynamics is an active field, and many exotic vortex states have been found, e.g., giant vortices [69], multi-quanta-vortices [70], fractional quantum vortices [71], VAV-pairs in type-I SCs [72], Josephson- and

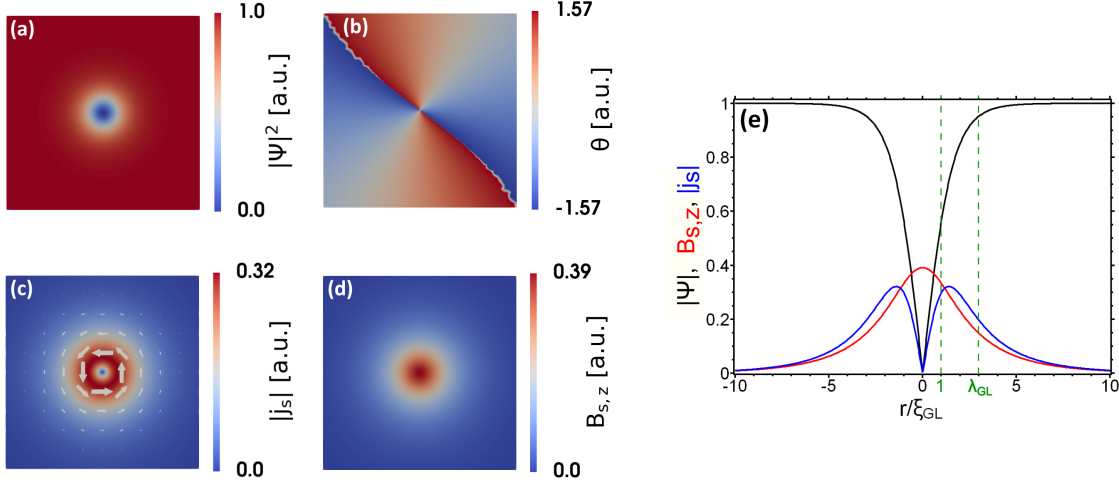


Figure 2.1: Vortex profile of a SC with $\lambda_{GL} = 450$ nm, $\xi_{GL} = 150$ nm and $\kappa = 3$ in zero external magnetic field. (a)-(d): local Cooper pair density $n_s = |\Psi|^2$, phase field θ , supercurrent density \mathbf{j}_s and magnetic flux density $B_{s,z}$ of the vortex. The white arrows in (c) mark the local direction and magnitude of the supercurrent density (e): Radial profile of $|\Psi|$, $B_{s,z}$ and $|\mathbf{j}_s|$ around the vortex core.

Josephson-like vortices [73, 74] and pancake vortices [75] in high-Tc materials. Finally, it should be noted that VAV-pairs can also be generated with the aid of a transport current flowing through the SC [76]. The combination of different external magnetic fields, transport currents, temperature fields, and SC geometries allows for a plethora of new and unexplored vortex states, making the field of vortex research interesting for theory and application.

2.3.2 Field of a vortex

Apart from their important impact on the electrodynamic behavior of the SC, vortices are also interesting for applications. An ensemble of static fluxons can be used to construct logic gates with potential usage in information technology [77–79]. But also in FM/SC hybrids, vortices were proposed to be useful in order to generate and amplify spin waves [80, 81], bind skyrmions [82–84] and shape the magnonic dispersion [85]. In all these cases, the magnetic field generated by the vortices is of crucial importance. However, the calculation of this field is a difficult task since, in general, it requires the self-consistent solution of the GL-equations. Analytical solutions to this problem can only be found if simplifications are made. For example, it is often suitable to operate in the high kappa limit, where the vortex diameter can be neglected, and n_s is approximately constant. In this way, it is possible to find analytical approximations for the vortex field \mathbf{B}_v of a single straight vortex line in a thin film of arbitrary thickness [86]. In the work presented here, such a simplification is unsuitable since Nb is the superconducting material of choice. Depending on its degree of purity Nb has $\kappa_\infty = 0.8$ (clean limit) and $\kappa \gg 1$ (dirty limit) [28]. Though, the latter limit will not be relevant to this work. The here-considered Nb samples are of average purity with $1 < \kappa < 5$. In this regime, the size of

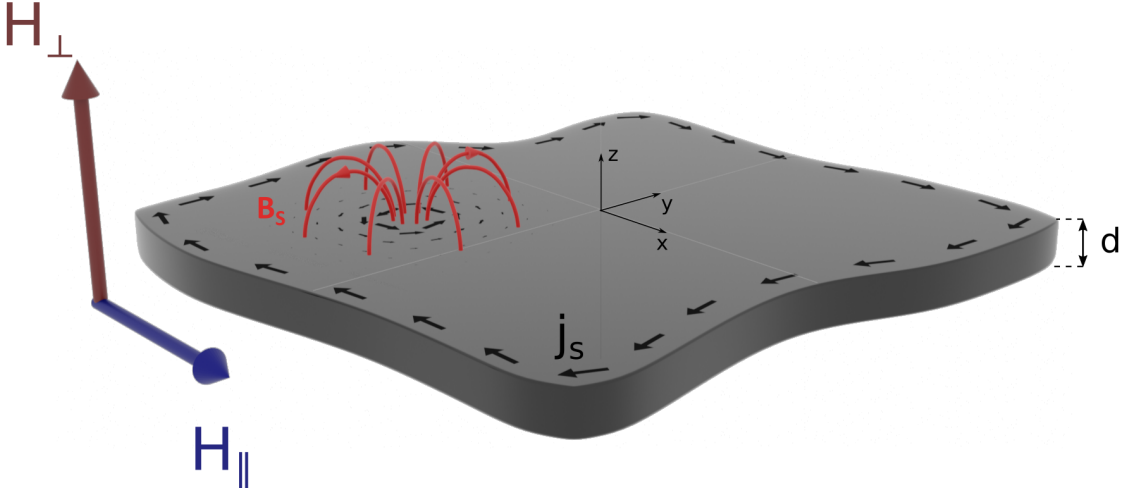


Figure 2.2: Schematic of a superconducting thin film of arbitrary shape. The red curves correspond to the field lines of \mathbf{B}_s in the vicinity of a superconducting vortex.

the vortex core and its influence on the current distribution and stray fields can not be neglected. Still, the self-consistent solution of (2.17) and (2.18) can be avoided in certain cases, as discussed in the following paragraphs.

Thin film

In the following, it is assumed that the SC is a plain thin film of arbitrary shape (see Fig. 2.2). For such a geometry with $d \ll \xi_{GL}$, the order parameter becomes effectively independent of the direction of the film-normal (here the z -direction). For the external magnetic field, two cases have to be considered.

First, a field parallel to the plane does not allow vortex solutions since this would require $d \sim 2\xi_{GL}$. In the here-considered case, increasing the in-plane field only leads to a gradual order parameter suppression with a second order phase transition at $H_{c\parallel}$ [29]. The diamagnetic response of the SC to such an in-plane field is usually rather weak and, therefore, $H_{c\parallel}$ can exceed the bulk value H_{c2} for the upper critical field substantially.

If the external magnetic field is directed parallel to the plane-normal, vortex solutions of the GL-equations become possible. However, the quantum expression for the supercurrent density (2.11) does not explicitly depend on the film thickness, i.e., for $\mathbf{A} = \mathbf{A}(x, y)$ and $\Psi = \Psi(x, y)$ also the supercurrent density becomes independent of the z -direction. That means if the film thickness is reduced, the stray fields of the vortices become weaker as well. In addition, the effective magnetic penetration depth $\lambda_{\text{eff}} \sim 1/d$ is thickness dependent as well, reducing the screening capabilities of the SC even further [45]. Under these conditions, the magnitude of the stray field becomes negligible compared to the external magnetic field, and the solution of the first GL-equation is sufficient to simulate the system behavior [73].

If the SC stray field is still of interest, e.g., as input for another differential equation, it can be calculated from (2.18). A standard procedure for this problem is to choose open boundary conditions for \mathbf{A}_s and solve Ampère's law in free space. This method will be

explained in more detail in Chapter 4. If only the field distribution in a small fraction of space is of interest, it is more convenient to solve Biot Savarts Law

$$\mathbf{B}_v = \frac{\mu_0}{4\pi} \int \mathbf{j}_s(\mathbf{r}') \times \frac{\mathbf{r} - \mathbf{r}'}{|\mathbf{r} - \mathbf{r}'|^3} dV'. \quad (2.29)$$

For later numeric calculations, it is convenient to use the fact that $\mathbf{j}_s = \mathbf{j}_s(x, y)$ and integrate (2.29) along the film thickness. In this way, one obtains

$$\mathbf{B}_v = \frac{\mu_0}{4\pi} \int \left(\frac{1}{r_{z-}} - \frac{1}{r_{z+}} \right) \mathbf{j}_s(\mathbf{r}') \times \mathbf{e}_z - g(\mathbf{r}') [\mathbf{j}_s(\mathbf{r}') \cdot ((\mathbf{r}_0 - \mathbf{r}') \times \mathbf{e}_z)] \mathbf{e}_z dF'. \quad (2.30)$$

where the domain of integration is now the cross-section of the superconducting prism. The space-dependent function g is given as

$$g(\mathbf{r}') = \frac{1}{|\mathbf{r}_0 - \mathbf{r}'|^2} \left(\frac{z_-}{r_{z-}} - \frac{z_+}{r_{z+}} \right)$$

$$r_{z\pm} = (x - x')^2 + (y - y')^2 + z_{\pm}^2$$

$$z_{\pm} = z \pm d/2.$$

with $\mathbf{r}_0 = (x, y, 0)$ and $\mathbf{r}'_0 = (x', y', 0)$.

Artificial vortex lattice

In situations where the density of vortices in the sample is high, and the extent of the SC is finite, the existing analytic thin-film solutions of \mathbf{B}_v can no longer be applied. It is then necessary to approximate the vortex field by other means. One technique relies on the observation that the stray field of an isolated vortex resembles the field of a small bar magnet. The stray field of a ferromagnetic cuboid of side length $\Delta x = 2x_b$, $\Delta y = 2y_b$, $\Delta z = 2z_b$ and magnetization $\mathbf{M} = M_s \mathbf{e}_z$ can be calculated analytically [87] and has the form:

$$\mathbf{h}_{\text{FM}} = \frac{M_s}{4\pi} \sum_{k,l,m=1}^2 (-1)^{k+l+m} [\log(y_l + r_{klm}) \mathbf{e}_x + \log(x_k + r_{klm}) \mathbf{e}_y] + \quad (2.31)$$

$$- \frac{M_s}{4\pi} \sum_{k,l,m=1}^2 (-1)^{k+l+m} \text{sign}(x_k z_m) \arctan \left(\frac{|x_k| y_l}{|z_m| r_{klm}} \right) \mathbf{e}_z.$$

Here, the origin of the coordinate system is located at the center of the cuboid. Also, the following abbreviations are used

$$x_k = x + (-1)^k x_b$$

$$y_l = y + (-1)^l y_b$$

$$z_m = z + (-1)^m z_b$$

$$r_{klm} = \sqrt{r_k^2 + y_l^2 + z_m^2}.$$

By adjusting the dimensions and magnetization of such a ferromagnetic nano cube, it is possible to use (2.31) to approximate the field of an ensemble of superconducting vortices. This technique will be used in Chapter 6 to simulate the interaction between vortices and magnons. Although useful, the magnetic field described by (2.31) is not suitable as input for the GL-equations since here, the magnetic vector potential instead of the H-field is required. In situations where the interaction between vortices and ferromagnetic nanocubes is of interest, it is, therefore, suitable to calculate the vector potential corresponding to (2.31). This field can be calculated analytically as well and has the form

$$\begin{aligned} \mathbf{A}_{\text{FM}} = & -B_0 \sum_{k,l,m=1}^2 (-1)^{k+l+m} [x_k \log(-z_m + r_{klm}) + z_m \log(-x_k + r_{klm})] \mathbf{e}_x \\ & + B_0 \sum_{k,l,m=1}^2 (-1)^{k+l+m} [y_l \log(-z_m + r_{klm}) + z_m \log(-y_l + r_{klm})] \mathbf{e}_y \\ & + B_0 \sum_{k,l,m=1}^2 (-1)^{k+l+m} \left[|x_k| \arctan\left(\frac{y_l z_m}{|x_k| r_{klm}}\right) \mathbf{e}_y - |y_l| \arctan\left(\frac{x_k z_m}{|y_l| r_{klm}}\right) \mathbf{e}_x \right] \end{aligned} \quad (2.32)$$

with the same abbreviations as before and $B_0 = \mu_0 M_s / 4\pi$.

2.4 Time-dependent Ginzburg-Landau theory

Over the decades, the London theory and the conventional GL theory have proven to be powerful tools that can explain many features of conventional SCs, e.g., the appearance of Little-Parks oscillations in thin-walled cylinders [88, 89] and the Josephson effect [90]. Also, a considerable number of generalized GL-theories were developed to describe phenomena like the Fulde-Ferrel-Larkin-Ochinkov-phase (FFLO) in SC/FM hybrids [91], superconducting alloys at arbitrary temperatures [92] and unconventional p-wave superconductivity in SC/FM multilayer systems [93]. However, one fundamental flaw of the theory is its inability to describe non-equilibrium phenomena since the conventional GL approach does not consider a time dependence of Ψ and \mathbf{A} . Finding a time-dependent generalization of the GL equations has turned out to be rather difficult since, for conventional SCs, the density of states displays a singularity at the gap edge [29]. Therefore a good TDGL theory of general validity can only be obtained for materials that are gapless or the singularity in the density of states has been smoothed out by a sufficient concentration of paramagnetic impurities. Several TDGL approaches were developed, taking these considerations into account [94–96]. For the present discussion and the forthcoming calculations, the TDGL equations proposed by Schmid and derived by L.P. Gor'kov and G.M. Eliashberg will be used [94]

$$0 = \frac{\hbar}{2m_s D} \left(\hbar \frac{\partial \Psi}{\partial t} + i q_s \phi \Psi \right) + \Psi (\beta |\Psi|^2 - |\alpha(T)|) + \frac{1}{2m_s} \left(\frac{\hbar}{i} \nabla - q_s \mathbf{A} \right)^2 \Psi \quad (2.33)$$

$$\frac{1}{\mu_0} \nabla \times \nabla \times \mathbf{A} = -\sigma \left(\frac{\partial \mathbf{A}}{\partial t} + \nabla \phi \right) + \mathbf{j}_s. \quad (2.34)$$

The first thing to note is that the equations (2.33) and (2.34) are invariant under the gauge transformations [97]

$$\Psi(\mathbf{r}, t) \longrightarrow \Psi(\mathbf{r}, t)e^{i\frac{q_s}{\hbar}\chi(\mathbf{r}, t)}$$

$$\mathbf{A}(\mathbf{r}, t) \longrightarrow \mathbf{A}(\mathbf{r}, t) + \nabla\chi(\mathbf{r}, t)$$

$$\phi(\mathbf{r}, t) \longrightarrow \phi(\mathbf{r}, t) - \frac{\partial}{\partial t}\chi(\mathbf{r}, t).$$

Later on, this property will be useful for simplifying the equations. The two most commonly used gauges in the TDGL-formalism are $\phi = 0$ (zero electric potential gauge) and $\phi + \omega\nabla \cdot \mathbf{A} = 0$, with a suitably chosen constant ω . These gauges have the advantage of eliminating the scalar potential from the TDGL equations altogether. The Coulomb gauge $\nabla \cdot \mathbf{A} = 0$ is also a valid choice. But it is less frequently used since it requires solving an additional equation for ϕ

$$0 = \nabla \cdot \left[\sigma \left(\frac{\partial \mathbf{A}}{\partial t} + \nabla \phi \right) + \mathbf{j}_s \right], \quad (2.35)$$

which can be obtained by applying the divergence to (2.34). It was already mentioned that in equilibrium situations and near the critical temperature, the first GL-equation (2.17) becomes identical to a Schrödinger equation for a charged particle in a magnetic field. This similarity disappears when dynamic systems described by the first TDGL equation (2.33) are considered. From a technical point of view, the first TDGL equation is a nonlinear diffusion equation for the complex-valued order parameter Ψ . The dynamics it describes are purely dissipative, meaning particle conservation and wave-like solutions are no longer possible. This point becomes clearer when considering a situation without electromagnetic fields and a spatially homogeneous order parameter. In this case, the equilibrium solution of (2.33) corresponds to (2.13). By inserting $|\Psi| = |\Psi_\infty| + \delta$ with $|\delta| \ll 1$ into the first TDGL equation and neglecting terms second order in δ one gets

$$\delta = \delta_0 e^{-\frac{t}{\tau_{\text{GL}}}}, \quad \tau_{\text{GL}} = \frac{\hbar^2}{2m_s D}. \quad (2.36)$$

Deviations from equilibrium, therefore, decay exponentially on a characteristic time scale τ_{GL} . The diffusion coefficient in the above formalism is $D = v_f l / 3$ where v_f is the material-specific Fermi velocity, and l is the electronic mean free path [29]. The scalar potential $\phi = \phi_e - \mu/e$ ensures gauge invariance of (2.33) and takes the effect of electric fields and the chemical potential μ into account. However, the scalar potential is often a redundant quantity in the TDGL-formalism and can be removed by applying an appropriate gauge. More insights into the dynamics of the SC are possible by inserting $\Psi = \Psi_0 e^{i\theta}$ into (2.33) and splitting into real- and imaginary parts. This procedure leads to two coupled equations for Ψ_0 and θ

$$0 = \frac{\hbar^2}{2m_s D} \frac{\partial \Psi_0}{\partial t} + \Psi_0 (\beta \Psi_0^2 - |\alpha(T)|) - \frac{\hbar^2 \Delta}{2m_s} \Psi_0 + \frac{1}{2m_s} (\hbar \nabla \theta - q_s \mathbf{A})^2 \Psi_0 \quad (2.37)$$

$$\frac{\hbar}{2m_s D} \left(\hbar \frac{\partial \theta}{\partial t} + q_s \phi \right) \Psi_0^2 = \frac{\hbar}{2q_s} \nabla \cdot \mathbf{j}_s. \quad (2.38)$$

Equation (2.38) can be interpreted as a continuity equation for supercurrents. In the presence of electric fields, and in non-equilibrium situations, the divergence of \mathbf{j}_s is no longer zero. That is, for example, the case if a time-dependent magnetic field is applied to the SC. The external vector potential then drives the time evolution of the phase and the coupled order parameter amplitude. For small magnetic fields one has $\Psi_0 \approx \Psi_\infty$, which allows to simplify (2.38) to

$$\frac{\partial \theta}{\partial t} - D\Delta\theta = -\frac{q_s}{\hbar} (\phi + D\nabla \cdot \mathbf{A}) \quad (2.39)$$

i.e., an inhomogeneous diffusion equation for the phase field θ . It should be noted that it is possible to eliminate the source term in (2.39) by using the gauge $\phi + D\nabla \cdot \mathbf{A} = 0$ [97]. But even in this case, the phase can assume nonzero values since its time evolution is also driven by the boundary condition (2.20), which has the form

$$\Psi_0 (\hbar\nabla\theta - q_s\mathbf{A}) \cdot \mathbf{n} = 0, \quad \text{on} \quad \partial\Omega_{\text{SC}} \quad (2.40)$$

$$\nabla\Psi_0 \cdot \mathbf{n} = 0, \quad \text{on} \quad \partial\Omega_{\text{SC}}. \quad (2.41)$$

The second TDGL-equation is the generalization of Ampère's law (2.34) with an additional eddy current term. The electrical conductivity $\sigma(\mathbf{r})$ is a material constant that can be taken from experiments (e.g., [44, 98]). A commonly used formula for the electrical conductivity is [27]

$$\sigma = \frac{l}{3.72 * 10^{-16}} \left[\frac{\text{A}}{\text{Vm}^2} \right]. \quad (2.42)$$

In most situations, σ can be treated as a scalar. However, in free space, σ is a step function with $\sigma > 0$ in the material and $\sigma = 0$ outside, giving $\nabla\sigma \rightarrow \infty$ on the surface of the sample.

After over 70 years of intense research, GL theory has helped to generate an enormous amount of scientific literature. One of its main applications is the theoretical investigation of superconducting vortex states in various 2d and 3d systems [99–111]. In particular, current driven vortex dynamics and vortex pinning [74, 112–127] have been studied in view of their high relevance for device performance. Apart from applied research [77–79, 128–134] also questions of fundamental interest are posed, e.g., How vortices react to temperature gradients [134–145], nearby ferromagnets [22, 68, 146–163], time dependent magnetic fields [164, 165] and electromagnetic radiation [166–168].

2.5 Validity of the Ginzburg-Landau theory

The series expansion of the GL-free energy (2.12) is only valid near the critical temperature where $|\Psi|^2 \ll 1$. In cases of a non-homogeneous order parameter distribution, it is additionally required that Ψ and \mathbf{A} are functions that vary slowly with \mathbf{r} . More precisely, it was shown by Gor'kov that the characteristic length scale for spatial variations of either of these quantities is the BCS-coherence length ξ_0 [32]. For the order

parameter, therefore, it is required that $\xi_{\text{GL}}(T) \gg \xi_0$, a condition that is well satisfied for $T \approx T_c$ (cf. (2.24)). The same argument can be made for spatial variations of the vector potential demanding $\lambda_{\text{GL}}(T) \gg \xi_0$. In dirty SCs, the conditions for validity are less restrictive since the electrodynamics of the SC become local [29]. In the dirty limit, one has $l \ll \xi_0$, and the theory is valid already for $\xi_{\text{GL}}(T) \gg l$ and $\lambda_{\text{GL}}(T) \gg l$.

Although the GL-theory has been developed for $T \lesssim T_c$, it still can give qualitatively correct results for much lower temperatures [169]. From a practical point of view, it is often suitable to operate at temperatures $T > 0.4T_c$. However, at low temperatures, the physics of the vortex core are no longer correctly described by the GL-formalism [57]. A better match with experiments can be obtained by modifying the temperature dependence of the GL parameters such that $\alpha \sim (1 - \bar{t}^2)/(1 + \bar{t}^2)$ and $\beta \sim 1/(1 + \bar{t}^2)^2$ [29].

Mean field theories are only valid as long as thermal fluctuations are negligible. Technically this limits the applicability of the GL theory to temperatures $T < T_{c1} < T_c$. Very close to the critical temperature, the mean value of the order parameter can no longer be considered dominant over the thermal fluctuations. The actual width of the forbidden temperature region can be estimated from the Ginzburg criterion. In this formalism, T_{c1} depends on the material itself and the considered system's dimensionality. E.g. for weak-coupling SCs in three dimensions, the temperature region $[T_{c1}, T_c]$ is usually very small, and the GL-theory can be considered to be valid arbitrarily close to T_c [170]. Nonetheless, if the effect of thermal fluctuations is of relevance, it can be included in the TDGL-formalism by adding a corresponding term to the first TDGL equation [142].

2.6 Micromagnetism

In this section, the basic concepts of micromagnetism and magnonics are introduced. Here, only the continuum approach of micromagnetism is covered since this work mainly focuses on the interaction of mesoscopic SCs and FMs. The methods and tools introduced here will be used in Chapter 6, where the interaction between magnonic excitations and superconducting vortices is investigated.

Micromagnetism is a continuum theory that aims at characterizing the state of a FM via its spatially averaged mean magnetization $\mathbf{M}(\mathbf{r}, t, T)$. On a microscopic scale, local magnetic moments $\boldsymbol{\mu}$ are associated with the spin and orbital motion of the electrons. The spatial and temporal mean value of $\boldsymbol{\mu}$ taken over a sufficiently large number of moments defines the local value of the macroscopic magnetization \mathbf{M} , which is, in most cases, a smooth and continuously differentiable vector field. The magnetization amplitude $|\mathbf{M}(\mathbf{r}, t, T)| = M_s(\mathbf{r}, T)$ is a temperature-dependent quantity that may vary locally. However, for sufficiently low temperatures, this local variation becomes small, and $|\mathbf{M}(\mathbf{r}, t, T)| = M_s(T)$ everywhere in the material, with M_s being the temperature-dependent saturation magnetization. In the following, the temperature dependence of the magnetization is not discussed. In the continuum limit, the micromagnetic energy of a FM under external magnetic field \mathbf{H}_e can be written in the form of a Gibbs–Landau free energy functional [171]

$$G[\mathbf{M}(\mathbf{r}, t), \mathbf{H}_e(\mathbf{r}, t)] = \int \left(\frac{A}{M_s^2} |\nabla \mathbf{M}|^2 + f_{\text{an}}(\mathbf{M}) - \mu_0 \mathbf{M} \cdot \mathbf{H}_e - \frac{\mu_0}{2} \mathbf{M} \cdot \mathbf{H}_m \right) dV \quad (2.43)$$

In the following, each energy contribution will be addressed separately. Here it is to say that the micromagnetic energy given by (2.43) is by far not complete, and effects due to stress, magnetorestriction, and antisymmetric exchange [172] are not taken into account. Although, their inclusion is straightforward once the corresponding energy is inserted into the integral.

2.6.1 Exchange interaction

The first term in the free energy functional (2.43) has a form similar to the stiffness term in the superconducting free energy density (2.16). That means that also in ferromagnetic systems, the corresponding order parameter \mathbf{M} can not vary on arbitrarily small length scales. The microscopic origin of this phenomenon is a strong coupling between neighbored spins of the crystal lattice, called exchange interaction. Consequently, neighbored spins in the crystal lattice can not change independently from each other and tend to align along a certain direction. A quantum mechanical treatment of this problem was done by W. Heisenberg, and he showed that ferromagnetic exchange due to the Pauli exclusion principle can be formulated as a Hamiltonian of the Form

$$\hat{H}_{\text{H}} = -2 \sum_{i>j} J_{ij} \hat{S}_i \cdot \hat{S}_j. \quad (2.44)$$

In FMs, the exchange constant J_{ij} is positive, and a parallel spin alignment minimizes energy. In antiferromagnets $J_{ij} < 0$, and spins tend to align antiparallel to minimize energy.

In the low-temperature limit, the exchange interaction prevails over all other interactions, and the canting between neighbored spins will be small. This idea can be utilized to express $\hat{S}_i \cdot \hat{S}_j$ in terms of the canting angle between the spins and expand the Hamiltonian (2.44) in a Taylor series [173]. As a result, the exchange energy in the continuum limit is

$$G_{\text{exc}} = \int \frac{A}{M_s^2} |\nabla \mathbf{M}|^2 dV = \int \frac{A}{M_s^2} \sum_{i=1}^3 |\nabla (\mathbf{M} \cdot \mathbf{e}_i)|^2 dV, \quad (2.45)$$

where A is known as exchange stiffness, a material constant that depends on the properties of the crystal lattice and on the exchange constant J . The expression (2.45) is valid for the many common crystal types, like cubic and hexagonal lattices. However, its applicability is limited to low temperatures and smooth sample geometries where abrupt changes in the magnetization are energetically unfavorable.

2.6.2 Magnetic anisotropy

In many known ferromagnetic materials, it can be observed that the magnetization alignment favors certain directions in space. This phenomenon is known as magnetic anisotropy. It is often an intrinsic property of the material, e.g., it can result from the crystal symmetry, the shape of the material, or internal strain [174, 175]. Nonetheless, also external forces can enforce spin alignment in the form of pressure-induced anisotropy [176]. In all these cases, an incomplete alignment between the magnetization and its preferred axes is energetically costly. Therefore, the favored directions are also called the "easy axes," whereas the directions of the highest energy cost are called "hard axes." Often magnetic anisotropy is rather weak compared to ferromagnetic exchange. Nevertheless, its role in the process of domain formation and magnetic equilibrium states is still important and of technological relevance (for a detailed discussion, see, e.g., [173, 177, 178]). In many materials, a combination of spin-orbit coupling and an anisotropic crystal lattice makes the spins prefer a specific space direction. This so-called magneto-crystalline anisotropy can be viewed as an internal material-specific field that tends to align the electronic spins along certain crystallographic directions. This kind of anisotropy often has uniaxial character, and the corresponding energy density can be expressed as a Taylor series in the angle ϑ between the easy axis and the magnetic moment [173]

$$g_{\text{an}} = -K_1 \cos(\vartheta)^2 + K_2 \cos(\vartheta)^4 + \dots \quad (2.46)$$

In many cases, it is sufficient to truncate the series already after the first term since K_2 and higher order terms are negligible compared to K_1 . Also, since the directions corresponding to $\vartheta = \pi$ and $\vartheta = -\pi$ are energetically equivalent, odd powers of $\cos \vartheta$ do not appear in the series expansion (2.46). Expressed in terms of the easy axis direction \mathbf{e}_a the magnetic anisotropy energy can be written as

$$g_{\text{an}} = -K_1 (\mathbf{m} \cdot \mathbf{e}_a)^2. \quad (2.47)$$

In Chapter 6, the considered FM is made from Permalloy, for which even $K_1 \approx 0$. Therefore the role of magneto crystalline anisotropy for the presented results is of minor relevance.

2.6.3 Zeeman energy

The energy of a magnetic moment in an external magnetic field is known as Zeeman-energy and has the form

$$g_z = -\mu_0 \mathbf{M} \cdot \mathbf{H}_e. \quad (2.48)$$

The external field exerts a torque on \mathbf{M} leading to a precessional motion of the magnetic moment around the direction defined by \mathbf{H}_e . However, magnetic damping is always present in realistic systems, and an equilibrium state of the magnetization is achieved once the magnetic moment and external field align.

2.6.4 Magnetostatic self-energy

The last term entering the micromagnetic energy (2.43) is known as the self-energy of the FM. It is a natural consequence of Maxwell's law for the divergence freedom of the Flux density (2.6). With the constitutive relation $\mathbf{B} = \mu_0(\mathbf{M} + \mathbf{H}_m)$ it follows

$$\nabla \cdot \mathbf{M} = -\nabla \cdot \mathbf{H}_m. \quad (2.49)$$

According to the Helmholtz theorem for vector fields, one has $\mathbf{H}_m = -\nabla u + \nabla \times \mathbf{a}$. Furthermore, since no free conduction currents are considered, Ampère's law states that $\nabla \times \mathbf{H}_m = \mu_0 \mathbf{j}_{\text{free}} = \nabla \times \nabla \times \mathbf{a} = 0$ and consequently $\mathbf{a} = \nabla a_0$ and $\mathbf{H}_m = -\nabla u$. That means divergences of the magnetization have to be compensated by a stray field \mathbf{H}_m to ensure that $\nabla \cdot \mathbf{B} = 0$. Equation (2.49) now takes on the form

$$\nabla \cdot \mathbf{M} = \rho_M = \Delta u. \quad (2.50)$$

This formula also appears in classical electrostatics, describing the relation between a charge density ρ and the corresponding field $\phi \hat{=} u$. Therefore, the divergence of \mathbf{M} is often seen as a magnetic charge. At the surface of the FM, the divergence of \mathbf{M} has the most prominent effect and causes the generation of a macroscopically measurable field \mathbf{H}_m known as stray field. Inside the material, the magnetic self field is also called the demagnetization field since it tends to drive the FM into a state that minimizes magnetic charge. This tendency of demagnetization manifests itself in the appearance of magnetic domains inside the material. The shape and extent of these domains is determined by the interplay between demagnetization, anisotropy, and exchange, where the latter two favor uniform magnetization. In soft FMs, the minimization of the self-field energy can manifest itself in the formation of magnetic vortex states. In thin films, the stray field can be minimized by forcing the magnetization along a certain in-plane direction. This stray field induced preferential direction of \mathbf{M} is often called shape anisotropy, an effect that purely depends on the geometry of the sample. In contrast to the strong short-range exchange forces, the dipolar interaction between magnetic moments is long-ranged. The free-energy density associated with the magnetic self field can be written as [171]

$$g_s = \frac{\mu_0}{2} \mathbf{M} \cdot \nabla u. \quad (2.51)$$

2.6.5 Landau-Lifschitz-Gilbert equation

The equilibrium state of the FM depends on the various interactions between the magnetic moments in the sample. The combination of these interactions acts like an effective magnetic field that locally tries to align the magnetization into an energetically favorable direction. In equilibrium, therefore, the following condition holds [171]

$$\delta G = -\mu_0 \left[\int \mathbf{H}_{\text{eff}} \cdot \delta \mathbf{M} \, dV - \frac{2A}{\mu_0 M_s^2} \oint_{\Omega_{\text{FM}}} \frac{\partial \mathbf{M}}{\partial \mathbf{n}} \cdot \delta \mathbf{M} \, dS \right] = 0. \quad (2.52)$$

Variations in the free energy due to variations in the direction of \mathbf{M} are supposed to be zero since $M_s = \text{const.}$. By carrying out the variational procedure, it is straightforward to show that the effective field takes on the form

$$\mathbf{H}_{\text{eff}} = -\frac{1}{\mu_0} \frac{\delta G}{\delta \mathbf{M}} = \frac{2A}{\mu_0 M_s^2} \Delta \mathbf{M} + \frac{2K_1}{\mu_0 M_s^2} (\mathbf{M} \cdot \mathbf{e}_a) \mathbf{e}_a + \mathbf{H}_{\text{ext}} - \nabla u. \quad (2.53)$$

The surface integral appearing in (2.53) is a natural consequence of minimizing the exchange term in the free energy. It can be eliminated by applying the boundary condition

$$\frac{\partial \mathbf{M}}{\partial \mathbf{n}} = \sum_{i=1}^3 (\nabla M_i) \cdot \mathbf{n} = 0, \quad \text{on} \quad \partial \Omega_{\text{FM}} \quad (2.54)$$

which is valid in the absence of surface anisotropy. Under the action of (2.53), the magnetization is locally precessing and obeys the conventional dynamic equation for a magnetic moment in an external magnetic field

$$\frac{\partial \mathbf{M}}{\partial t} = -\gamma \mu_0 \mathbf{M} \times \mathbf{H}_{\text{eff}}. \quad (2.55)$$

The prefactor γ is the gyromagnetic ratio of the electron spin and has a value $\gamma = gq_e \hbar / 2m_e$ with a Landé-factor $g \approx 2$. Remarkably, the precessional frequency is not dependent on the angle between the magnetic moment and the effective field. This behavior is also known from the quantum mechanical description of magnetic moments. In that sense, equation (2.55) is not very realistic since a constant precessional motion does not allow the FM to find an equilibrium state where $\mathbf{M} \times \mathbf{H}_{\text{eff}} = 0$. This obstacle was overcome by Landau and Lifschitz, who proposed that relaxation could be achieved by adding a damping term to (2.55) [179]. However, even though the new form of (2.55) was able to give qualitatively correct magnetodynamics, in many cases, it still predicted incorrect behavior in the limit of strong damping. An improved version of the Landau-Lifshitz equation, valid also in the high damping regime, was developed by T. L. Gilbert [180]

$$\frac{\partial \mathbf{M}}{\partial t} = -\gamma^* \mathbf{M} \times \mathbf{H}_{\text{eff}} + \frac{\Gamma}{M_s} \mathbf{M} \times \frac{\partial \mathbf{M}}{\partial t}. \quad (2.56)$$

This equation is commonly known as the Gilbert equation. Mathematically, the original Landau-Lifshitz equation and (2.56) are representatives of a class of equivalent differential equations differing only in the definition of the constants. For this reason, dynamic equations of the form (2.56) are often referred to as Landau-Lifshitz-Gilbert equation. In this work, the same name convention will be used. Representatives of the

LLG-equation have to obey two principles: conservation of the magnetization amplitude $|\mathbf{M}| = \text{const.}$ and the equilibrium condition between the local magnetization and the effective field $\mathbf{M} \times \mathbf{H}_{\text{eff}} = 0$. It can be easily shown that the LLG-equation (2.56) fulfills both conditions. The damping term is as well constructed to fulfill these requirements. It has the form of a torque that drives the magnetic moment into the direction of the effective field. The combined action of the two torque terms in the LLG-equation leads to a spiral trajectory of \mathbf{m} on the Bloch-sphere (see Fig. 2.3). The gyromagnetic factor

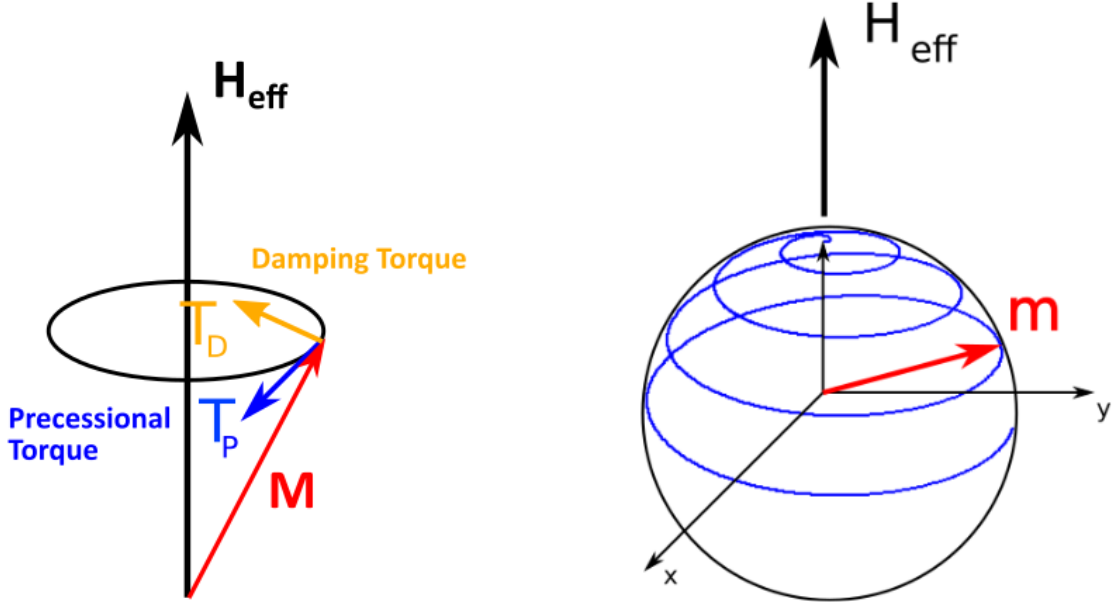


Figure 2.3: Damped precessional motion of a magnetic moment due to an effective field. Left: damping torque T_D and precessional torque T_P acting on the magnetization \mathbf{M} . Right: Trajectory of \mathbf{m} on the Bloch sphere.

appearing in the LLG equation is, in general, a function that depends on the state of the system as well as damping. For simplicity, in most cases, only the latter is considered. By comparing the Landau-Lifschitz-equation and the LLG-equation one can show that $\gamma^* = \gamma_L(1 + \Gamma^2)$ where often $\gamma_L = \gamma$ is used [180]. In cases where the total angular momentum of the unpaired electrons has a significant contribution from the orbital angular momentum, the precessional factor needs to be adjusted accordingly.

2.6.6 Spin waves

Under the action of the effective magnetic field (2.53), the energetic ground state of a FM corresponds to regions of approximately uniform magnetization but different orientations. The exchange interaction forces neighbored spins to equally align inside each domain, as described by the Heisenberg-operator (2.44). Inverting the direction of one moment is energetically costly. However, suppose such a deviation from the ground state is uniformly distributed across the spin system. In that case, neighbored moments will only be slightly canted, and the penalty in exchange energy will be less severe. The corresponding periodic modulations of the spin system are called spin waves, as depicted

in Fig. 2.4(a). Spin waves or magnons (in reference to their energy-excitation quanta)

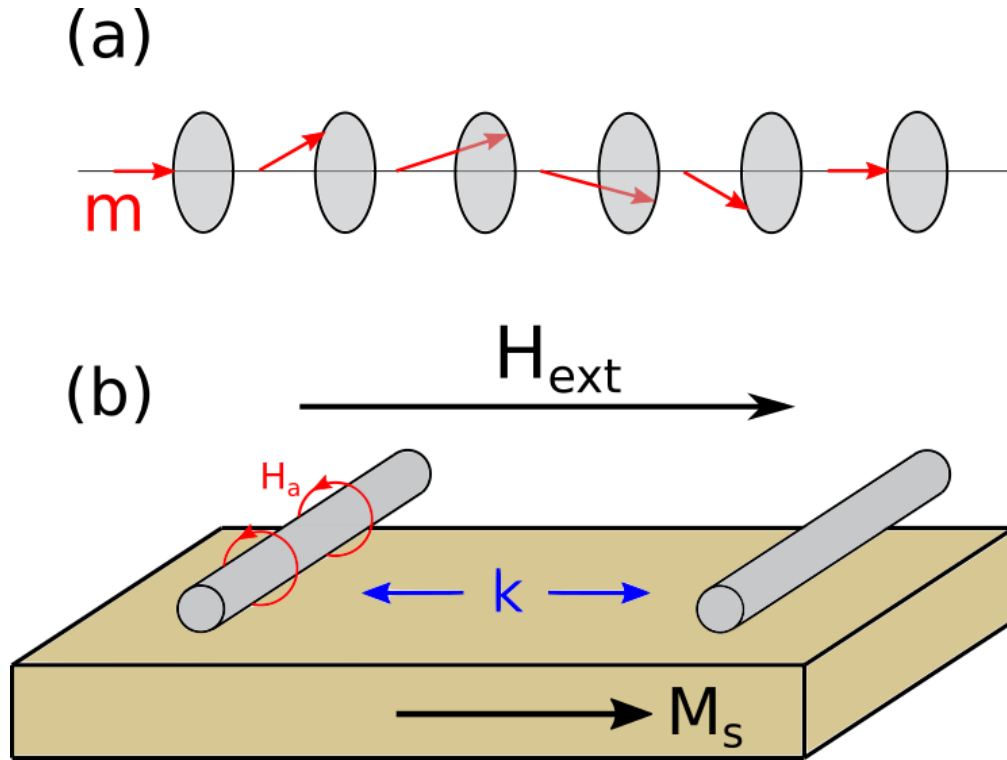


Figure 2.4: (a) spin wave propagating along a chain of magnetic moments \mathbf{m} . (b) schematic experimental setup for magnon propagation in a waveguide of backward volume magnetostatic spin wave (BVMSW) configuration. The left antenna is fed by a microwave current giving rise to a time-dependent excitation field \mathbf{H}_a . The right antenna serves for magnon detection.

are dynamic collective excitations of the ferromagnetic ground state. Technically they are similar to phonons - the collective excitations of the atomic lattice of a solid. Both are bosonic in nature and carry a quantized amount of energy. However, the relation between wave vector \mathbf{k} and frequency f has a complicated form for magnons. In particular, it depends not only on the underlying material but also on the mutual orientation between the magnetic field and propagation direction. In addition, in a FM, the coupling between neighbored magnetic moments has contributions from short-range exchange interactions and long-range dipolar interactions making a systematic study of $f(\mathbf{k})$ challenging. Dipolar coupling dominates the spin-wave dispersion for $|\mathbf{k}| \ll 1$ and in large probe geometries. Here the mutual orientation between \mathbf{k} and \mathbf{H}_e determines the propagation characteristics of magnonic excitations (see, e.g., [181]). In the following, only the so-called backward volume magnetostatic spin wave (BVMSW) configuration is considered, as shown in Fig. 2.4 (b). In this particular case, the external bias field of the FM is oriented parallel to the propagating modes, i.e., $\mathbf{H}_e \parallel \mathbf{k}$. In contrast to surface waves, volume modes are characterized by a nonvanishing amplitude of the spin waves in the entire volume of the sample. The term "backward volume" refers to the property $v_p v_g < 0$ meaning at (k_1, f_1) the phase velocity $v_p = f_1/k_1 > 0$ is opposite to the group

velocity $v_g = \partial f / \partial k < 0$. The exact frequency interval for which this property holds depends on the sample geometry and the internal field \mathbf{H}_{eff} of the waveguide. A typical BVMSW spectrum (except for the band gaps) is shown in 6.5 (d).

Due to its high potential for applications in information technology, the research in magnonics has grown exponentially in recent years [182,183]. Various proposed magnonic device ideas include spin wave filters, emitters, logic devices, diodes, and integrated circuits. One of the key ideas for magnonic logic applications is tailoring the spin wave dispersion, allowing the control of information transfer through a waveguide. For example, this can be done by introducing periodic modulations to chosen system parameters, such as waveguide thickness [184], external magnetic field [85], magnetic texture [185] or material parameters [186]. In this way, a so-called magnonic crystal [187–189] can be constructed, which is the magnetic analog to a photonic crystal [190,191]. However, magnonic crystals have several advantages over their optical counterpart, e.g., lower energy consumption, smaller wavelength, and smaller device features [183]. The basic idea of periodically patterned materials is that propagating waves subsequently scatter at the introduced nonuniformity. Then, due to destructive interference, waves in a certain frequency interval are not allowed to propagate inside the crystal. The corresponding frequency regime is called a band gap. Controlling the width and number of these forbidden bands is one of the driving factors for research in magnonics. Here only a rough introduction to this vast research field can be given. The literature is referred to for further information about magnonics and magnonic crystals.

3 Numerical procedure

This section presents the methods for the numerical solution of the TDGL-equations and the LLG-equation. First, the superconducting subsystem and the numerical treatment of the TDGL are discussed. The numeric integration scheme for the LLG and methods for calculating the magnonic dispersion are introduced afterward.

Before the actual solution method for the TDGL-system (2.33)-(2.34) is presented, it is useful to make the equations dimensionless by applying a suitable scaling. For this reason, the superconducting order parameter $\Psi = \Psi_\infty(T_0)\tilde{\Psi}$, the position vector $\mathbf{r} = L\tilde{\mathbf{r}}$, the time $t = \tau\tilde{t}$, the vector potential $\mathbf{A} = \sqrt{2}B_{\text{cth}}(T_0)L\tilde{\mathbf{A}}$, the magnetic flux density $\mathbf{B} = \sqrt{2}B_{\text{cth}}(T_0)\tilde{\mathbf{B}}$, the temperature $T = T_c\tilde{T}$, the supercurrent density $\mathbf{j}_s = \sqrt{2}B_{\text{cth}}/\mu_0\lambda_{\text{GL}}\tilde{\mathbf{j}}_s$ and the scalar potential $\phi = \sqrt{2}B_{\text{cth}}(T_0)\lambda_{\text{GL}}(T_0)^2/\tau\tilde{\phi}$ are set in relation to their dimensionless quantities which are denoted by a tilde. In the following, the tilde is omitted, and only the dimensionless variables are considered. Equation (2.33) is divided by $|\alpha(T_0)|$ and (2.34) by $\sqrt{2}B_{\text{cth}}(T_0)/\mu_0\lambda_{\text{GL}}$. The dimensionless TDGL equations now have the form

$$\eta_1 \left(\frac{\partial \Psi}{\partial t} + i\kappa\phi\Psi \right) + \Psi \left(|\Psi|^2 - 1 + \frac{T - T_0}{T_c - T_0} \right) + \left(\frac{1}{in\kappa} \nabla - n\mathbf{A} \right)^2 \Psi = 0, \quad (3.1)$$

$$\frac{1}{n} \nabla \times \nabla \times \mathbf{A} = -\eta_2 \left(n \frac{\partial \mathbf{A}}{\partial t} + \frac{1}{n} \nabla \phi \right) + \mathbf{j}_s, \quad (3.2)$$

$$\mathbf{j}_s = \frac{i}{2n\kappa} (\Psi \nabla \Psi^* - \Psi^* \nabla \Psi) - n|\Psi|^2 \mathbf{A}, \quad (3.3)$$

with boundary condition

$$\left(\frac{1}{in\kappa} \nabla \Psi - n\Psi \mathbf{A} \right) \cdot \mathbf{n} = 0, \quad \text{on} \quad \partial\Omega_{\text{SC}}. \quad (3.4)$$

The boundary condition for (3.2) will be specified later. The constants appearing in the rescaled TDGL equations are

$$\eta_1 = \frac{\xi_{\text{GL}}(T_0)^2}{D\tau}, \quad (3.5)$$

$$\eta_2 = \sigma \frac{\mu_0\lambda_{\text{GL}}(T_0)^2}{\tau}, \quad (3.6)$$

$$n = \frac{L}{\lambda_{\text{GL}}(T_0)}. \quad (3.7)$$

The measures for time (τ), space (L), and the operating temperature (T_0) are chosen according to the problem at hand. A common choice is to set $\tau = \xi_{\text{GL}}(T_0)^2/D$, $\sigma = 1/(\mu_0\kappa^2 D)$ and $L = \lambda_{\text{GL}}(T_0)$ which sets the constants to unity [69, 76, 115, 192]. In the

dirty limit, one has $\eta_1 \approx 1$, which is a commonly accepted parameter in the literature and known to lead to qualitatively and sometimes even quantitatively correct results [193]. In the following calculations, the superconducting material is chosen to be Nb. Niobium is the elemental SC with the highest critical temperature $T_c \approx 9$ K and a natural type-II-material with $\kappa \geq 0.8$ [28]. Depending on its purity, Nb can host vortices with comparably large cores and strong stray fields. All these properties make Nb especially suitable for studying superconducting vortices under various conditions. The material properties of Nb are therefore well studied and can be easily found in the literature [27, 44, 98].

In the first TDGL-equation (3.1) the temperature-dependent expression

$$f(T) = -1 + \frac{T - T_0}{T_c - T_0} \quad (3.8)$$

becomes zero if $T = T_c$ and -1 if $T = T_0$. That means that in equilibrium and under zero external field, the SC is in the Meißner state. In this case the order parameter is homogeneous and $0 = |\Psi_\infty(T_c)|^2 \leq n_s \leq |\Psi_\infty(T_0)|^2 = 1$.

In most cases, (3.1) and (3.2) are solved numerically by the use of either the finite-difference method (see [192] and references therein) or the finite element method (FEM) [194, 195]. Finite difference schemes are usually faster than the FEM and allow large-scale simulations of systems of micrometer size and beyond [196]. On the other hand, the FEM allows the solution of the TDGL equations on superconducting samples of complex shapes, like spheres, tubes, or geometries that are taken from real experiments. In the following, only finite-sized SCs are considered, where geometric confinement effects are important. For this reason a linearized semi-implicit Galerkin-mixed FEM is used for the simultaneous solution of (3.1)-(3.4) [194]. The computations are carried out with the FEM software FEniCS [195] and generation of finite-element meshes is done with the open source 3D finite element mesh generator GMSH [197]. Depending on the problem at hand, boundary conditions and element orders are adapted to match specific requirements. Details about these modifications will be provided in the corresponding text passages. A detailed discussion of the FEM is beyond the scope of this work. For more information, the reader is referred to the literature, e.g., [198, 199].

In many cases, solving the LLG equation is quite involved. The solution of (2.56) is a 3D vector field that fulfills the constraint $|\mathbf{m}(\mathbf{r})| = 1$ at all times. Also, calculating the dipolar field $\mathbf{H}_m = -\nabla u$ is numerically demanding. So, the numerical solution of the LLG equation is performed with the micromagnetic simulation program MuMax3 [200]. This software package uses a finite-difference discretization scheme where the ferromagnetic sample is uniformly subdivided into a grid of orthorhombic cells. The output data of MuMax3 consists of a number of arrays for each magnetization component $m_{x,y,z}(t_j)$ and each instance of simulation time t_j . Each value of the arrays corresponds to the local magnetization component at a specific grid site.

In Chapter 6, the considered magnetic samples consist of long Py strips subjected to an external bias field \mathbf{H}_\parallel , which points along the strip's central axis. If $\mathbf{H}_\parallel = H_\parallel \mathbf{e}_x$, the equilibrium solution of the LLG equation consists of the vector field $\mathbf{m} = \mathbf{e}_x$. Note that shape anisotropy supports such a magnetization alignment since, in this way, the magnetic charge $\nabla \cdot \mathbf{m}$ inside the waveguide can be minimized. Dynamic deviations from the equilibrium solution appear if the magnetization is locally stirred, e.g., by the

Oersted field of a microwave antenna. The magnetic disturbance travels through the waveguide as a spin wave with a specific, mode-dependent frequency $f(\mathbf{k})$. In the following, the orthogonal magnetization components will be denoted as $\delta m_{y,z}$. In particular, the orthogonal magnetization component $\delta m_z(x, y_0, z_0, t)$ will be used to calculate the waveguide's spin wave dispersion. Here, $\delta m_z(x, t)$ is evaluated along the waveguide's central axis, and y_0 and z_0 are chosen accordingly. The spinwave dispersion can be calculated by applying a 2D Fast Fourier transform (FFT) to the 2D matrix $\delta m_z(x_i, t_j)$ yielding $\delta \hat{m}_z(k_i, f_j)$. The maxima of the Fourier amplitudes correspond to modes that are allowed to travel along the waveguide. By transforming the array $|\delta \hat{m}_z(k_i, f_j)|$ into a pseudocolor image, e.g., by using the Python library Matplotlib [201], the entire spectrum can be visualized. The spatial distribution of a specific mode can be found by evaluating $F_t \delta m_z(x_i, t_j) = \delta \hat{m}_z(x_i, f_j)$ and inspecting the local magnetization in the frequency domain.

Before applying the FFT it is advisable to multiply the magnetization array by an appropriate window function to avoid FFT-specific errors like scalloping loss [202]. In the here-presented calculations $\delta m_z(x_i, t_j)$ is multiplied by Hanning windows [203]

$$H_t(t) = \frac{1}{2} \left(1 - \cos \left(\frac{2\pi j}{M-1} \right) \right), \quad 0 \leq j \leq M-1, \quad (3.9)$$

$$H_x(x) = \frac{1}{2} \left(1 - \cos \left(\frac{2\pi i}{N-1} \right) \right), \quad 0 \leq i \leq N-1. \quad (3.10)$$

Here, M and N correspond to the number of samples over time and space. The sampling rates are chosen to match the requirements of the dispersion plots. For example, by using a sinc-field $\mathbf{H}_a = H_0 \sin(2\pi f_0 t) / (2\pi f_0 t) \mathbf{e}_y$ to excite spin waves, only modes with frequencies $f < f_0 = 20$ GHz are excited. Therefore, it is sufficient to evaluate δm_z every $\Delta t = 25$ ps giving the calculated spectrum an upper bound (Nyquist frequency) of $f_{\text{Nyquist}} = 0.5/\Delta t = 20$ GHz. On the other hand, the resolution in frequency space is determined by the total simulation time $T = M\Delta t$. The simulations in Chapter 6 were run for $T = 1$ μ s allowing for a resolution of $\Delta f = 1/T = 1$ MHz. Similar arguments can be made for the spatial sampling of δm_z . Here, the cell size l of the finite difference grid determines the maximum wave vector $k_{\text{Nyquist}} = \pi/l$ that can be resolved, whereas the waveguide length $L = Nl$ determines the resolution in k -space. For more information about magnonic dispersion calculations, see, e.g., [202].

4 Controlled vortex formation at nanostructured superconductor/ferromagnetic junctions

Coupling between superconducting and ferromagnetic matter can be achieved in two ways. For directly coupled FM/SC hybrids, the two system constituents are in physical contact. Thereby, the ferromagnetic correlations usually prevail since they have a strong pair-breaking effect on the superconducting condensate. As a result, superconductivity is suppressed around the FM/SC interface. On the other hand, if the ferromagnetic order is weakly developed, the competition between FM and SC is more balanced. In such a system, novel effects may appear, e.g., a direct coupling between the magnetic spin system and the superconducting phase field, leading to anomalous supercurrents at the material interface. This effect will be discussed in detail in Chapter 5.

In many applications and theoretical studies, the direct proximity effect is avoided by separating the two sub-systems by an insulating interlayer. In this way, the system constituents only interact via their corresponding stray field. The following section deals with such an electromagnetically coupled FM/SC hybrid system.

The results presented in this chapter are based on studies of vortex patterns in confined FM/SC bilayers, published by the author of this thesis [204]. In this section, it will be discussed how the stray field of a patterned nanomagnet affects vortex nucleation in a nearby SC. It will also be shown how an external magnetic field can be used to precisely control the total vorticity of the FM/SC hybrid structure. Here the old results will be reviewed, and an outlook will be given on how the research in the field might be continued.

The three main parameters in the TDGL-equations that determine the solution of (3.1) and (3.2) are the material constants, the boundary conditions, and the external vector potential. For this reason, the major part of publications in the field of vortex physics deals with problems related to modifying these system parameters. In many of these works, several simplifying assumptions are made to keep the computational effort tractable. For example, the assumption of an infinitely long superconducting prism along the z -direction allows to neglect the z -dependence of the superconducting order parameter Ψ and vector potential \mathbf{A} and renders the system essentially two-dimensional. Additionally, for such a system geometry, demagnetization effects do not occur, which allows simplification of the boundary conditions for the magnetic field [194]. Another simplification method is to neglect the superconducting stray field completely and solve only the first TDGL for a given external vector potential. This approach is valid in thin films and nano-sized systems or in other cases where the superconducting stray field is negligible compared to the external field [73]. In films of intermediate thickness, such

a simplification becomes less appropriate since demagnetization effects due to the superconducting stray field become important. Also, superconducting vortices can behave differently in extended systems and tend to form loops [66, 67, 73], semi-loops [58, 68] and connected networks [56]. That is often the case if the SC is subject to the stray field of a nearby FM. Also, the superconducting stray field and material inhomogeneities play an important role in extended geometries and lead to a complicated vortex-vortex interaction. The statics and dynamics of such systems are difficult to investigate since they often appear only in samples of macroscopic size. Hence, the computational effort for computer simulations becomes enormous. For this reason, the amount of literature in the field is rather limited. On the other hand, the potential for applications is high since artificial FM/SC compounds are known to give rise to effects that can not be observed in each of the systems separately.

For this reason, this work investigates how superconducting films of intermediate thickness behave in the vicinity of a FM with a distinct domain structure. The stray field of such a magnet is highly inhomogeneous in space and has the potential to induce VAV systems in the nearby SC. It will be shown that in conjunction with additional external magnetic fields, the vorticity of the system can be precisely controlled and allows to perform logic operations based on the vortex state of the SC. Also, the transport properties of the SC are expected to be strongly modified by the FM since they are inherently coupled to the vortex dynamics. The presented findings are also interesting from a fundamental point of view since 3D-simulations of vortex states in highly confined geometries and in the presence of inhomogeneous magnetic fields are rarely to be found in the literature.

4.1 Simulation details

A sketch of the domain of computation is shown in Fig. 4.1. The SC has a square geometry and is located on top of a FM of the same size. Both layers have a side length of $a = 2 \mu\text{m}$, a thickness of $d = 200 \text{ nm}$ and are separated by a thin insulating oxide layer of height $h = 20 \text{ nm}$. The insulator prevents direct proximity between the materials and makes the interaction between the system constituents purely electromagnetic. The entire trilayer is surrounded by a vacuum and placed in a cubic box of side length $b = 10 \mu\text{m}$. In general, the magnetization \mathbf{M} of the FM and the superconducting order parameter Ψ will, by mutual interaction, find an equilibrium state which minimizes the free energy of the entire system. Even though it is an interesting process, the relaxation of the entire system is not considered here. Instead, the FM will be set to have a fixed magnetization of strength and direction that are chosen freely. The ferromagnetic component is assumed not to be affected by external fields of any kind and only serves as a magnetic field source. In the following, the operating temperature will be set to $T_0 = 8.26 \text{ K}$, corresponding to $T_0 = 0.92 T_c$ with $T_c = 9 \text{ K}$ for Nb. The state of the SC is calculated by solving the dimensionless TDGL-equations (3.1) and (3.2). The material constants of Nb are taken from the literature and displayed in table 4.1 [29, 44]. In order to simplify the problem, the gauge $\phi = 0$ is chosen [97]. Therefore, the superconducting wave function and the vector potential are the only quantities to be calculated. The latter can be split into several contributions $\mathbf{A} = \mathbf{A}_e + \mathbf{A}_{\text{FM}} + \mathbf{A}_s$ where \mathbf{A}_e is the vector

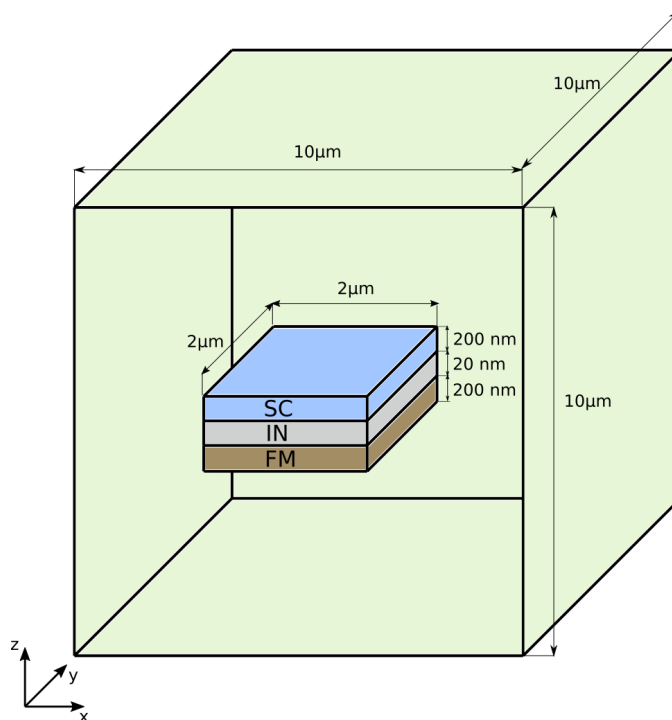


Figure 4.1: Sketch of the considered FM/SC hybrid structure. The SC is a square film made from Nb. It is separated from the FM by a thin insulating oxide layer. The surrounding empty box is for the computation of the vector potentials, which are supposed to fulfill open boundary conditions.

| | Quantity | Value |
|----------------------------|----------------|----------------------------------|
| Magnetic penetration depth | λ_{GL} | 266 nm |
| GL-parameter | κ | 3.4 |
| Basic time unit | τ | 3.3 ps |
| Basic length unit | L | 266 nm |
| Mean free path | l | 9 nm |
| Fermi velocity | v_f | $6 \times 10^5 \text{ m s}^{-1}$ |
| Relative temperature | T/T_c | 0.9175 |
| Length ratio | n | 1 |
| First TDGL coefficient | η_1 | 1 |
| Second TDGL coefficient | η_2 | 0 |

Table 4.1: Material parameters of Nb and the quantities used in the calculations. [204]

potential of homogeneous external fields, \mathbf{A}_{FM} is the potential of the ferromagnetic flux density, and \mathbf{A}_s corresponds to the superconducting stray field. From Ampère's law, it follows

$$\frac{1}{\mu_0} \nabla \times \nabla \times \mathbf{A}_{FM} = \nabla \times \mathbf{M}. \quad (4.1)$$

Equations (3.2) and (4.1) are solved with open boundary conditions for \mathbf{A}_s and \mathbf{A}_{FM} and the corresponding fields tend to zero at infinite distance from the sample. This boundary condition is approximated by setting the following Dirichlet condition for the vector potentials

$$\mathbf{A} \times \mathbf{n} = 0 \quad \text{at} \quad \partial\Omega \quad (4.2)$$

where $\partial\Omega$ denotes the outer boundary of the box. The condition (4.2) enforces $\mathbf{B} \cdot \mathbf{n} = 0$ at the boundary, i.e., the whole system is surrounded by a perfectly diamagnetic material that screens all fields. Under these conditions, it is known that the FEM delivers acceptable numeric results if the distance from the center of the sample towards the box edges is about five times the distance between the center and the outer surface of the sample [205]. Numeric accuracy also requires a sufficiently high amount of finite-element cells outside the sample. These conditions are fulfilled with the above-shown geometry and the usage of ten million cells outside the sample and about one million cells in each layer.

In principle, the ferromagnetic vector potential could also be calculated analytically from (2.32). Both methods were tried out, and the results were confirmed to be identical. The numeric procedure is now the following. Equation (4.1) is solved for $\mathbf{M} = M_0 \mathbf{m}$ with $M_0 = 1 \text{ kA/m}$ and unit vector \mathbf{m} for a chosen magnetic configuration. The vector potential \mathbf{A}_{FM} is inserted into the first TDGL equation, and the equation is solved for a slowly increasing field. This procedure is possible since Ampère's law scales linearly with the magnetization amplitude. Once the desired field value is reached, the system is allowed to relax, and the equilibrium order parameter Ψ and supercurrent \mathbf{j}_s are calculated. With \mathbf{j}_s at hand, the stray field \mathbf{A}_s of the SC is calculated by solving the second TDGL equation. This field is then reinserted into the first TDGL equation, and the relaxation procedure starts again. The equilibrium state of the system is usually reached after two relaxation cycles, and the state of the system is evaluated. Since only equilibrium states are of interest here, the effect of normal currents is not considered, and $\eta_2 = 0$ is set. Technically, it would also be possible to directly solve the static GL-equations selfconsistently for Ψ and \mathbf{A}_s . However, the solution of the classic GL-equation is much more difficult than solving the time-dependent problem. For the external vector potential, the symmetric gauge $\mathbf{A}_e = 0.5B_e(-y\mathbf{e}_x + x\mathbf{e}_y)$ is chosen. The corresponding flux density $\mathbf{B}_e = B_e\mathbf{e}_z$ is the field at the center of a very long solenoid. This particular field matches the setup where a conventional Helmholtz coil produces the external field.

4.2 Results and discussion

In the following, several magnetic configurations will be considered, and it will be shown how they affect the state of the SC. Specifically, the magnetization of the FM shown in Fig. 4.1 is now divided into several domains. In the first case, the FM consists of two domains of opposite magnetization separated by a domain wall of negligible size (see Fig. 4.2). The saturation magnetization, in this case, is assumed to be $M_s = 75 \text{ kA/m}$, a realistic but relatively weak value compared to the magnetization of standard materials like Permalloy (600 – 1900 kA/m) or YIG (140 kA/m).

Such a weak magnetization is chosen because of the comparably small separation between the layers. At close distances, conventional FMs produce a stray field that is strong

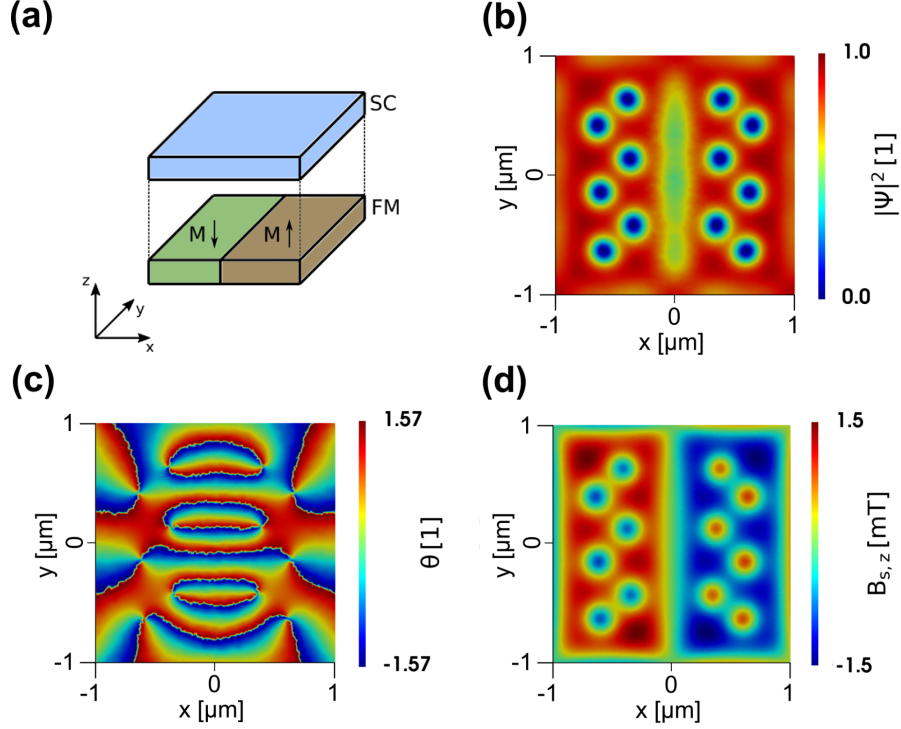


Figure 4.2: State of the FM/SC bilayer where the FM consists of two domains of opposite magnetization direction. No additional external fields are applied, and the saturation magnetization is set to $M_s = 75$ kA/m. (a): Sketch of the system geometry. (b): Order parameter amplitude $|\Psi|^2$ on a slice through the center. (c): phase θ of the wave function. (d): z-component of the superconducting stray field \mathbf{B}_s .

enough to substantially suppress the superconducting state, especially at temperatures close to the critical temperature of the SC. That means, in close proximity to the FM, vortex states appear already at small magnetization values. These states with a comparably small number of fluxons are of primary interest in this work since they already reflect the principal behavior of the system very well. Furthermore, at small distances, the stray field of the FM reflects very well the actual state of the magnetization and the shape of the magnet. So the geometry of the magnetic layer becomes an important parameter in the problem.

For the system shown in Fig. 4.2, the stray field is relatively homogeneous above each domain, but its sign rapidly changes at the domain wall. Also, directly above the domain wall, the stray field has its strongest magnitude and the greatest effect on the SC. Here, under slowly increasing magnetization, the superconducting order parameter is gradually suppressed, leading to the formation of a pocket of reduced superconductivity. For sufficiently large magnetization, this region becomes unstable, and dynamic vortex nucleation sets in. In the final stage of the process, the normal conducting region collapses into a vortex semi-loop. Despite the sample's comparably large thickness $d \approx 2.5 \xi_{GL}$, the semi-loop is unstable and splits into two independent fluxons. Driven apart by the strong Meissner currents above the domain walls, each fluxon travels into a region that

magnetically stabilizes it. The stabilizing mechanism here is the attractive interaction of current loops of opposite flow directions.

On the one hand, the Meissner currents above each ferromagnetic domain are directed oppositely to the magnetization current of the underlying ferromagnetic texture. In this way, the magnetic stray field is expelled from the SC. On the other hand, the screening currents flowing around the vortices have the opposite polarity. Therefore, fluxons with a certain magnetic moment will preferably assemble above magnetic domains that share the same polarity. In this way, the conventional Meißner currents and the fluxonic currents cancel to some extent, and the energy of the system is reduced.

This is also reflected in the stray field produced by the fluxons. The z-component of \mathbf{B}_s points in the same direction as the stray field of the underlying ferromagnetic domain. As the magnetization increases further, more and more fluxons enter the sample. Vortex creation, in this case, happens not only at the center of the SC but also at its edges, like under the action of a homogeneous magnetic field. The fluxons form two seemingly independent lattices and populate the domains according to their polarity. However, superconducting vortices are topological entities, so their presence affects the entire SC. By looking at the superconducting phase, it becomes apparent that, despite their spatial separation, the VAV-pairs are still connected. The phase gradient of a vortex opposes that of an antivortex, and under normal conditions, both entities attract each other and annihilate. In the present case, the current flow at the domain wall prevents annihilation, and the two fluxon subsystems are stable. Also, vortex expulsion through the edges is prevented by the magnetic barrier. Without additional magnetic fields, fluxons in the considered system can only appear in pairs. That is because the total flux provided by the FM is zero, and the vorticity of the SC has to follow this tendency to minimize energy.

The situation is similar if the FM is divided into four domains, as shown in Fig. 4.3. Such a magnetic configuration can be experimentally reproduced by combining four magnetic plaques into the considered structure. Since the volume of each domain is now smaller than in the case of a two-domain system, the stray field is weaker as well. A higher magnetization is, therefore, necessary to generate vortices. Upon slowly increasing magnetization, vortex generation at the domain walls and the sample edges is observed again. In this case, the fluxons form stable systems above each domain with a polarity that matches the underlying magnetization direction. Due to symmetry, for all magnetizations, the number and arrangement of the fluxons is observed to be identical in each subsystem. This symmetry can be disturbed under the application of an external field. Concretely the additional field adds to the stray fields of the magnet and increases or decreases the total field in certain parts of the structure. E.g., For $\mathbf{B}_e = B_e \mathbf{e}_z$, the fluxons in the lower left and upper right corner experience an increased magnetic flux. As a result, the corresponding vortex lattices shrink in size. On the other hand, the antivortex lattices at the lower right, and upper left corner expand since the external field counteracts the magnetic stray field. If the external magnetic field is strong enough, it can change the number of vortices in the sample. In this way, it is possible to reduce the fluxon number to zero in domains where the external and ferromagnetic fields cancel each other. In the remaining domains, superconductivity is strongly reduced under the action of the external field. At this point, it should be mentioned that in a more realistic system, the magnetization of the plaques might very well have in-plane

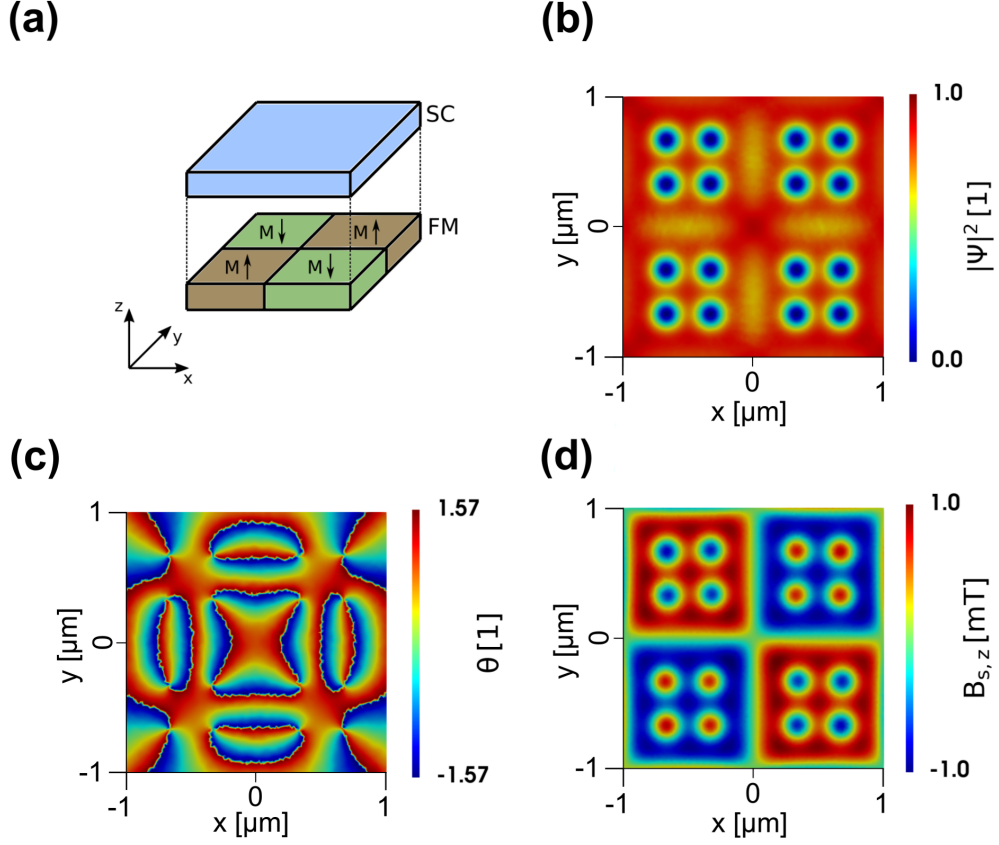


Figure 4.3: State of the FM/SC bilayer where the FM consists of four domains of opposite magnetization direction. No additional external fields are applied, and the saturation magnetization is chosen to be $M_s = 95 \text{ kA/m}$. (a): Sketch of the system geometry. (b): Order parameter amplitude $|\Psi|^2$ on a slice through the center. (c): phase θ of the wave function. (d): z-component of the superconducting stray field \mathbf{B}_s .

components, and the field acting on the SC is reduced to some degree. Also, the width of the domain walls is nonzero, and the stray field is modified accordingly [206, 207]. The fluxonic state presented here should be easily modifiable by altering the magnetic domain structure. That, together with the aid of external magnetic fields, provides the possibility of applications relying on precisely controllable fluxon systems [77–79]. Also, the superconducting stray field of VAV-systems might be used to control the magnon propagation in an adjacent magnetic waveguide.

So far, the geometry of the entire system has been relatively simple. Therefore, to put more emphasis on the geometry of the FM, the size and orientation of the layers are changed. The new geometry is shown in Fig. 4.4. As before, the SC sits on top of the FM, and an insulating layer separates both systems. The thicknesses of the layers and their quadratic geometry are also the same as before. But the FM is now rotated by 45 degrees with respect to the other layers. Also, its side length is reduced to $a = 1 \mu\text{m}$. Consequently, the SC now has two regions of opposite magnetic flux density. Directly above the FM, the field points mainly into the z-direction. Outside, it has the opposite

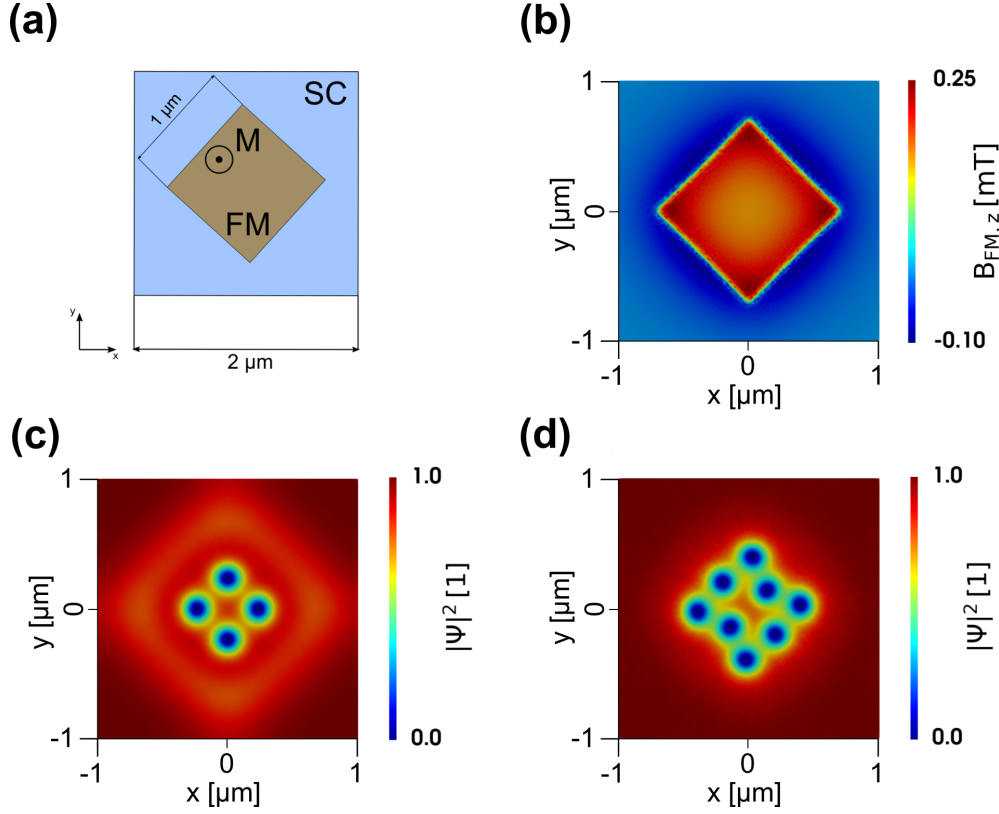


Figure 4.4: FM/SC bilayer-system with a ferromagnetic bottom layer of side length $a = 1 \mu\text{m}$ and a rotation of 45° with respect to the superconducting top layer. (a): geometry of the system. (b): magnetic stray field at the bottom of the superconducting layer for $M_s = 1 \text{ kA/m}$. (c), (d): state of the SC for a magnetization $M_s = 105 \text{ kA/m}$ and $M_s = 130 \text{ kA/m}$, respectively.

orientation. At the edges of the FM, the field orientation changes rapidly from positive to negative. If the superconducting layer were infinitely wide, the magnetic flux provided by the FM would be exactly zero. In the here-considered case, the SC is finite, and the flux is positive. That also becomes apparent if the magnetization is ramped up and the appearing vortices are investigated. In the absence of additional external fields, only vortices of distinct polarity are observed to gather above the domain of positive flux. However, in the process of fluxon generation, VAV-pairs were observed to appear at the corners of the FM. But due to finite-size effects and strong interaction with the Meissner currents, the antivortices are quickly expelled from the system. As a result, only vortices can populate the material and find a stable equilibrium. The situation is expected to be different for larger samples since the total flux tends to zero, and also, VAV-pairs should be able to stabilize [208]. With these observations at hand, it is straightforward to conceive a scenario where an additional external magnetic field restores the flux equilibrium in the system. However, before this idea is elaborated further, it is instructive to investigate how such a field modifies the superconducting state in the absence of magnetization.

The importance of geometric confinement in nano-SCs becomes especially apparent if the magnetization of the bottom layer is set to zero and the external field is slowly increased. Fig. 4.5 shows the resulting vortex arrangement. Under the action of a ho-

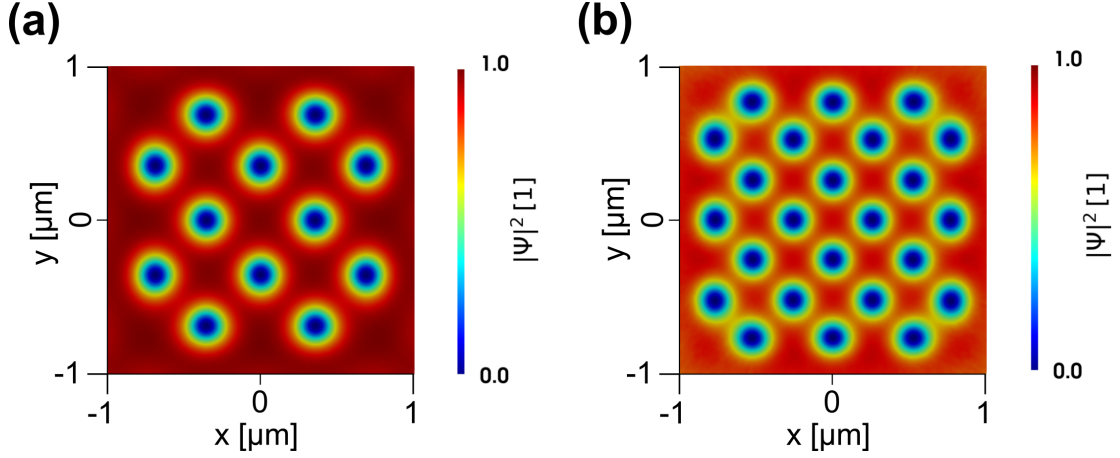


Figure 4.5: Vortex lattice for $M_s = 0$ and increasing external field $\mathbf{B} = B_e \mathbf{e}_z$. Left: $B_e = 8.5$ mT. Right: $B_e = 15.7$ mT.

mogeneous magnetic field, vortex generation solely happens at the sample edges, and vortices appear in multiples of four. Here the fourfold multiplicity is a natural consequence of strong geometric confinement. In nanosized SCs, it is typical for fluxons to arrange in a way that reflects the system geometry [209]. The influence of geometric confinement is also reflected by the symmetry of the Abrikosov lattice. In extended systems, vortices arrange in a lattice of hexagonal symmetry due to their mutual repulsion. In the here-considered case, the lattice has a simple cubic structure that is rotated by 45 degree compared to the sample geometry. However, the states depicted in Fig. 4.5 might be metastable, and the lattice potentially reconfigures into a sixfold symmetry over large time scales.

Now, it is discussed how a homogeneous external field can be utilized to manipulate the vortex state generated by a nearby FM. Starting point is the system shown in Fig. 4.4(c), where $M_s = 105$ kA/m and four vortices are present in the SC. The external field $\mathbf{B}_e = B_e \mathbf{e}_z$ is chosen to have a direction that opposes the direction of the stray field of the FM. Therefore, its presence reduces the magnetic flux in the system and stabilizes antivortices. Initially, the vortices sit at the center of the SC and are caged by circulating Meißner currents along the FM/SC interface. As the external field is increased, the negative magnetic flux outside the ferromagnetic domain is enhanced, and antivortices enter the system from the sample edges. For $B_e = 9.4$ mT, the fluxons of negative vorticity build a stable ring around the central region. In this case, the magnetic barrier around the FM/SC interface is strong enough to prevent VAV-annihilation. If the field is further increased, the magnetic flux at the center region gradually tends to zero, and the magnetic barrier becomes too weak to prevent fluxons from mutual annihilation. After reaching a new equilibrium, the center region is devoid of fluxons, and superconductivity is fully restored. Also, the number of antivortices has increased, and the total vorticity is negative. The observations made on this system show that careful adjustment of the

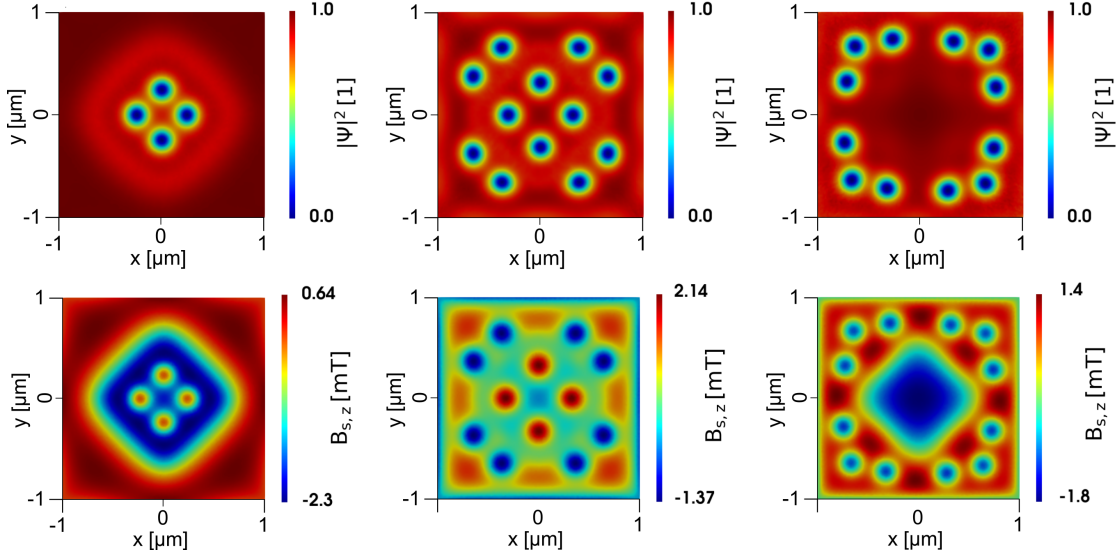


Figure 4.6: Upper panels: vortex states of the system shown in Fig. 4.4(c) for external magnetic field $\mathbf{B}_e = B_e \mathbf{e}_z$. The field amplitude increases from left to right and has values $B_e = 1.2$ mT (left), $B_e = 9.4$ mT (middle), $B_e = 12.3$ mT (right). Lower panels: z-component of the superconducting stray field \mathbf{B}_s for increasing external fields as in the corresponding upper panels.

external field allows for precisely controlling the SC's vorticity in this hybrid structure. Also, the size and geometry of the FM are important parameters in this problem since the vortices will adjust their position to the magnetic flux provided from outside.

The results evidence that vortex formation in FM/SC hybrid systems depends remarkably on the sample geometry- and size. It is demonstrated how a nanomagnet can serve as a field source in such a structure, enabling the formation of well-separated VAV-systems in the SC layer. The application of additional external magnetic fields allows further control of these fluxonic states. By adjusting the ferromagnetic domain structure and external field, it is possible to precisely control the vorticity of the SC layer enabling potential applications in fluxonic logic devices. Also, the stray field of the VAV-systems could serve as a building block for a dynamic magnonic crystal. This idea will be elaborated further in Chapter 6.

Due to the length restriction on the thesis, only a selected number of results were presented here. However, from a general perspective, this research project can be considered a precursor for more advanced ideas. For example, one could investigate how the here-presented fluxonic systems affect the high-harmonic generation in superconductors under structured light. One can also conceive a scenario where the coupled FM/SC bilayers are integral parts of a Josephson junction. The findings of such research studies will be reported elsewhere.

5 Supercurrent induced by chiral coupling in multiferroic/superconductor nanostructures

In this chapter, it is discussed how interfacial Rashba-SOC modifies the dynamic properties of superconducting vortices in coupled FM/SC hybrid systems. Specifically, it is considered how electric current-induced vortex motion is affected if the SC and FM are in close contact. The results presented in this chapter are selected from the original article [210], published by the author of this thesis.

From an application point of view, vortex motion is problematic since it is connected with finite electrical resistance and unwanted energy dissipation. On the other hand, type-II SCs are known to have much higher critical magnetic fields and critical current densities than type-I materials. Therefore, finding effective pinning mechanisms for fluxons is of high interest and an active field of research. A standard method for vortex pinning consists of introducing artificial pinning centers into the SC, for example, nanoparticles, antidots, columnar defects, thickness modulations, and magnetic dots [48–52]. Another interesting and effective method relies on the so-called flux pinning [211]. Here, the vortex is magnetically bound to a position where a local external field is applied. This is the case when the SC is placed on top of a strong-anisotropy FM which is divided into several domains. The corresponding magnetic stray fields have been proposed to exert exceptionally strong pinning forces on vortices [212].

In this work, another strategy is applied. The idea is to prevent fluxon penetration into the material in the first place. In SCs of non-ellipsoidal shape, it is commonly observed that an energetic barrier significantly inhibits vortex generation at the edges of the sample. This surface barrier usually depends in a complicated way on the geometry of the sample and the material composition. Its investigation is, therefore, quite challenging. Nonetheless, it is crucial to understand how vortex entry is affected by surfaces since it directly affects flux flow in the system [213–215]. Therefore, a natural idea is to use the energetic entry barrier to keep the material free of fluxons. Furthermore, combined with conventional pinning mechanisms, even better fluxon control can be achieved and the critical current of devices can be significantly enhanced [216].

In the following, it will be discussed how the fluxonic entry barrier in a microsized FM/SC bilayer is modified by interfacial Rashba-SOC. Specifically, it will be shown how the flux flow in a conventional s-wave SC is modified by direct proximity to a helical multiferroic oxide, such as TbMnO_3 [217]. In such a material, a combination of electronic correlations, magnetic exchange, and SOC can lead to the appearance of spontaneous electric polarization. Thus, the material is ferroelectric and ferromagnetic at the same time. As a consequence, the underlying magnetic order becomes susceptible to changes

in the electric polarization providing an opportunity for an all-electric control of the spin-ordering [218,219]. In helical ferroics, it has been demonstrated that the switching from positive to negative helicity can already be achieved with comparably small electric fields. On the other hand, in proximity-coupled FM/SC hybrids, interfacial SOC is directly affected by changes in the magnetic order of the FM. Combining these ideas allows the multiferroic layer to be utilized as an electrical control element for flux motion in the adjacent SC.

In the following, it will be demonstrated how changes in the spin-helicity of a multiferroic layer drive a proximity-coupled SC into subsequent states of vortex pinning and viscous flux flow. It will be shown that the key mechanism responsible for this behavior is a change in the energetic barrier for fluxon entry. This change is associated with a modified magnetic field at the sample edges, and in return, natural consequence of the interfacial Rashba SOC between the materials. Furthermore, it will be shown that the SOC-induced supercurrents lead to a substantial anisotropy in the vortex dynamics.

5.1 Methods

The geometry of the considered system is shown in Fig. 5.1. The SC is a square film

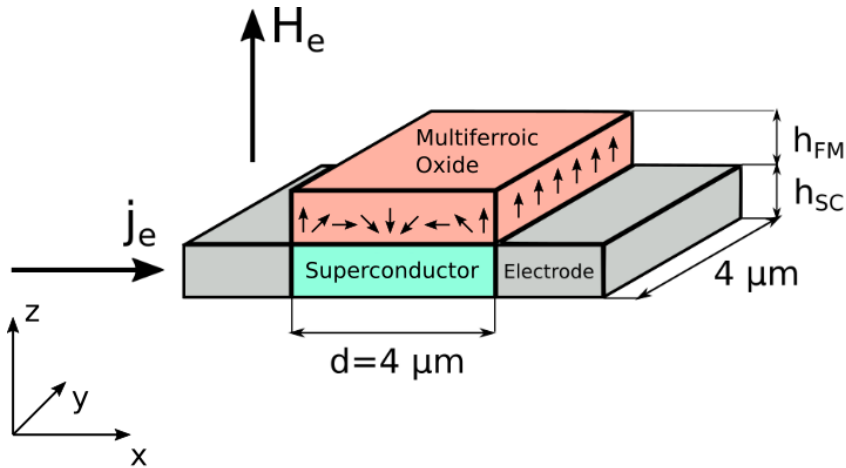


Figure 5.1: Geometry of the considered system. A superconducting square layer of length $d = 4 \mu\text{m}$ and height h_{SC} is placed underneath a multiferroic oxide of equal dimensions. The multiferroic top layer hosts a helical magnetic ordering and is proximity coupled to the SC via interfacial Rashba-SOC. Both layers are subject to an external magnetic field \mathbf{H}_e . A transport current \mathbf{j}_e is applied to the SC, driving the SC into a state of continuous flux flow.

of side length $d = 4 \mu\text{m}$ and a height h_{SC} . It is placed directly under a multiferroic film of equal side length and height h_{FM} . Both layers are in close contact and subject to an external magnetic field \mathbf{H}_e pointing into the z -direction. The ferroic layer hosts a magnetic ordering in the form of a transverse spin spiral. It will be referred to as the magnetic layer, though its mean magnetization is zero in equilibrium. Two electrodes

are attached to the sides of the bottom layer where a transport current \mathbf{j}_e is injected. Space-inversion symmetry is broken at the interface between the layers, allowing for a finite Rashba-SOC. In addition, the top layer displays an intrinsic SOC associated with its distinct ferroelectric properties. Upon close contact and in the presence of SOC, the local exchange interaction leads to a magneto-electric coupling between the magnetic texture \mathbf{m} and the superconducting phase field θ [38, 220, 221]. This interaction results in a flow of supercurrents around the interface, even without additional external magnetic fields. In the following, this magnetoelectrically generated current is investigated for its potential to control fluxon motion.

In the presence of SOC, the free energy functional of the SC (2.15) has to be modified to account for SOC-induced current flow. In the series expansion of the free energy then an additional term appears [39, 222]

$$f_{\text{SOC}} = \frac{\alpha_s}{2m_s} \cdot \left[\Psi \left(\hat{\mathbf{D}}\Psi \right)^* + \Psi^* \left(\hat{\mathbf{D}}\Psi \right) \right]. \quad (5.1)$$

Here, one has $\alpha_s = \alpha_{s,0} \mathbf{N} \times \mathbf{h}$ with the Rashba-constant $\alpha_{s,0}$ being nonzero only in the absence of inversion symmetry. The normal vector \mathbf{N} points in the direction of the broken inversion symmetry, here the z-direction. The exchange field \mathbf{h} has the same orientation as the local magnetization \mathbf{M} and penetrates the SC in a thin layer around the interface. In very thin films with $h_{\text{SC}} \ll \lambda_{\text{GL}}$ and $h_{\text{SC}} \ll \xi_{\text{GL}}$ the exchange can be averaged out over the superconducting volume [25, 223]. Also, in this limit, the order parameter no longer changes across the height of the layer. After functional minimization, the modified TDGL equations take on the form

$$0 = \frac{\hbar}{2m_s D} \left(\hbar \frac{\partial \Psi}{\partial t} + iq_s \phi \Psi \right) + \Psi \left(\beta |\Psi|^2 - |\alpha(T)| - \frac{\alpha_s^2}{2m_s} \right) + \frac{1}{2m_s} \left(\hat{\mathbf{D}} + \alpha_s \right)^2 \Psi \quad (5.2)$$

$$\frac{1}{\mu_0} \nabla \times \nabla \times \mathbf{A} = \sigma \left(\frac{\partial \mathbf{A}}{\partial t} + \nabla \phi \right) + \mathbf{j}_s \quad (5.3)$$

$$0 = \nabla \cdot \left(\sigma \left(\frac{\partial \mathbf{A}}{\partial t} + \nabla \phi \right) + \mathbf{j}_s \right). \quad (5.4)$$

$$\mathbf{j}_s = \frac{iq_s \hbar}{2m_s} (\Psi \nabla \Psi^* - \Psi^* \nabla \Psi) - \frac{q_s}{m_s} |\Psi|^2 (q_s \mathbf{A} - \alpha_s). \quad (5.5)$$

with boundary conditions

$$\left(\hat{\mathbf{D}} + \alpha_s \right) \Psi \cdot \mathbf{n} = 0, \quad \text{on } \partial\Omega_v \quad (5.6)$$

$$\Psi = 0, \quad \text{on } \partial\Omega_e \quad (5.7)$$

$$-\sigma \left(\nabla \phi + \frac{\partial \mathbf{A}}{\partial t} \right) \cdot \mathbf{n} = \mathbf{j}_e \cdot \mathbf{n}, \quad \text{on } \partial\Omega_e. \quad (5.8)$$

The parts of the boundary $\partial\Omega_v$ and $\partial\Omega_e$ indicate SC/vacuum and SC/electrode interfaces, respectively. Note, in general ϕ has contributions from the screening of the polarization

\mathbf{p} of the top layer. However, \mathbf{p} is very small in the chosen material and does not need to be considered here. The SOC-parameter $\boldsymbol{\alpha}_s$ enters the first TDGL in the form of a pair binding potential and leads to an increased critical temperature $T_c^* = T_c + \alpha_s^2/2m_s\alpha_0$. That means a space-dependent magnetic texture is now via SOC directly translated into an according modification of the order parameter amplitude. The SOC parameter also enters the equation in the form of a vector potential $\mathbf{A}_{\text{SOC}} = -\boldsymbol{\alpha}_s/q_s$ and leads to an anomalous contribution to the supercurrent density. This observation indicates that only certain magnetic textures can generate supercurrents around the interface. Specifically, if $\boldsymbol{\alpha}_s = \nabla u$, and u being a continuously differentiable field, the first TDGL equation is solved by a homogeneous order parameter distribution $\Psi = \Psi_\infty e^{-iq_s^2 u/\hbar}$. On the other hand, if $\boldsymbol{\alpha}_s = \nabla \times \mathbf{w}$, the SOC-term has the effect of a regular magnetic field applied to the sample. In the following calculations, the SOC-term is chosen to have values $|\boldsymbol{\alpha}_s| \leq 0.1\hbar/\xi_{\text{GL}}$, and order parameter variations due to the anomalous pair binding potential can be neglected. Nonetheless, this value is still large compared with commonly used values $|\boldsymbol{\alpha}_s| \leq 0.01\hbar/\xi_{\text{GL}}$ [224]. Also, for strong SOC, it has been reported that the generation of antivortices is enabled [225]. However, SOC-induced vortex nucleation was not observed here, presumably because a different material and sample geometry was used in this work. For the SC, the material parameters of Nb are chosen [204]. In addition, the electrical conductivity is set to $\sigma = 38 \times 10^6/\Omega\text{m}$. At this point, it should be mentioned that the combination of Nb and TbMnO₃ is not optimal since the wavelength of the spin spiral, typically on the order of several nanometers, is smaller than the Ginzburg-Landau coherence length. Here, using a high-T_c material with very small ξ_{GL} could be a better choice for experiments. In the here-considered case, the spin spiral is chosen to have the form of a Néel spiral with a minimum wavelength of $\Lambda = 400 \text{ nm} \approx 2.5 \xi_{\text{GL}}$, which is roughly the size of a vortex. The corresponding exchange field reads

$$\mathbf{h} = -\sin\left(\frac{2\pi mx}{d}\right)\mathbf{e}_x - \cos\left(\frac{2\pi mx}{d}\right)\mathbf{e}_z. \quad (5.9)$$

Here, m is the winding number with $m = 1$ indicating the magnetization making one complete rotation across the entire length of the sample. The absolute value of the exchange field is absorbed into the SOC parameter, and \mathbf{h} is a unit vector field. From this field, it is straightforward to calculate the SOC-parameter as

$$\boldsymbol{\alpha}_s = -\alpha_{s,0} \sin\left(\frac{2\pi mx}{d}\right)\mathbf{e}_y. \quad (5.10)$$

Following the above discussion, it can be confirmed that $\boldsymbol{\alpha}_s = \nabla \times \mathbf{w}$ and $\nabla \cdot \boldsymbol{\alpha}_s = 0$ and the anomalous supercurrent distribution is nonzero. In contrast, for a magnetic texture in the form of a Bloch spiral, the curl of $\boldsymbol{\alpha}_s$ would be zero, and the current flow would not be observable. The magnetic field corresponding to (5.10) is now

$$\mathbf{B}_{\text{SOC}} = -\nabla \times \frac{\boldsymbol{\alpha}_s}{q_s} = 2\pi m \frac{\alpha_{s,0}}{dq_s} \cos\left(\frac{2\pi mx}{d}\right)\mathbf{e}_z. \quad (5.11)$$

The SOC-induced magnetic field has a spatial dependency and modulates the external field. With increasing winding number, the amplitude of this modulation increases as

well. However, the total magnetic flux over one half-period of \mathbf{B}_{SOC} is constant, i.e.,

$$\Phi_{\text{SOC}} = \int \mathbf{B}_{\text{SOC}} \cdot \mathbf{e}_z dF = 2 \frac{\alpha_{s,0}}{q_s} d^2. \quad (5.12)$$

Before the results are discussed, several simplifying assumptions have to be made. First of all, a very thin superconducting film is considered. For such a system, the effective London penetration depth is very high, and the superconducting stray field is usually relatively weak. In this case, it is permitted to neglect the influence of the stray field on the order parameter and set $\mathbf{A}_s = 0$. Furthermore, the magnetic layer is assumed to be unaffected by the SC, external fields, and Oersted fields stemming from current flow in the bottom layer [226]. Also, the thickness of this layer is assumed to be small enough to neglect magnetic stray fields that eventually appear [223]. Finally, the Oersted fields of the circuits are also not expected to act on the SC. Another important point is that, in general, the magnetization of the top layer is not a perfect spin spiral but distorted due to external and internal fields. In the presence of broken inversion symmetry, such deviations can lead to additional Lifschitz-invariants in the free energy functional [227]. For simplification purposes, effects stemming from texture imperfections are not taken into account.

5.2 Results

5.2.1 Vortex dynamics for zero SOC

Before it is discussed how SOC affects the vortex motion, it is instructive to see the principal behavior of fluxons under transport current. Starting point is the state with a single vortex under applied magnetic field $B_e = 1.5 \text{ mT}$. Upon slowly ramping up the external current $\mathbf{j}_e = j_e \mathbf{e}_y$, the vortex is deflected into the x-direction. The resulting vortex motion is associated with a normal current flow and an increased voltage between the electrodes. The mean voltage, in this case, can be calculated as

$$\langle U \rangle_{x,y} = \frac{1}{d} \int_{\Omega_{\text{SC}}} \nabla \phi \cdot \mathbf{e}_{x,y} dF. \quad (5.13)$$

This quantity will be used in the following to characterize the dynamic state of the system. If the current is strong enough, a continuous vortex motion sets in, as shown in Fig. 5.2.

The dynamical behavior of the SC can be understood as follows. Initially, the vortex at the SC center is deflected towards the sample edge by the applied transport current. If the current is sufficiently small, the vortex finds a new equilibrium position closer to the edge at $x = 2 \mu\text{m}$. In this case, vortex expulsion from the system is prevented by an energetic surface barrier, resulting from the microscopic Bean-Livingston barrier and geometric confinement [228–230]. Flux expulsion only happens once an additional fluxon enters the sample from the left edge at $x = -2 \mu\text{m}$. The possibility of having another fluxon entering the sample has two reasons. First, the external current has a direction that enhances the supercurrent flow at the left edge of the SC and reduces it at the right edge. The increased current magnitude locally reduces the order parameter density and

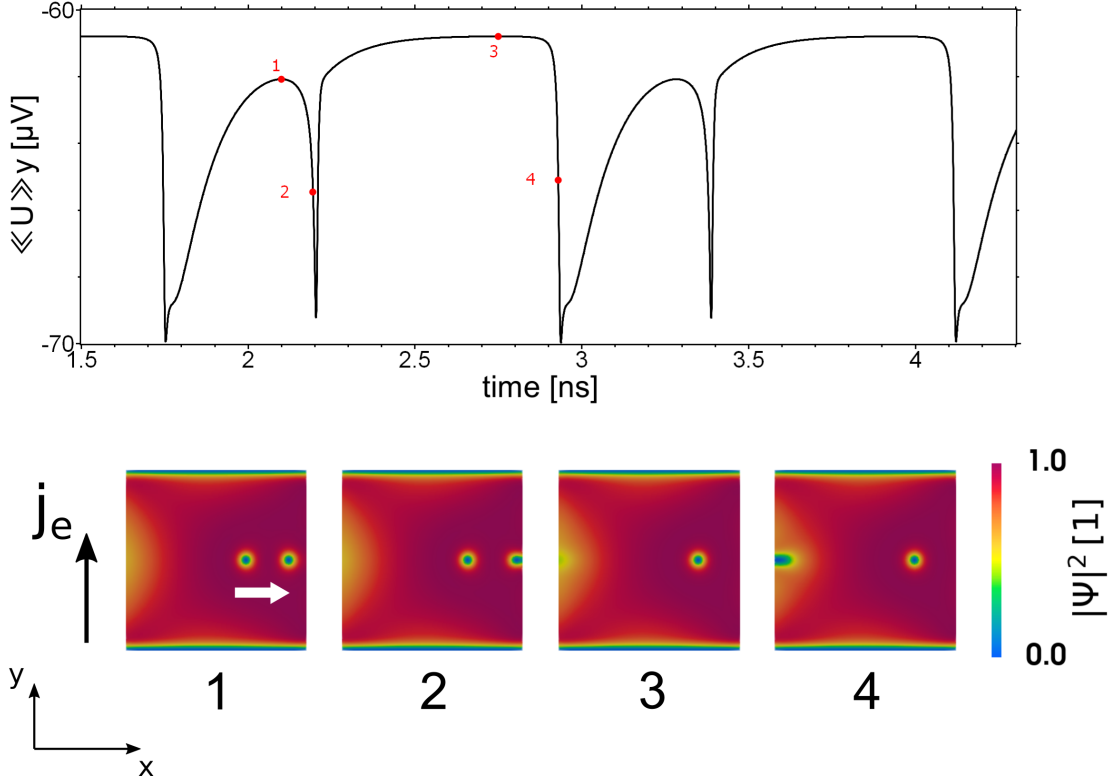


Figure 5.2: Time evolution of the superconducting state for $B_e = 1.5$ mT, $\alpha_{s,0} = 0$ and $\mathbf{j}_e = 7.07$ GA/m² \mathbf{e}_y . The black curve shows oscillations of the mean voltage due to periodic vortex motion in the SC. Lower panels: Vortex states for specific points in time. The numbering corresponds to the points indicated in the upper plot.

the edge barrier for vortex entry. Second, the initial vortex now has a greater distance towards the left edge, and its screening currents are less effective in keeping other fluxons out of the sample. Once nucleated, the second vortex travels toward the center of the sample, where it pushes against the first vortex. The combined forces of the external current and the other fluxon provoke an annihilation event at the right edge, and another metastable equilibrium is reached. The whole dynamic process repeats every $t = 1.2$ ns. In general, the edge barrier depends on the exact current distribution and, therefore, on the number and spatial distribution of fluxons. In return, The barrier determines the flux configuration of the SC. In realistic samples, edge imperfections modify the energetic barrier for vortex nucleation. However, only clean samples with perfect edges and nonzero SOC are considered in the following.

5.2.2 Vortex dynamics in the presence of SOC

In this section, it is investigated how Rashba SOC with $\alpha_{s,0} = 0.1\hbar/\xi_{\text{GL}}$ affects the previously described vortex dynamics. Starting point is the dynamic state shown in Fig. 5.2, from which the winding number of the spin spiral is slowly increased from $m = 0$ to $|m| = 10$. Experimentally such a change of the winding number can be

achieved by applying an electric field to the top layer that acts upon the ferroelectric polarization. This field is supposed to be symmetric with respect to the y-axis leaving the magnetization unchanged along that direction. This way, the spin spiral is contracted symmetrically around the central axis. The ferroic top layer acts on the SC via the space-dependent SOC field defined in equation (5.11) and modifies the current distribution around the interface. In the following calculations, the spin spiral is always assumed to be a static structure, and the transient spin dynamics are not considered. Apart from the symmetric contraction around the central axis, two other scenarios are considered as well: one where the magnetization is always fixed at the left edge of the SC and one where it is fixed at the right edge. The corresponding SOC-parameters are denoted as α_s^l (left edge fixed) and α_s^r (right edge fixed) respectively

$$\alpha_s^{l,r} = -k_{r,l}\alpha_{s,0} \sin\left(n\pi\left[2\frac{x}{d} + k_{r,l}\right]\right) \mathbf{e}_y. \quad (5.14)$$

Here $k_l = 1$ and $k_r = -1$. The corresponding magnetic field is

$$\mathbf{B}_{\text{SOC}}^{l,r} = k_{r,l}2\pi n \frac{\alpha_{s,0}}{dq_s} \cos\left(n\pi\left[2\frac{x}{d} + k_{r,l}\right]\right) \mathbf{e}_z. \quad (5.15)$$

From now on, the SOC parameter corresponding to a symmetric contraction around the central axis will be referred to as α_s^s . The mean voltage for increasing winding number $|m|$ and different magnetic textures $\alpha_s^{l,s,r}$ is shown in Fig. 5.3. First, the case of the symmetric SOC-parameter α_s^s is considered. For increasing winding number, the mean voltage displays several plateaus followed by sharp drops towards local minima. Analyzing the simulation data reveals that the voltage oscillations result from vortices experiencing different dynamic phases. Each plateau corresponds to a superconducting state where vortex motion is inhibited, and the current flow is dissipationless. The voltage minima, on the other hand, result from enhanced vortex mobility, and the corresponding states are highly dynamic. It is also observed that the onset of vortex motion upon increasing m is always triggered by a vortex entering the sample from the left edge. That indicates that the energy barrier for fluxon entry plays an important role in the problem. The barrier for vortex exit is observed to be of lesser relevance. That also becomes apparent if the magnetic spiral is contracted in a way that the magnetization is fixed either on the left or right edge of the magnetic layer.

First the SOC-parameter α_s^l is considered for slowly increasing $|m|$ (see Fig. 5.2(b)). In this case, the SOC-field B_{SOC} is constructed such that for $m > 0$, the field on the left edge of the sample points into the positive z-direction, whereas for $m < 0$, the field is negative.

For positive field values ($m > 0$), Vortex motion is permanently inhibited, and the mean voltage is only changing slightly. These small voltage changes are caused by fluxon rearrangements due to the changing spatial distribution of the magnetic field. Such vortex displacements are also the reason for voltage drops across the plateaus in Fig. 5.2(a).

If the SOC field is permanently negative at the left edge ($m < 0$), the frequency of the voltage oscillations roughly doubles. Also, the voltage plateaus only gradually appear in the form of local spikes. The negative SOC field at the left sample edge makes vortex entry permanently easier. The higher amount of fluxons, as well as their position and

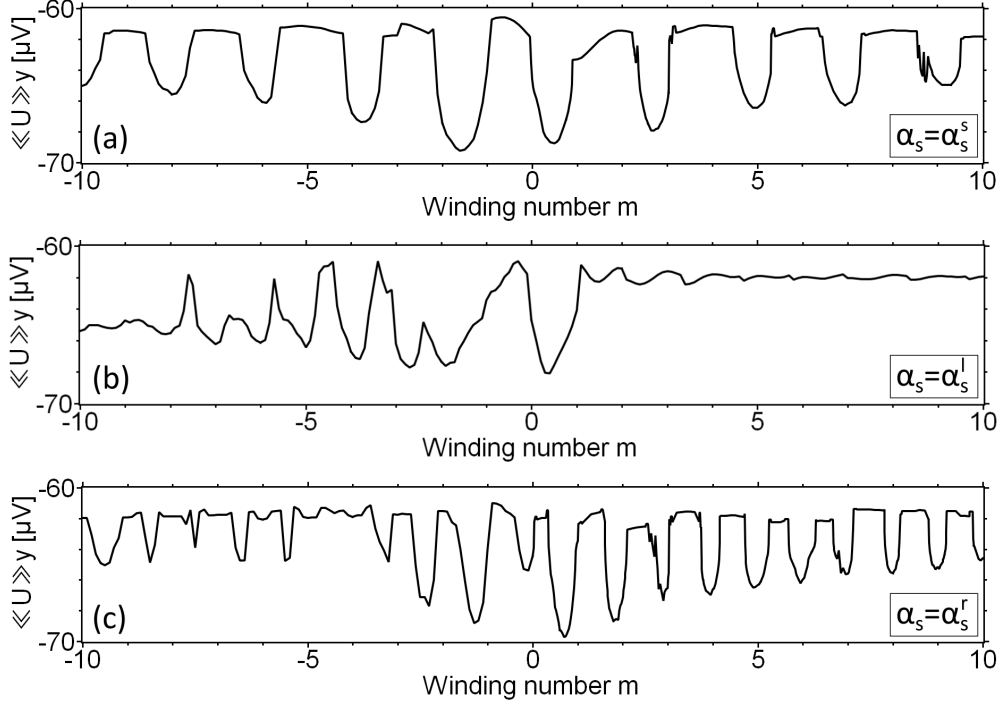


Figure 5.3: Mean voltage versus winding number for $B_e = 1.5$ mT, $\alpha_{s,0} = 0.1\hbar/\xi_{GL}$, $j_e = 7.07$ GA/m² and three distinct magnetic textures. (a): the magnetic spiral is symmetrically contracted around the y-axis with SOC-parameter $\alpha_s = \alpha_s^s$. (b): the magnetization is fixed at $x = -d/2$ with $\alpha_s = \alpha_s^l$. (c): the magnetization is fixed at $x = +d/2$ with $\alpha_s = \alpha_s^r$.

interaction, now lead to a more complex behavior of the energy barrier. In this case, extended regions of vortex pinning are no more to be found.

These observations indicate that the sign of \mathbf{B}_{SOC} at the layer edges is responsible for the different dynamic fluxon phases. Therefore, a change of the system's dynamic state should be possible by applying an appropriate phase shift to the spin spiral. To support these assumptions, the symmetric SOC parameter is now modified to

$$\alpha_s^s = -\alpha_{s,0} \sin\left(2\pi m \frac{x}{d} + \varphi\right) \mathbf{e}_y, \quad (5.16)$$

where $\varphi \in [0, 2\pi]$ corresponds to the phase of the spin spiral. Then φ is varied from 0 to 2π for a number of specific m -values. The results are shown in Fig. 5.4. Here the values of m are chosen such that for $\varphi = 0$, the vortices are highly mobile, and the system is in the resistive state (see Fig. 5.2(a)). Upon increasing the phase factor from 0 to π , vortex pinning can be restored, and the system becomes dissipationless, as indicated by the voltage plateau at $\varphi = \pi$. Such a phase shift corresponds to a sign inversion of \mathbf{B}_{SOC} from negative to positive values at $x = -2$ μm . For $\varphi = \pi$, the energy barrier for vortex entry is enhanced, and vortices become immobile. The observations made for different phase factors match those made for the SOC-parameter α_s^l . The sign inversion of \mathbf{B}_{SOC} for negative values of m is also reflected in the symmetry of the curve in Fig. 5.2(a), i.e.,

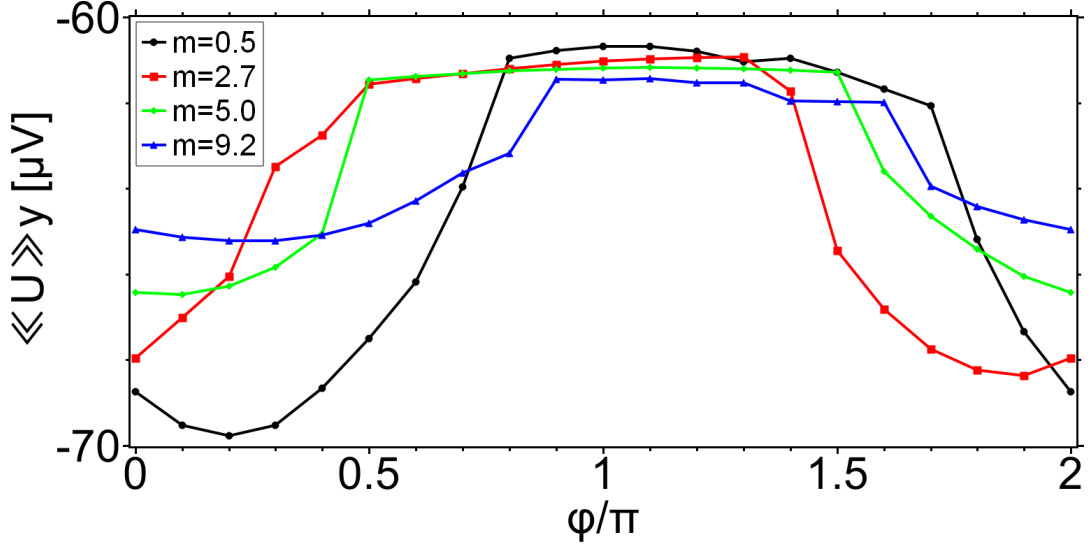


Figure 5.4: Mean voltage versus phase shift φ for a symmetric SOC-parameter α_s^s and selected winding numbers. The values of m are chosen such that the system is in the resistive state for $\varphi = 0$. Upon a phase change of $\varphi = \pi$, the system transits into the dissipationless state.

the curve is antisymmetric with respect to $m = 0$.

The spin spiral is now fixed at the right edge of the layer with a SOC-parameter $\alpha_s = \alpha_s^r$. The corresponding SOC-field is constructed such that for positive m , \mathbf{B}_{SOC} is negative at the right edge of the sample, and for negative m , the field is positive. If a symmetric contraction with $\alpha_s = \alpha_s^s$ is considered, a sign-change of B_{SOC} at the sample edges requires a change in the winding number of $\Delta m = 1$. On the other hand, if the magnetization is fixed at one of the edges, the field value of B_{SOC} at the opposite side flips from positive to negative already for $\Delta m = 0.5$. In the here-considered case, this means that the voltage oscillations double their frequency for $\alpha_s = \alpha_s^r$. That is indeed the case, as can be seen in Fig. 5.2(c). Interestingly the curve, in this case, is not as symmetric as the one for $\alpha_s = \alpha_s^s$. That indicates that the vortex expulsion barrier, despite its seemingly lesser relevance, plays a role in the given problem.

From now on, the external current that transits the system into the flux flow state is denoted as depinning current j_d . The dependency of this current on the winding number for $\alpha_s = \alpha_s^s$, $B_e = 1.5 \text{ mT}$ and $\alpha_{s,0} = 0.1\hbar/\xi_{\text{GL}}$ is shown in Fig. 5.5. Here, the vortices are pinned for $j_e \leq j_d$, whereas for $j_e > j_d$, a continuous vortex motion sets in. The shape of the curve matches the one in 5.2 (a) very well, i.e., depinning current maxima and voltage plateaus appear for the same values of m . Interestingly two regimes for the vortex dynamics can be distinguished. For small values of m , vortex mobility is enhanced for half-integer values of the winding number whereas for large values of m the corresponding voltage minima appear at full integer values. Also, the vortex number changes more rapidly for small winding numbers. For high values of m , mostly 1-vortex and two-vortex states are found to be stable. The curve also displays several sharp kinks. During the simulations, it was found that j_d suddenly changes when the

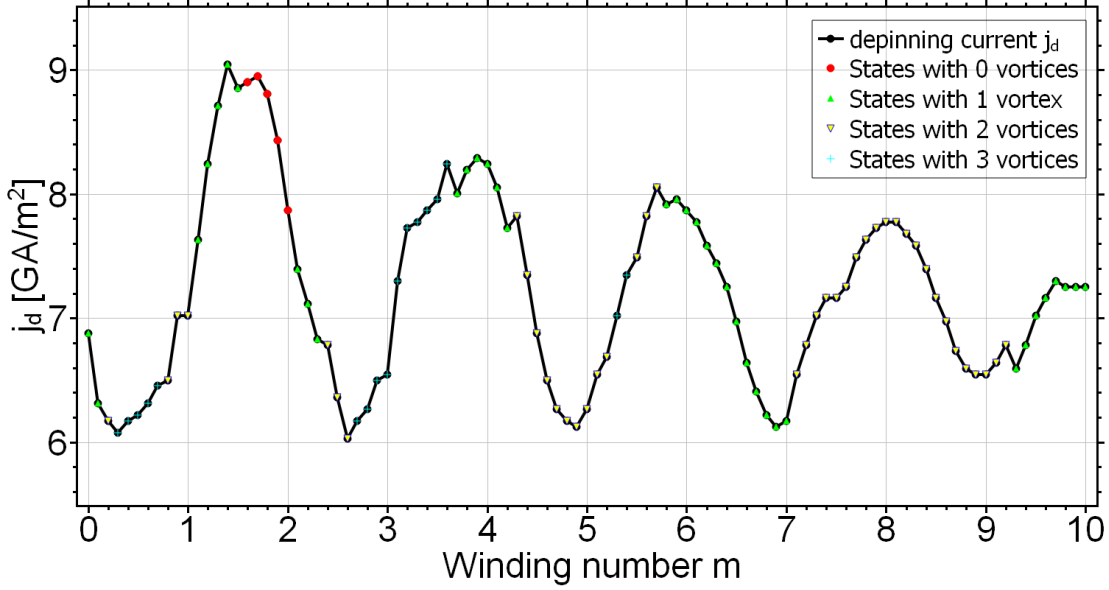


Figure 5.5: Depinning current versus winding number for $\alpha_s = \alpha_s^s$, $B_e = 1.5$ mT and $\alpha_{s,0} = 0.1\hbar/\xi_{GL}$. The black curve approximates the current values for which vortex motion is barely prevented. The points on the curve show the number of vortices simultaneously existing in the SC.

total fluxon number in the sample changes as well. Also, vortex rearrangements were observed to have the same effect. SOC-induced vortex pinning becomes strongest for $m \approx 1.5$, and the depinning current, in this case, has an approximately 28% higher value than in the SOC-free case.

A better understanding of the two dynamic regimes of small and large winding numbers can be obtained by inspecting the supercurrent density in the absence of vortices. Additionally, $B_e = 0$, $j_e = 0$ and $|\alpha_s^s| = 0.1\hbar/\xi_{GL}$ are set, which means the supercurrent is purely defined by its anomalous part. For small current densities, the order parameter is now approximately homogeneous, and the supercurrent can be written as $\mathbf{j}_s = q_s \alpha_s^s / m_s$. In Fig. 5.6, the y-component of this current across the x-axis is plotted for selected values of m . For comparison, the supercurrent for $\alpha_{s,0} = 0$ and $B_e = 1.5$ mT is also displayed here.

Note, despite the increasing winding number, the amplitude of \mathbf{j}_s is for all curves the same. That is because the magnetic flux $\Phi_{SOC} = 2\alpha_{s,0}d^2/q_s$ threading the SC/FM interface over one half-period of α_s^s is independent of m .

For small winding numbers, the currents spread broadly across the entire SC. In this regime, increased vortex mobility is observed for $m = 0.5$ and $m = 2.5$. Here from (5.10), it follows that the anomalous supercurrent $j_{s,y} \sim \alpha_{s,y}^s$ along the edges has the same flow direction as the conventional Meißner current induced by external fields (see Fig. 5.6). As a consequence, the total current is increased, leading to stronger suppression of the order parameter along the edges. As a result, the corresponding energy barriers are reduced as well, enabling an easier fluxon transit through the material [231].

If the current flow is reversed by a sign change of \mathbf{B}_{SOC} , the anomalous supercurrents

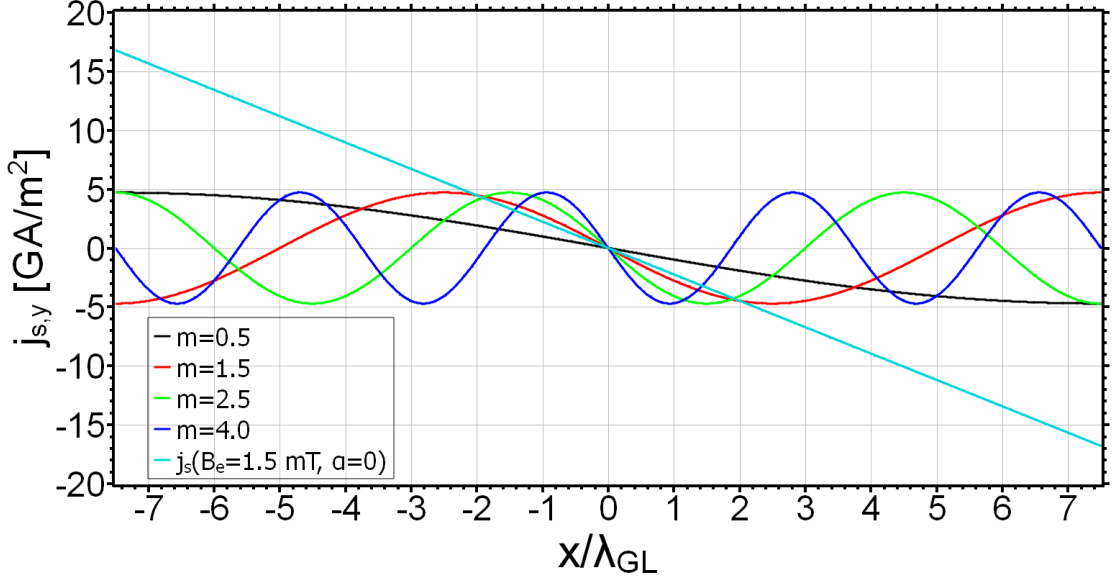


Figure 5.6: y-component of the supercurrent \mathbf{j}_s for $|\boldsymbol{\alpha}_s^s| = 0.1\hbar/\xi_{GL}$, $B_e = 0$ and in the absence of vortices and external currents. For the selected winding numbers m , the current becomes extremal around the edges. Cyan curve: reference state for $B_e = 1.5$ mT and zero SOC.

counteract the conventional Meißner currents along the edges. That is, for example, the case for $m = 1.5$. Now the edge barrier is higher than before, and vortex flow is inhibited. This effect resembles the restoration of the edge barrier by vortex entry into the SC [232].

An externally imposed current flow, on the other hand, reduces the entry barrier and enhances the exit barrier since its flow direction is strictly along the positive y-direction. In this way, an imbalance in the entry and exit conditions for fluxons is created, leading to the dynamic phases discussed above.

For large winding numbers, the extrema of the depinning current are shifted to full integer values of m where the SOC-induced supercurrent along the edges becomes zero. In this regime, it is evident that not the actual value of \mathbf{j}_s but rather the total current distribution along the edges determines the conditions for the flux flow. For example, vortex pinning is observed for $m = 4$, i.e., when the first extremum of \mathbf{j}_s is negative near the left edge. In contrast, vortex flow is re-enabled \mathbf{j}_s has a local maximum near the left edge. The total current flow around the edges is also in the low- m regime, the decisive factor for the vortex dynamics. Here the broad current distribution allows more vortices at the same time to exist in the SC, leading to an enhanced voltage signal (see Fig. 5.2 (a)).

Finally, also vortex motion due to an external current along the x-direction is considered. Such a current is directed transversely to the wave vector \mathbf{k} of the spin spiral $\boldsymbol{\alpha}_s^s$. In this case, the fluxons are forced to move along the y-axis and produce a voltage signal that depends on the winding number m of the spin spiral (see Fig. 5.7). For comparison, the voltage signal for $\mathbf{j}_e = j_e \mathbf{e}_y$ is also plotted for the same values of m .

In contrast to the case where $\mathbf{j}_e \parallel \mathbf{k}$, a transverse current flow leads to a substan-

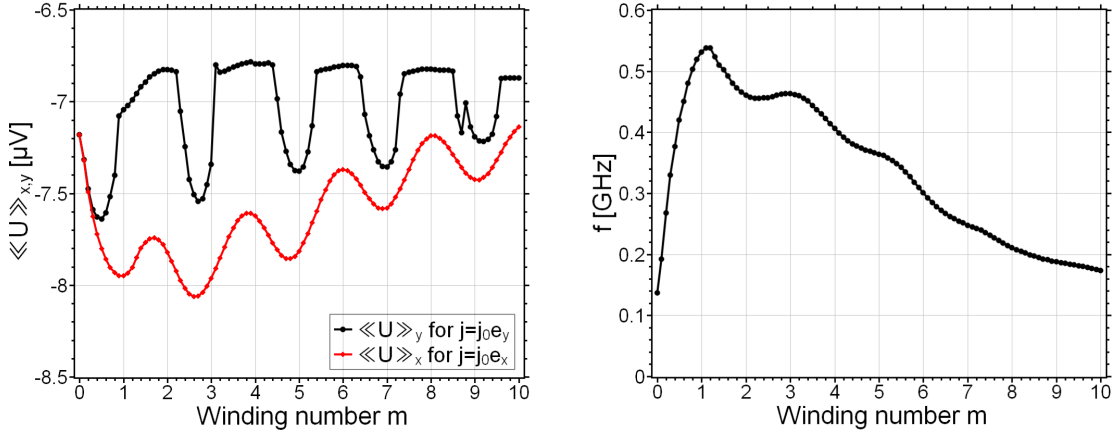


Figure 5.7: Left: Mean voltage versus winding number for $\alpha_s = \alpha_s^s$ and different directions of the injected transport current. Here \mathbf{k} is the wave vector of the spin spiral. For transport-currents parallel to \mathbf{k} (upper curve), vortices experience consecutive phases of pinning and enhanced mobility. For transport currents transverse to \mathbf{k} (lower curve), vortex-pinning is not observed. Right: Frequency of the voltage oscillations for $\mathbf{j}_e = j_e \mathbf{e}_x$ depending on the average vortex number and the time a vortex resides in the sample.

tially enhanced voltage signal. Also, instead of consecutive phases of vortex pinning and flux flow, this time, the voltage signal oscillates with increasing winding number. That indicates the complete absence of static vortex phases. Instead, the SC is in a state of constant flux flow where the average number of fluxons varies continuously with m . The maxima and minima of the average vortex number coincide with the corresponding extrema in the voltage curve.

An interesting observation can be made by comparing the voltage maxima and minima of the two curves in Fig. 5.7. Apparently, the winding numbers that prevented flux motion in the case $\mathbf{j}_e \parallel \mathbf{k}$ also reduce the voltage signal when $\mathbf{j}_e \perp \mathbf{k}$. So far, no suitable explanation for this phenomenon could be found. That is mainly because the current distribution along the boundaries is more complicated for transverse current flow.

In any case, vortex entry is always observed at parts of the boundary where \mathbf{B}_{SOC} points into the positive z -direction. There it leads to an enhanced total field. For $\alpha_s = \alpha_s^s$ this is, for example, the case at $(x = 0, y = \pm 2 \mu\text{m})$. For a symmetric SOC parameter, the SOC-enhanced magnetic field at the center of the sample builds a channel that hinders transverse vortex motion. Only for small winding numbers, the slowly varying SOC field allows for lateral movement. On the other hand, for higher values of m , vortex motion becomes highly directional along the y -direction.

The frequency f of the time-dependent voltage oscillations for $\mathbf{j}_e \perp \mathbf{k}$ is shown in Fig. 5.7 (b). This frequency depends on the moving speed of individual fluxons, their average number, and the time that an individual vortex resides in the SC before it gets expelled. One can see that f has values in the GHz-regime with a local maximum for $m = 1$. For larger winding numbers, the frequency approaches the initial value for $B_{\text{SOC}} = 0$ since the SOC field becomes averaged out on a spatial scale. That is also visible in Fig. 5.5 where the maximum depinning current is reduced for large winding numbers. If

the winding number becomes negative (not shown here), the mechanism that increases vortex mobility is reversed, and vortex pinning is again observable.

In this chapter, it was investigated how the vortex dynamics of a superconducting thin film are affected by interfacial Rashba-SOC. The SC was proximity-coupled to a magnetically ordered top layer with strong intrinsic SOC. The magnetic ordering was assumed to have the form of a Néel-spiral with a freely adjustable winding number m . A subsequent increase of m was found to force the vortices in the system through alternating phases of pinning and enhanced mobility. Thereby, a SOC-induced modification of the energetic edge barrier for vortex nucleation was identified as the main reason for the modified vortex dynamics. Furthermore, the coupling between the superconducting phase field θ and the magnetic texture was also observed to modify the average vortex number and the critical depinning current of the sample. In particular, SOC-induced vortex pinning is most effective for low winding numbers. In contrast, for high winding numbers, the coupling to the multiferroic layer became less relevant since SOC-related effects are averaged out. It was also investigated how phase changes of the spin spiral affect the vortex mobility. Thereby it was confirmed that a modification of the edge barrier for vortex penetration is susceptible to such a phase change leading to the modified vortex dynamics described earlier. Finally, if the external electric current is directed transversely to the spin spiral vortex motion becomes channeled. In this case, phases of vortex pinning can be avoided altogether for positive winding numbers of the spin spiral. The results of this section potentially allow for superconducting devices where the vortex dynamics are electrically coupled to the magnetization of a multiferroic top layer. In this way, an all-electric control of the dynamic state of the system could be achieved with potential applications in fluxonic memory devices. The results presented in this section are also expected to remain valid if the interfacial SOC field is replaced with the stray field of an appropriately textured FM (e.g., a FM with a magnetization in the form of a chiral domain wall).

6 Magnon-fluxon interaction in coupled superconductor/ferromagnet hybrid systems

In this chapter, it is investigated how magnon propagation in a micro-sized waveguide is affected by the vortex field of a nearby SC. First, the equilibrium state of the SC, and the associated stray field, are obtained by solving the TDGL equations of superconductivity. Then, a replacement system consisting of ferromagnetic nanocubes is constructed, mimicking the vortex field and serving as input for the Landau-Lifschitz equation. The material parameters are chosen to match the experiment of Dobrovolskiy et al. [85], allowing for a quantitative comparison of the here-presented results to realistic systems. It was found, that the presence of the vortex lattice leads to the formation of a Bloch-like band structure in the magnon spectrum. It was also observed that the presence of the nanomagnets leads to a downward shift of the lowest order allowed bands due to the confinement of the low-frequency magnonic modes. The role of structural disorder in the vortex lattice was also investigated. It was observed that already a slight distortion of the lattice substantially inhibits the propagation of the lowest-frequency modes, whereas the high-frequency modes are only slightly disturbed. Finally, it is also discussed how the magnonic bands change with varying waveguide thickness.

6.1 Methods

The here-presented system consists of a ferromagnetic magnonic waveguide and a type-II SC on top. Both layers are separated by an insulating layer of height $h = 5$ nm. In this way, the interaction between the two layers is purely electromagnetic, and hybridization effects do not have to be considered [233]. Spin wave dynamics are then only driven by the stray fields of the system constituents and intrinsic damping of the FM layer. A schematic of the structure under investigation is shown in Fig. 6.1 (a). For the ferromagnetic strip, the material constants of a Py layer are chosen, i.e., a saturation magnetization $M_s = 676$ kA/m, an exchange stiffness $A = 16$ pJ/m, and zero magnetocrystalline anisotropy. In this work, the effects of damping are not taken into account for reasons explained later. The SC is made from Nb with a magnetic penetration depth of $\lambda(8\text{ K}) = 150$ nm [85]. The GL-parameter is estimated as $\kappa = 1$, which is a typical value for Nb in the clean limit [234].

The interaction of the magnonic excitations in the waveguide with the superconducting vortices is simulated in two steps. First, the TDGL-equations (3.1) - (3.4) are solved under $\mathbf{B}_e = B_e \mathbf{e}_z$ in order to get the field distribution of a static vortex lattice. Then, the static vortex field \mathbf{B}_v is used as input for the LLG equation. In this way, the magnetization dynamics of the FM can be calculated independently from the SC dynamics.

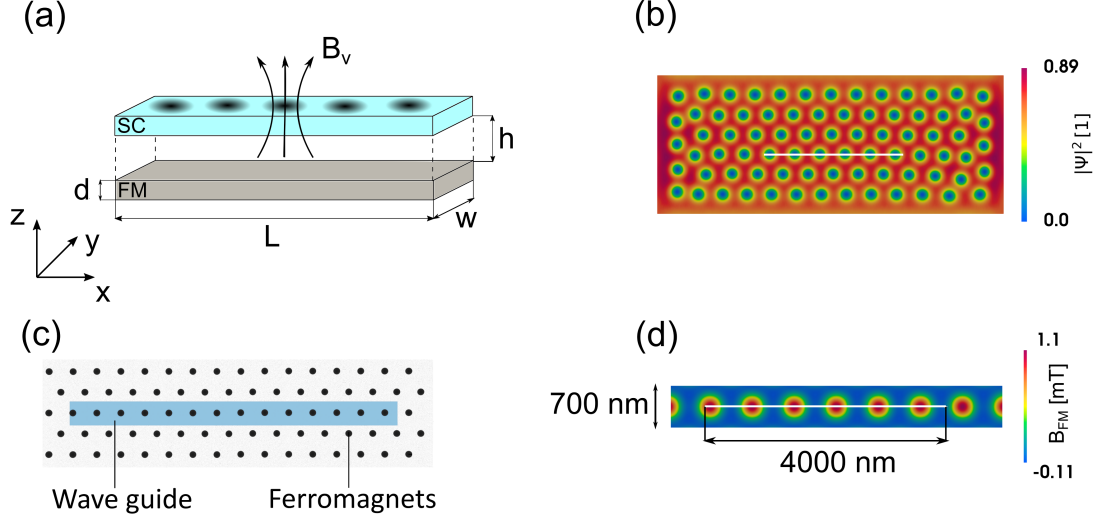


Figure 6.1: (a): Schematic of the system under investigation. The SC is a host for vortices that modulate the field distribution in the waveguide below. (b): Amplitude of the superconducting order parameter for an external field of $H_z = 5$ mT. The blue regions are normal conducting and indicate the positions of vortices. (c): Replacement system where nanomagnets modulate the field of the waveguide instead of vortices. The black dots indicate the lateral positions of the nanomagnets. (d): Field distribution B_z in the wave guide, modulated by nanomagnets with magnetization $M_{s1} = M_{s0} = 12.6$ kA/m. The lines in (c) and (d) indicate the regions over which line plots were taken.

Technically, the complete set of TDGL equations and the LLG equation have to be solved selfconsistently to capture all aspects of coupled FM/SC dynamics. However, this task is computationally very demanding, so the dynamics of the SC and FM are decoupled. That can be done by assuming that the vortex lattice is static and non-affected by the stray field of the underlying FM layer. Still, in a realistic scenario, the magnonic stray fields can very well act back on the vortex lattice [235]. Also, to trigger magnonic excitations in the ferromagnetic waveguide, it is common practice to use the time-varying Oersted field of a microwave antenna. Its effect on the static vortex lattice is also not considered in this work. For a detailed discussion of this problem, see Appendix A of the original paper [236].

In this research, it is attempted to keep the model close to the one used in [85], i.e., the SC is a clean thin film of length $L = 10$ μm , width $w = 4$ μm and thickness $d = 80$ nm. The entire bilayer-structure is subject to an external magnetic field $\mathbf{B}_e = B_\perp \mathbf{e}_z + B_\parallel \mathbf{e}_x$. Here, the in-plane component B_\parallel has the purpose of setting the magnonic waveguide into BVMSW configuration, whereas B_\perp triggers vortex nucleation in the SC. Since the superconducting layer is a thin film of thickness $d < \xi_{\text{GL}}$ the in-plane field is not able to generate vortices for the given geometry [237], and it is also not able to change the equilibrium state of the SC. For this reason, $B_\parallel = 0$ is set in the first TDGL equation. The external field acting on the SC is then $\mathbf{B}_e = \nabla \times \mathbf{A}_e = B_e \mathbf{e}_z$ with $B_e = 5$ mT. Operating in the thin film limit is equivalent to setting $\kappa \gg 1$ and allows to neglect the back-action of the SC stray field. In that case, the electromagnetic behavior of the SC

is dominated by the external magnetic field, and it is allowed to set $\mathbf{A}_s = 0$ in the first TDGL equation [238]. The solution of (3.1) then yields the equilibrium order parameter Ψ and the corresponding supercurrent distribution \mathbf{j}_s . The latter can be used as input for the second TDGL equation (3.2), or the Biot Savart law (2.29), providing the stray field \mathbf{B}_v of the vortex lattice. The solution of the first TDGL equation is performed under the gauge $\phi = 0$ and by setting $\mathbf{A}_e = -B_e y \mathbf{e}_x$.

The equilibrium state of the SC is shown in Fig. 6.1 (b). Since the SC is simulated without structural defects, the vortices tend to form a hexagonal lattice [5]. Each blue dot corresponds to a vortex with a normal conducting core surrounded by a whirl of supercurrents. For the system under investigation, the fields of these currents are not strong enough to effectively alter the state of the SC. However, they still modulate the field in the magnonic waveguide and change the magnon dynamics. Since it is inconvenient to import the numerically calculated vortex field \mathbf{B}_v into micromagnetic software like MuMax3 [200], the vortex lattice is replaced with a lattice of nanomagnets that approximately produce the same stray field. The field of a magnetic cuboid can be calculated analytically, and its strength and spatial distribution can be easily adapted to \mathbf{B}_v [87]. The nanomagnets are chosen to have dimensions $\Delta x = \Delta y = 250$ nm and $\Delta z = 360$ nm, and they are placed under the waveguide. An air gap of $\Delta h = 175$ nm separates the magnetic lattice from the waveguide above. Like the vortices, the magnet-lattice has hexagonal symmetry with a lattice constant of $a_{\text{VL}} = 700$ nm (see Fig. 6.1 (c)). Each nanomagnet has a magnetization $\mathbf{M} = M_{s1} \mathbf{e}_z$ where M_{s1} is chosen as a free parameter. For $M_{s1} = 12.6$ kA/m, the field distribution in a magnonic strip of width $w = 700$ nm is shown in Fig. 6.1 (d). Like the vortex field, the nanomagnets produce a field with local maxima directly above each magnet. The fields are compared via line plots along the x-direction in the waveguide (see Fig. 6.2). The true field of the vortices (TDGL-model) was calculated from (2.30) under the assumption of a supercurrent density that is independent of the z-direction. With the chosen geometry of the nanomagnet lattice,

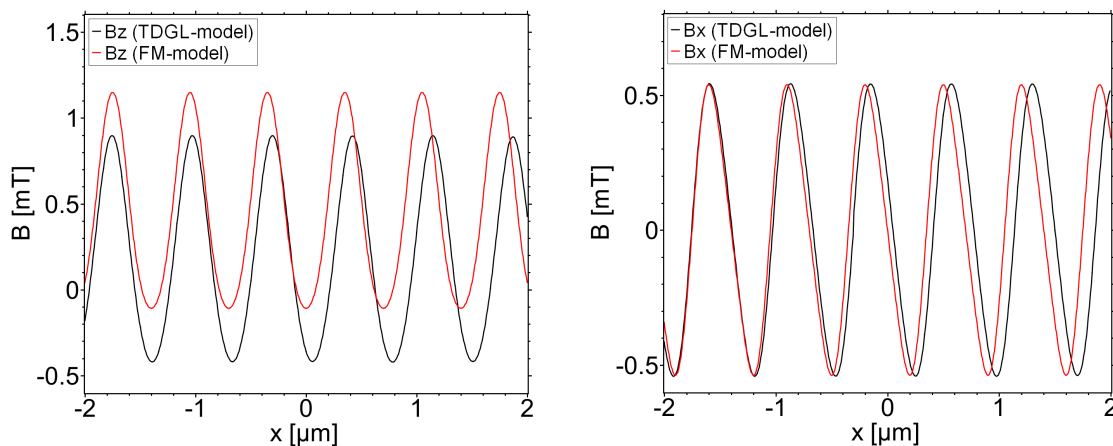


Figure 6.2: Comparison of the vortex field (TDGL-model) and the field of the nanomagnets (FM-model) for $M_{s1} = M_{s0} = 12.6$ kA/m along the lines indicated in Fig. 6.1 (b),(d).

and by setting $M_{s1} = 12.6$ kA/m, the in-plane components of the superconducting stray

field can be well approximated. In the following, this magnetization value is denoted as M_{s0} , i.e., for $M_{s1} = M_{s0}$, the replacement system of nanocubes produces a realistic vortex field. The matching for the z-component is of poorer quality. However, numeric experiments have shown that the magnonic dispersion is virtually independent of $B_{v,z}$. Therefore, even a bad approximation of this field component does not notably change the magnetization dynamics. In the original experiment, the lattice constant was found to be $a_{\text{VL}}(B_{\perp} = 5 \text{ mT}) = 691 \text{ nm}$ [85], whereas the here presented TDGL-simulations yielded $a_{\text{VL}}(B_{\perp} = 5 \text{ mT}) = 720 \text{ nm}$. As a compromise between these two values, the nanomagnet-lattice is chosen to have a lattice constant of $a_{\text{VL}} = 700 \text{ nm}$ leading to a slight mismatch between the fields shown in Fig. 6.2 (a).

Magnon dynamics along the waveguide are now simulated by solving the Landau-Lifshitz equation (2.56) with the micromagnetic simulation program MuMax3 [200]. For the waveguide, a Py stripe of variable width w , but fixed thickness $d = 1 \text{ nm}$ and length $L = 28 \mu\text{m}$ is chosen. The material parameters are as indicated above, and the cell size of the finite-difference mesh is chosen to be $5 \times 5 \times 1 \text{ nm}^3$. For spin-wave excitation, a sinc-field $\mathbf{H}_a = H_0 \sin(2\pi f_0 t)/(2\pi f_0 t) \mathbf{e}_y$ is applied to a 5 nm long stripe at the center of the waveguide and across its width. The frequency of this field is set to $f_0 = 20 \text{ GHz}$ and its amplitude to $H_0 = 15 \text{ mT}$, which is small enough to keep the magnetization dynamics in the linear regime. As already mentioned, the waveguide is placed in a magnetic bias field $H_{\parallel} = 60 \text{ mT}$, bringing the system into BVMSW configuration. The out-of-plane field $H_{\perp} = 5 \text{ mT}$ was also applied but was not observed to have a noticeable effect on the results. By applying a 2D FFT to the dynamic magnetization fluctuations $\delta m_z(x, t)$, it is possible to calculate the spin wave spectra [202]. However, it can be expected that band gaps in the magnonic dispersion are on the order of MHz since the vortex field is comparably weak. That means getting spectra of acceptable resolution requires long simulation times. That means magnetic damping has to be neglected. Otherwise, the system returns to equilibrium too quickly, leading to dispersion plots of insufficient quality. In the here presented calculations, it was found that for all tested values of Γ , the spectrum does not qualitatively change. For this reason, magnetic damping was neglected completely by setting $\Gamma = 0$.

6.2 Results and discussion

In the following calculations, the magnetization is allowed to have values up to $M_{s1} = 25M_{s0} = 315 \text{ kA/m}$. Operating with an artificially strong field allows to get a better insight into the characteristics of the magnonic dispersion. The corresponding band diagrams for $M_{s1} = 0$ and $M_{s1} = 25M_{s0}$ are shown in Fig. 6.3. For $M_{s1} = 0$, the stray field of the vortex lattice is zero, and the magnonic dispersion shows BVMSW behavior. Here, two modes are triggered by the external excitation signal; a first-order mode of high intensity and a higher-order mode of low intensity [187, 239–241]. In a typical BVMSW-spectrum, the k-space region around $k = 0$ is dominated by long-range dipolar interactions leading to a negative group velocity v_g of magnonic excitation [181]. However, the here-considered waveguide is comparably thin, and the magnonic modes are mainly driven by short-range exchange interactions. Therefore, the region with $v_g < 0$ is very narrow and not visible in the plots of Fig. 6.3. Nonetheless, dipolar interactions are

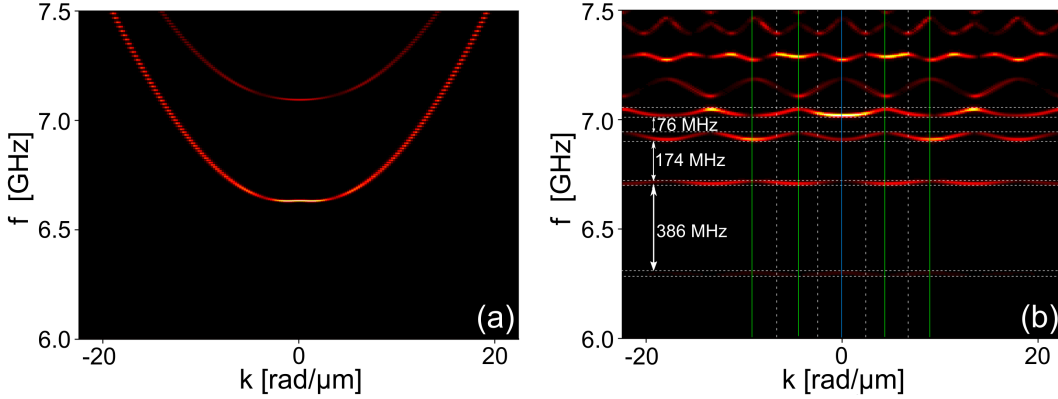


Figure 6.3: Magnonic dispersion modulated by the stray field of a superconducting vortex lattice. Left: band diagram in the absence of vortices ($M_{s1} = 0$). Right: band diagram for an artificial vortex lattice. The stray field of the vortices is replaced by the magnetic field of a lattice of nanomagnets with magnetizations $M_{s1} = 25M_{s0} = 315 \text{ kA/m}$.

still relevant and lead to an effective magnetic pinning of the dynamic magnetization at the lateral edges of the waveguide. This so-called dipolar pinning is connected with an upward shift of the entire spectrum giving rise to an intrinsic gap $f < 6.62 \text{ GHz}$ where spin wave propagation is prohibited [242, 243]. If now the vortex field is switched on by setting $M_{s1} = 25M_{s0}$ additional band gaps appear at wave vectors $k = n\pi/a_{VL}$, $n \in \mathbb{Z}$ (see Fig. 6.3 (b)). The opening of these gaps at the edges of the Brillouin zones (BZs) (thick green lines) is a consequence of the periodically modulated field inside the waveguide and reflects the translational symmetry of the vortex field in the x-direction. The formation of standing wave patterns in periodic systems due to interference of incoming and partially reflected waves is a phenomenon that appears not only in magnonic systems [187, 241] but is also well known in photonics [190] and electronic systems. In Fig. 6.3 (b), it can be observed that higher-order bands have gaps that open inside the BZs (vertical dashed lines). These gaps are a natural consequence of the interaction between first-order modes and higher-order width-modes, leading to more complicated standing wave patterns in the waveguide. This behavior was already observed in width-modulated magnonic crystals where the higher order modes are excited by magnonic scattering at edge steps in the waveguide [244, 245]. Another important observation is the appearance of a magnonic band at $f = 6.3 \text{ GHz}$. In the absence of vortices, magnon propagation at such a frequency is not allowed due to the intrinsic gap $f < 6.62 \text{ GHz}$.

In order to get a better insight into this problem, micromagnetic simulations were performed for a gradually increasing magnetization M_{s1} of the artificial vortex field (see Fig. 6.4). In addition, effects resulting from varying the distance h between the waveguide and vortex lattice were investigated as well. In (a), one can see that several band gaps open (white color) with increasing strength of the vortex field. In zero field, all frequencies with $f > 6.62 \text{ GHz}$ are allowed to propagate (grey color). The width of the lowest-order band is very narrow, and the band quickly flattens out for an increasing magnitude of the vortex field. Another important observation is a gradual downward

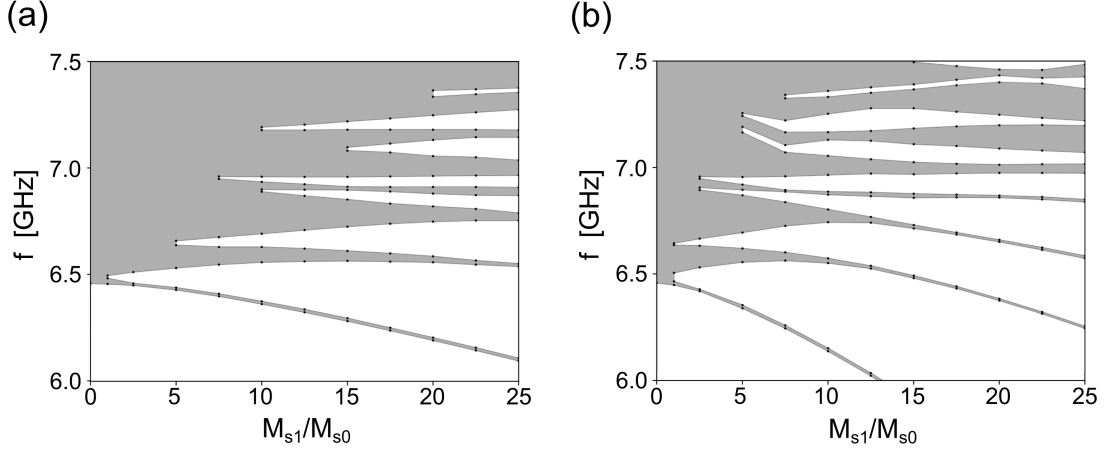


Figure 6.4: Frequency versus magnetization M_{s1} for a wave guide of width $w = 700$ nm. White color corresponds to forbidden frequency bands, whereas magnon propagation is allowed for gray color. The air gap between the waveguide and the nanomagnets is chosen to be (a): $h = 175$ nm and (b): $h = 100$ nm.

shift of the band for higher values of M_{s1} . The second band behaves similarly under varying magnetization, whereas higher-order modes do not show a noticeable frequency shift. In Fig. 6.4 (b), one can see that for a reduced air gap size h between FM and SC, the spectrum is much more susceptible to changes in M_{s1} . That is because a reduction of h has a similar effect like increasing the magnetization of the nanocubes. In both cases, the stray field acting on the waveguide grows in magnitude, leading to a pronounced downward shift of specific frequency bands. However, for $h = 100$ nm, the frequency shift is much stronger than for $h = 175$ nm, and also, higher frequency bands show the tendency to become completely flat. With these observations at hand, it becomes easy to interpret the appearance of the lowest frequency band in Fig. 6.3 (b). The band at $f = 6.3$ GHz is located in the forbidden frequency region due to a frequency shift induced by the artificial vortex lattice.

If the magnetization is reduced to $M_{s1} = M_{s0}$, the stray field of the nanocubes resembles a realistic vortex field. In this case, one finds only a single band gap of width $\Delta f \approx 18$ MHz in the magnonic spectrum. Therefore, the width of this gap is considerably smaller than the one reported by Dobrovolskiy, where $\Delta f \approx 50$ MHz. The discrepancy between the results will be discussed at the end of this chapter.

6.3 Effect of the thickness of the wave guide

It is now investigated how the waveguide's thickness h_{FM} affects the magnonic dispersion. In order to reduce the computational effort, the width of the FM is set to $w = 65$ nm whereas its length $L = 28 \mu\text{m}$ remains as before. Furthermore, the magnetization of the artificial vortex lattice is set to $M_{s1} = 1M_{s0}$. At first, it should be mentioned that a reduction of the width w leads to a stronger mode quantization in the waveguide. As a consequence, higher-order modes are shifted upwards in frequency space. For the here

considered setup, the second band in Fig. 6.4 disappears completely since the microwave excitation signal only triggers magnonic modes of frequency $f < 20$ GHz. On the other hand, if the waveguide's thickness h_{FM} increases, dipolar interactions become of greater relevance. In that case, one can expect a typical BVMSW-type spectrum of the magnonic excitations.

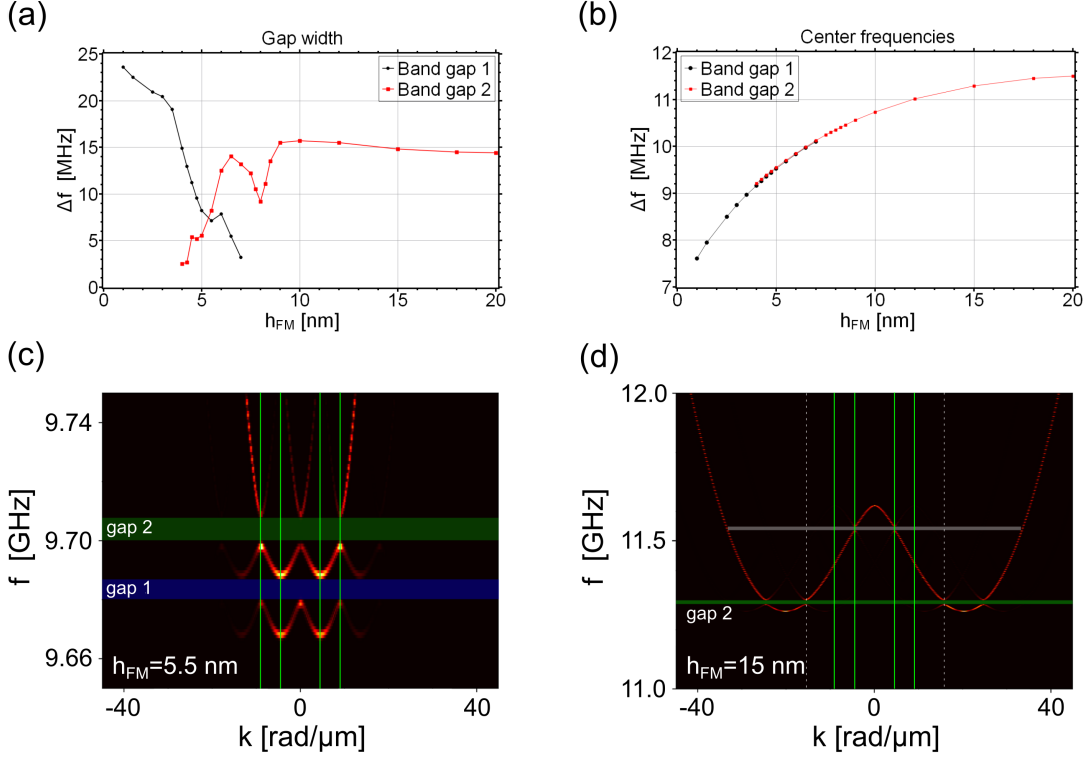


Figure 6.5: Dispersion properties of a magnonic wave guide of length $L = 28 \mu\text{m}$, width $w = 65 \text{ nm}$ and variable thickness h_{FM} . The magnetization of the artificial vortex lattice is set to $M_{s1} = 1M_{s0}$ leading to the formation of band gaps in the spectrum. (a),(b): width of the band gaps (a) and corresponding center frequencies (b) in dependence on the waveguide thickness. (c),(d): band diagrams for $h_{\text{FM}} = 5.5 \text{ nm}$ (c) and $h_{\text{FM}} = 15 \text{ nm}$ (d). Vertical green lines correspond to the first two Brillouin zone edges $k_1 = \pm\pi/a_{\text{VL}}$, $k_2 = \pm 2\pi/a_{\text{VL}}$. Dashed lines indicate gap opening at unconventional k -values.

In Fig. 6.5, it is shown how the width and center frequency of the band gaps change under variations of the waveguide thickness. For $h_{\text{FM}} = 1 \text{ nm}$ only one band gap of with $\Delta f \approx 23 \text{ MHz}$ appears in the spectrum. This value is somewhat larger than the gap width $\Delta f \approx 18 \text{ MHz}$ found for a FM of lateral extent $w = 700 \text{ nm}$. If h_{FM} is increased, the gap width gradually reduces until it becomes zero at $h_{\text{FM}} = 7.5 \text{ nm}$. At the same time, a second gap opens at $h_{\text{FM}} = 4 \text{ nm}$ remaining finite for intermediate and large thicknesses of the waveguide. Here it should be noted that gap widths of $\Delta f < 2 \text{ MHz}$ are not recorded in Fig. 6.5 (a). That is because the here considered simulation times did not allow for a sufficient resolution in frequency space (see, e.g., [202]).

In Fig. 6.5 (b), it is shown how the waveguide thickness affects the center frequencies of

the gaps. As already mentioned, an increasing h_{FM} leads to stronger dipolar interactions in the system. As a result, the entire spectrum is shifted upwards in frequency space leading to continuously increasing center frequencies of the band gaps. Also, the region in k -space where the group velocity is negative considerably widens. For $h_{\text{FM}} = 5.5 \text{ nm}$ one finds $v_g < 0$ inside the entire first BZ.

If the waveguide thickness is increased to large values, the dipolar shift of the spectrum saturates, and the system shows strong BVMSW behavior (see Fig. 6.5 (d)). In this regime, the center frequencies in Fig. 6.5 (b) show only a slight h_{FM} dependency. Also, only one complete band gap appears in the spectrum opening at unconventional k -values (dashed vertical lines). An interesting observation is the appearance of a second, incomplete band gap opening at the edges of the first BZ (grey bar). For a better understanding of these features, a logarithmic color scale was applied to the spectrum (cf. Fig. 6.6). Now it becomes clear that the complete band gap already opens at $k = \pm 0.5\pi/a_{\text{VL}}$ and inside the first BZ. It can also be seen that the incomplete band gap only affects modes with negative group velocity. In contrast, for $v_g > 0$, wave propagation in this frequency regime is not forbidden. An explanation for these features is still missing, and they will not be investigated further in this work. Nevertheless, the above discussion shows that the waveguide thickness is an important parameter in the problem of magnon-fluxon interaction. This point will be addressed again at the end of this chapter when comparing theory and experiment.

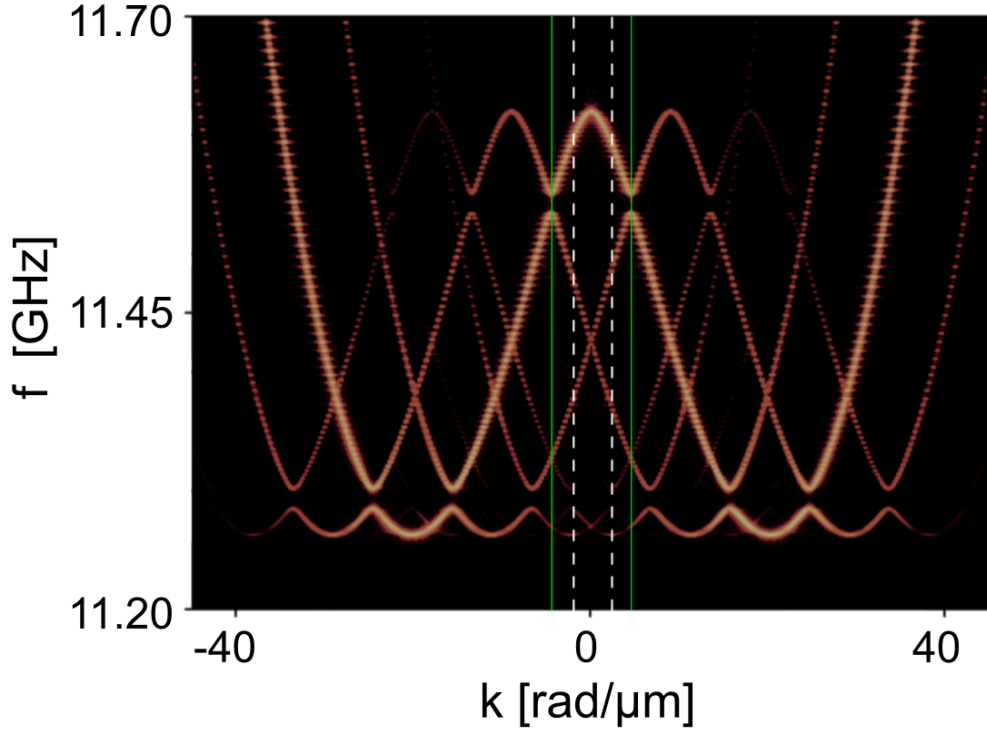


Figure 6.6: Band diagram corresponding to 6.5 (d) but with a logarithmic color scale. Vertical green lines correspond to the edges of the first BZ ($k_1 = \pm\pi/a_{\text{VL}}$), whereas dashed lines indicate a gap opening at $k_1 = \pm 0.5\pi/a_{\text{VL}}$.

6.4 Disordered vortex lattice

In this section, it is investigated how an imperfect vortex lattice affects magnon-propagation in the waveguide. Specifically, two kinds of disorder are of interest here. At first, variations in the supercurrent density between individual vortices are considered. In a perfectly clean material, the electronic mean free path l and the film thickness d are uniform, leading to a homogeneous GL-parameter κ throughout the sample. In contrast, real materials have a certain degree of impurity, and geometric imperfections are present, making the GL parameter a space-dependent quantity. As a consequence, the screening capabilities of the material are nonuniform, and the stray fields emanating from individual vortices are not identical in magnitude. That has also been shown in numeric simulations of superconducting wedges [246]. The uniform thickness gradient in such a sample leads to a space-dependent GL parameter allowing for vortex nucleation even if $\kappa < 1/\sqrt{2}$. But more importantly, vortices in the region of reduced sample thickness have weaker stray fields and smaller vortex cores due to an effective increase of κ . Even in mostly uniform thin films, structural imperfections can affect the equilibrium position of vortices. From an energetic point of view, it is beneficial for fluxons to populate positions of reduced sample thickness. This way, the volume threaded by supercurrents and the associated kinetic energy can be reduced. The new equilibrium state of the systems corresponds to a hexagonal vortex lattice with a certain degree of structural disorder.

A space-dependent electronic mean free path $l(\mathbf{r})$ affects the SC in a similar way, i.e., it makes the magnetic penetration depth λ , coherence length ξ and GL-parameter κ space dependent as well [29, 44].

In a real SC, the vortex lattice rarely meets structural perfection. Therefore, it is instructive to investigate how an imperfect lattice affects the interaction between magnons and fluxons. For simplicity, the effects of random vortex field magnitudes, and random vortex positions, are disentangled from each other. Instead, each kind of disorder is investigated separately.

6.4.1 Variations in field strength

In this section, it is investigated how random field variations between individual fluxons affect the magnonic dispersion. For the waveguide geometry, the one shown in Fig. 6.1 is chosen, i.e., the FM now has a width $w = 700$ nm, a thickness $h_{\text{FM}} = 1$ nm and a length $L = 28$ μm . Also, the air gap between the system constituents is reverted back to $h = 175$ nm.

The setup for the following calculations is shown in Fig. 6.7(a). Here, each black dot represents a superconducting vortex (or nanomagnet), and the sizes of the dots correspond to the magnetization M_{s1} . The ideal vortex lattice has perfect hexagonal order, and the stray fields of the fluxons are identical in magnitude. Disorder in the field amplitudes can be simulated by giving the magnetization of individual nanocubes a fixed random value in interval $[M'_{s1} - \Delta M, M'_{s1} + \Delta M]$. Here M'_{s1} is the magnetization in the absence of disorder, and ΔM is the maximum deviation from the ideal value. In the following calculations $M'_{s1} = 3.5M_{s0}$ is set allowing the formation of a band gap $f = 65$ MHz. This value better matches the experimentally obtained band gap width $f = 50$ MHz [85]. A second band gap $f = 12$ MHz is present as well, but its center

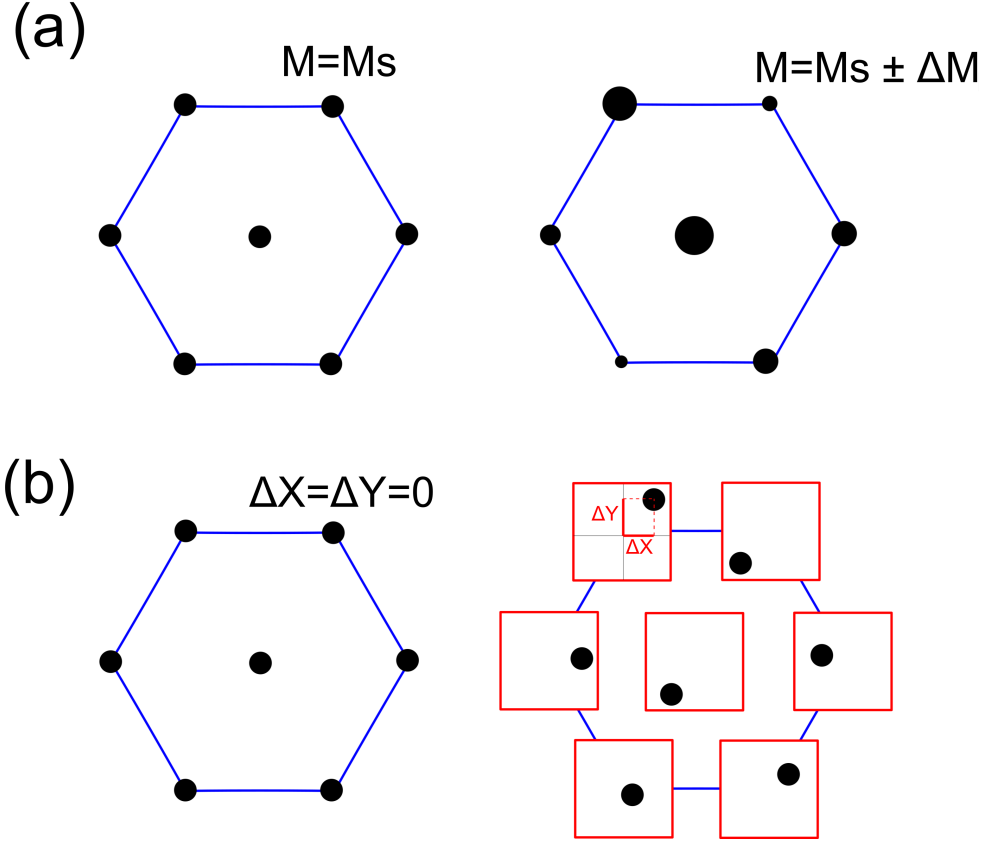


Figure 6.7: Setup to investigate effects of an imperfect vortex lattice on the magnonic dispersion. (a): artificial vortex lattice of perfect structural order but randomly varying magnetic moments. The size of each dot corresponds to the magnetization M_{s1} of individual nanomagnets. The disorder is introduced by giving each nanomagnet a random magnetization in the interval $[0.85M_{s1}, 1.15M_{s1}]$ or $[0.7M_{s1}, 1.3M_{s1}]$ with $M_{s1} = 3.5M_{s0}$. (b): artificial vortex lattice of uniformly magnetized nanodots. Each magnet can occupy a random position in a box of side length $a = 100$ nm or $a = 200$ nm. The boxes are centered around the ideal vortex positions in the absence of disorder.

frequency is outside the frequency region of interest.

In the here-presented calculations, three levels of disorder are considered. At first, it is investigated how the magnonic spectrum behaves for $\Delta M = 0$. Then, two calculations with $\Delta M = 0.15M'_{s1}$ and $\Delta M = 0.3M'_{s1}$ are performed and the results are compared. The spectrum without disorder is shown in Fig. 6.8. As in previous cases, the artificial vortex lattice leads to the formation of several band gaps in the magnonic spectrum. Thereby the lowest band has a small but finite dispersion.

If the magnetization M_{s1} is randomized, the band quickly flats out, and the dispersion becomes zero (cf. Fig. 6.9). Also, more flat bands appear in the formerly forbidden frequency region. In order to get a better understanding of the modifications of the spectrum for $\Delta M > 0$, a 1D Fourier Transformation of $\delta m_z(x, t)$ was performed in the time domain. For a selected number of frequencies, the corresponding Fourier amplitudes

are shown in the middle panels of Fig. 6.8 and 6.9. For a perfectly structured lattice ($\Delta M = 0$), the lowest order modes are located at positions where the vortex field opposes the external bias field. In the here considered case, that means $B_{vx} < 0$, as indicated by vertical blue lines. At such positions, the effective magnetic field in the waveguide is weakened, and the energy associated with magnonic modes is reduced. In this way, mode propagation is inhibited to some degree. The effect of mode confinement is also observable in the magnonic spectrum, where it leads to a loss of dispersion of the corresponding band. For high levels of disorder, the band becomes completely flat, and the magnonic mode can no longer propagate in the waveguide.

Upon inspection of the mode profiles in Fig. 6.9, one can see that for $\Delta M > 0$, the uniformly distributed Fourier peaks turn into a random arrangement of isolated knots. The incoherent oscillation of these knots prevents uniform wave propagation and leads to the appearance of additional flat bands in the dispersion plots. Only the low-frequency dipolar modes are affected by the randomization of the vortex stray field. The high-frequency modes are barely affected since they are mostly exchange driven.

With these observations at hand, it becomes possible to interpret the flattening of bands due to an increase of M_{s1} (cf. Fig. 6.4). A strong vortex field confines the low-frequency magnonic modes above the positions of the nanomagnets. Consequently, the corresponding bands become flat and are shifted downward in frequency space.

Similar mode confinement and frequency shifts have also been predicted to occur in surface-modulated magnonic crystals [184]. In this particular system, an array of grooves in the sample surface creates a periodic modulation of the waveguide stray field. The consequent modification of the magnonic spectrum is similar to the one presented here. Flat bands are also known to occur in waveguides with periodic Dzyaloshinskii-Moriya interaction [186].

6.4.2 Variations in field position

Now, the case of a vortex lattice with uniform magnetization $M_{s1} = 3.5M_{s0}$, but a structural disorder is discussed. As displayed in Fig. 6.7 (b), the nanomagnets can now occupy random locations in a box of side length $a = 100$ nm or $a = 200$ nm around their ideal positions. In Fig. 6.10, it can be seen that randomization of the vortex positions has a similar effect like a nonuniform field magnitude, i.e., the low-frequency modes become flat and coherent mode propagation is inhibited. In addition, this time, the exchange-driven modes are affected by lattice imperfection. That is especially true for $a = 200$ nm corresponding to high structural disorder. Here even the mode profiles for frequencies up to $f = 7.2$ GHz are highly distorted.

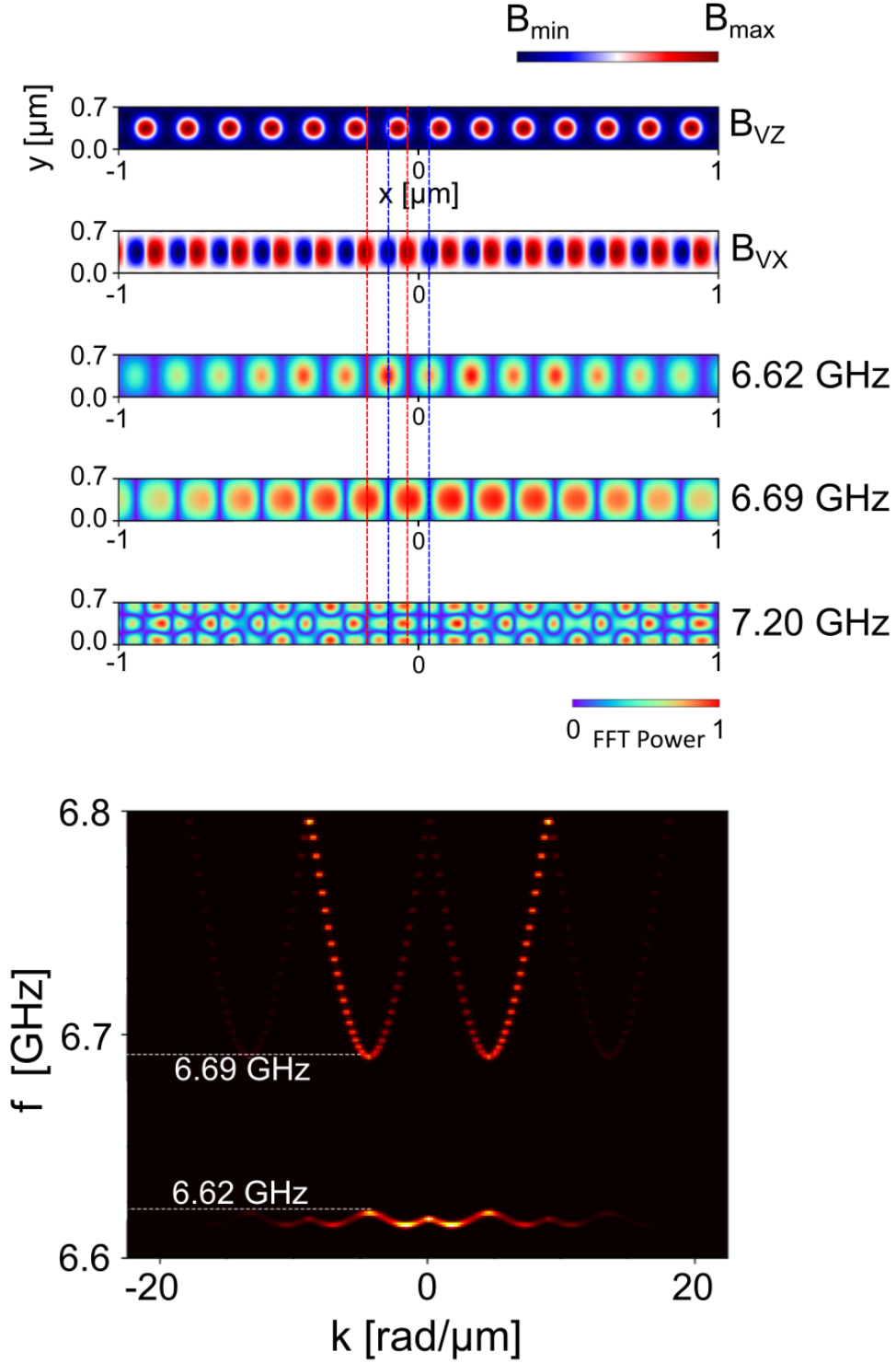


Figure 6.8: Band diagram for a perfectly structured vortex lattice. The magnetization of the replacement system is set to $M_{s1} = 3.5M_{s0}$ leading to the formation of a band gap $\Delta f = 65$ MHz. Upper panels: components B_{vx} and B_{vz} of the vortex field \mathbf{B}_v along the waveguide. Center panels: Mode profiles of selected frequencies. The vertical red lines mark positions in the waveguide where the in-plane field has maxima. Vertical blue lines mark the minima of the field.

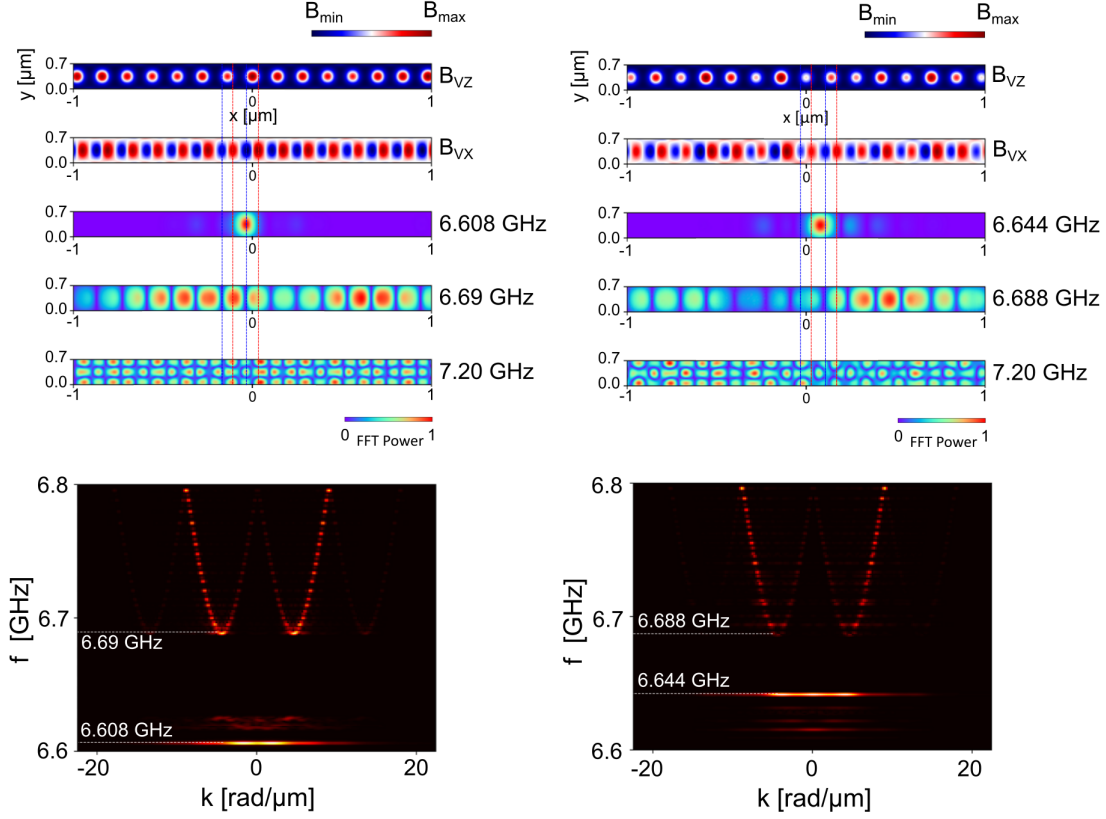


Figure 6.9: Band diagram for a disordered vortex lattice. The magnetization of individual nanocubes takes on random values from the interval $[0.85M'_{s1}, 1.15M'_{s1}]$ (left) and $[0.7M'_{s1}, 1.3M'_{s1}]$ (right) with $M'_{s1} = 3.5M_{s0}$. Upper panels: components B_{vx} and B_{vz} of the vortex field \mathbf{B}_v along the waveguide. Center panels: Mode profiles of selected frequencies. The vertical red lines mark positions in the waveguide where the in-plane field has maxima. Vertical blue lines mark the minima of the field.

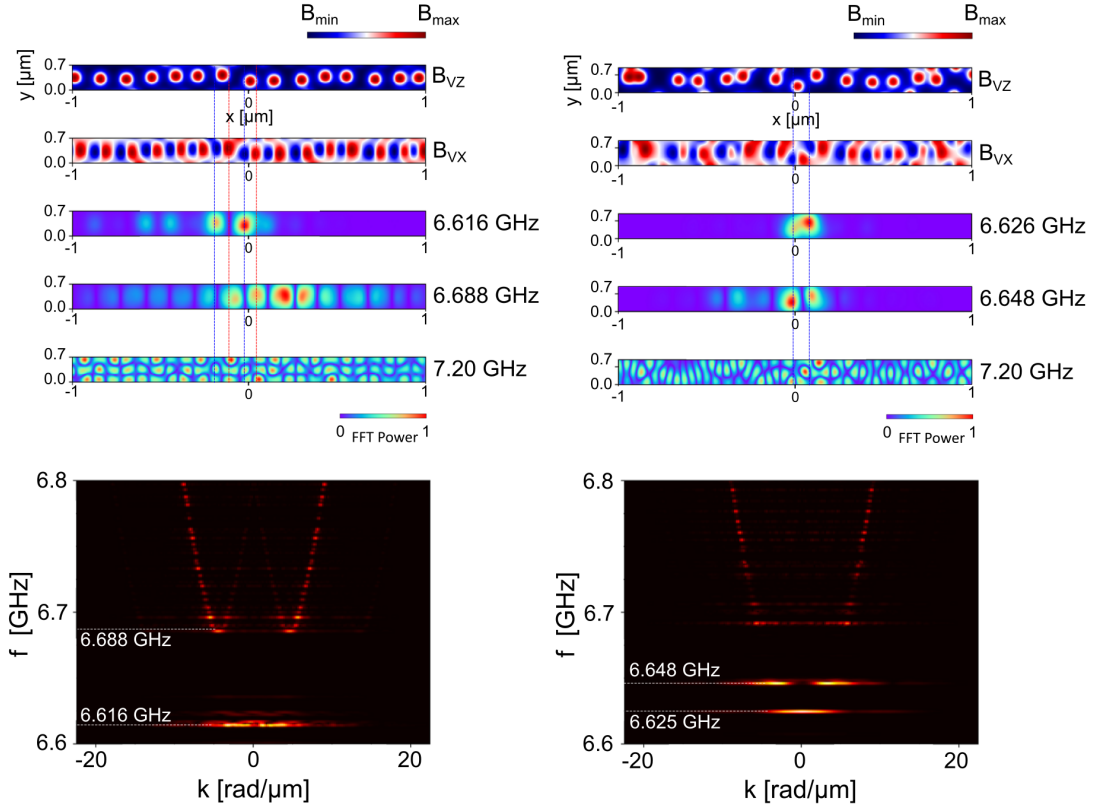


Figure 6.10: Band diagram for a disordered vortex lattice. The magnetization of the nanocubes is set to $M_{s1} = 3.5M_{s0}$. The disorder is introduced by allowing the magnets to occupy random positions in a box of side length $a = 100$ nm (left) or $a = 200$ nm (right) around their ideal position. Upper panels: components B_{vx} and B_{vz} of the vortex field \mathbf{B}_v along the waveguide. Center panels: Mode profiles of selected frequencies. The vertical red lines mark positions in the waveguide where the in-plane field has maxima. Vertical blue lines mark the minima of the field.

6.5 Summary and comparison with experiment

In this work, a simplified method for investigating the interaction between magnonic excitations and superconducting vortices was presented. Thereby, the stray field of a static vortex lattice was fitted to the magnetic field distribution of a lattice of ferromagnetic nanodots. It was found that the presence of the artificial vortex field leads to the formation of band gaps in the magnonic spectra due to conventional Bragg scattering at the BZ boundaries. The in-plane component of the vortex field was found to be the main driving factor for gap formation, whereas the perpendicular component was confirmed to be negligible. The calculated spectra showed high susceptibility to changes in the waveguide geometry, the field strength of individual vortices, and the spatial distribution of fluxon. Furthermore, it was found that the vortex fields are able to confine dipolar magnonic modes causing a shift of the corresponding bands to lower frequencies.

Several open questions remain, as becomes evident by comparing the numeric results with the experiment of Dobrovolskiy et al. [85]. In order to enable such a comparison, material parameters and SC geometry were chosen as in the experiment. Also, the external magnetic field $B_{\perp} = 5 \text{ mT}$ was adapted to simulate a realistic vortex distribution. The system size in the calculations is comparable to the experiment as well. However, the FM geometry could not be matched due to the numerical complexity of the resulting problem. The difference in the waveguide geometry can be considered one of the main reasons for no quantitative agreement between the here-presented calculations and the experiment. For comparison: in most of the simulations, the FM was chosen to have a width of $w = 700 \text{ nm}$ and thickness $d = 1 \text{ nm}$. Under the influence of a realistic vortex field ($M_{s1} = M_{s0}$), the corresponding magnonic spectrum consists of two allowed frequency bands separated by a gap of width $f = 18 \text{ MHz}$. In the experiment, the waveguide had a width of $w = 2 \mu\text{m}$ and thickness $d = 80 \text{ nm}$, giving rise to two band gaps of widths $f \approx 50 \text{ MHz}$. Apart from the geometric sample mismatch, it could also be possible that the vortex field in the experiment was stronger than here. This modification of \mathbf{B}_v is possible when the interaction of the SC with its own stray field can not be considered negligible. At the same time, a larger vortex field would lead to stronger mode confinement, and the corresponding band shift potentially widens existing band gaps. Another source of error could be an inaccurate estimate of the GL parameter, which was set to $\kappa = 1$. It should also be considered that the superconducting vortex field is highly nonhomogeneous in space. In a thicker waveguide, such a field affects magnonic modes at the top and bottom of the FM differently. Finally, the dynamic interaction between the SC and FM was neglected as well. That also includes a potential modification of the FM's dynamic stray fields due to the conventional Meißner screening of the nearby SC. For example, electromagnetic coupling between FM and SC is known to be connected with enhanced phase velocities and nonreciprocal magnon dispersion [247, 248].

7 Temperature-driven vortex dynamics

In experiments, it is found that a local increase in temperature exerts a force on nearby vortices and drives them out of equilibrium [141, 144]. Thereby, the force direction is such that the vortices find their new equilibrium position at the center of the hot spot. This temperature-induced vortex motion is interesting for applications since it allows precise control of the position of individual vortices. For example, this idea could find use in fluxonic memory devices [77–79]. Also, by carefully adjusting the hot spot size, it is possible to sweep the vortices out of certain areas in the SC [144]. In particular for nanosystems such vortex cleansing could be interesting since it potentially allows to reduce energy dissipation associated with unwanted vortex motion.

Apart from its potential practical use, temperature-driven vortex motion is also fascinating on a theoretical level. However, many of the studied systems only consider the static equilibrium configuration of fluxons in the presence of uniform temperature gradients [135, 137, 138]. A detailed, TDGL-based analysis of the dynamic interaction between a fluxon and a nonhomogeneous temperature field is still pending at the moment of writing. For example, an open question is how the size of the vortex core and the exact distribution of supercurrents affect the attractive force on the vortex [144].

In a realistic situation, the temperature-induced dragging force is counterbalanced by pinning forces. Such effects are not considered in this work. Instead, the dynamic interaction between an isolated fluxon and a nearby hot spot is investigated. A detailed analysis of the TDGL equations reveals which role the supercurrent distribution and density variations in the superconducting condensate play. It is found that the superfluid velocity \mathbf{v} of the vortex and the density of superconducting charge carriers n_s near the vortex core play a key role in the problem. It is demonstrated that an interaction of the form $\mathbf{v} \cdot \nabla n_s$, induced by the external heat source, has the same effect on the vortex as an electric field. Therefore, the hot spot exerts a force onto the vortex that is similar to the conventional Lorentz force due to external current flow. Furthermore, it will be shown how different probe geometries affect the interaction between the vortex and the temperature field.

7.1 Setup

Fig. 7.1 shows the system under investigation. The SC is a semi-infinite cuboid of side length $L = 18 \mu\text{m}$, with $w = 4.5 \mu\text{m}$ and a height h much larger than the GL-coherence length ξ_{GL} . A superconducting vortex is placed at the center of the structure, and its interaction with a nearby hot spot at $x = 2.25 \mu\text{m}$ is investigated. In the dynamic processes described later, the vortex will gradually approach the edge at $x = 9 \mu\text{m}$. That makes the interaction between supercurrent and boundary a complicated time-dependent function and the dynamic processes hard to interpret. To avoid such complexities, the SC is chosen to be comparably long. On the other hand, even under external drive the

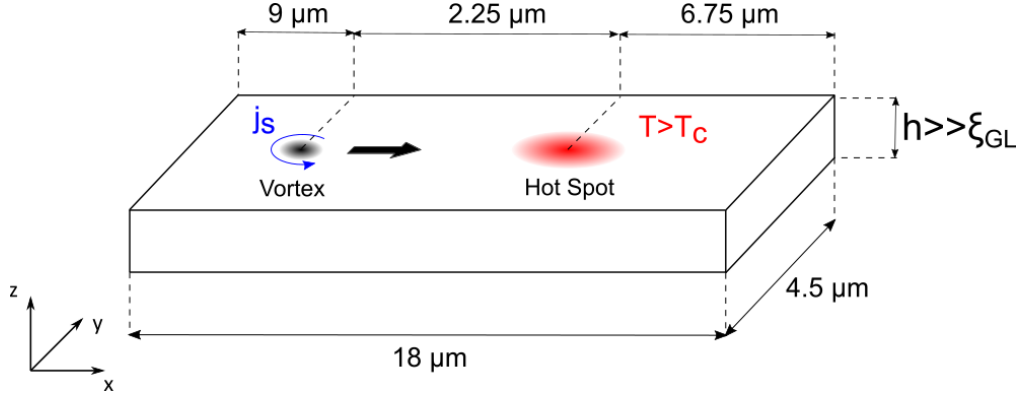


Figure 7.1: Setup of the system. The SC is a rectangular prism of length $L = 18 \mu\text{m}$, width $w = 4.5 \mu\text{m}$ and height $h \gg \xi_{\text{GL}}$. At the center of the strip, a vortex is located with supercurrents \mathbf{j}_s flowing around it. Its interaction with a nearby hot spot is the subject of study. The large arrow indicates the moving direction of the vortex in the absence of pinning forces.

vortex keeps a constant distance to the boundaries at $y = \pm 2.25 \mu\text{m}$. Therefore, w can be considered a static, system-specific parameter.

The system is simulated by solving the normalized TDGL-equations (3.1)-(3.3) together with the equilibrium heat equation

$$0 = \Delta T + T_c f(\mathbf{r}) - \eta_3(T - T_0). \quad (7.1)$$

For simplicity, the material constants η_1 and η_2 are set to unity and the operating temperature to $T_0 = 0.9T_c$. Correspondingly one has $D = \tau/\xi_{\text{GL}}(T_0)^2$ and $\sigma = \tau/(\mu_0\lambda_{\text{GL}}(T_0)^2)$. The basic time unit in (3.5) (3.6) is chosen to be $\tau = 0.1 \text{ ps}$. The temperature is a space-dependent function with values $T \geq T_0$ and $T_0 \leq T_c$. That means in the absence of magnetic fields and for homogeneous temperature distribution eq. (3.1) has equilibrium solutions $|\Psi(T_0)|^2 = 1$ (indicating perfect superconductivity) and $|\Psi(T \geq T_c)|^2 = 0$ (normal conductivity). The boundary conditions for equations (3.1) and (3.2) are chosen as

$$\left(\frac{\nabla \Psi}{in\kappa} - n\Psi\mathbf{A} \right) \cdot \mathbf{n} = 0, \quad \text{on } \partial\Omega_{\text{SC}} \quad (7.2)$$

$$(\nabla \times \mathbf{A}) \times \mathbf{n} = \mathbf{B}_e \times \mathbf{n}, \quad \text{on } \partial\Omega_{\text{SC}}. \quad (7.3)$$

Equation (7.3) ensures the continuity of the tangential component of the magnetic flux density across the superconducting interfaces. It is applicable if the stray field \mathbf{B}_s of the SC has a vanishing tangential component at the interfaces, e.g., for infinitely long superconducting prisms. The scalar potential appearing in the TDGL equations can be eliminated by applying a suitable gauge. In this work, $\phi = -\nabla \cdot \mathbf{A}$ is chosen, which requires the additional boundary condition $\mathbf{A} \cdot \mathbf{n} = 0$ for the vector potential [97]. Furthermore, the total vector potential is split into its individual contributions $\mathbf{A} = \mathbf{A}_s + \mathbf{A}_e$, where \mathbf{A}_s is the contribution of the superconducting stray field and \mathbf{A}_e is the vector potential of external magnetic fields. For the latter one, it is suitable to choose a modified Landau gauge $\mathbf{A}_e = -B_e y \mathbf{e}_x + \nabla u$ where the gauge field u ensures that $\nabla \cdot \mathbf{A}_e = 0$ and

$\mathbf{A}_e \cdot \mathbf{n} = 0$ on $\partial\Omega_{SC}$. With these presets, the boundary conditions of the system can be reformulated as

$$\mathbf{A}_s \cdot \mathbf{n} = 0, \quad \text{on } \partial\Omega_{SC} \quad (7.4)$$

$$\nabla\Psi \cdot \mathbf{n} = 0, \quad \text{on } \partial\Omega_{SC} \quad (7.5)$$

$$(\nabla \times \mathbf{A}_s) \times \mathbf{n} = 0, \quad \text{on } \partial\Omega_{SC}. \quad (7.6)$$

For the heat equation (7.1) the boundary condition

$$T = T_0, \quad \text{on } \partial\Omega_{SC} \quad (7.7)$$

is applied, ensuring the equilibrium solution $T = T_0$ in the absence of heat sources. The material constant in (7.1) is set to $\eta_3 = 1.67 \times 10^{-7}$, a value very similar to the one used in [141]. An external heat source, e.g., a laser beam hitting the superconducting surface, is described by the space-dependent function f . In the here-considered case $f = f_0$ inside a circular region of radius $b = 100$ nm located at $(2.25 \mu\text{m}, 0, 0)$ (see Fig. 7.1). Outside that region, $f = 0$ is set. The simulation procedure is now the following. For a chosen value of f_0 , equation (7.1) is solved and the obtained temperature field is used as input for the TDGL-equations. Equations (3.1) and (3.2) are then solved selfconsistently for the given temperature until an equilibrium solution is found. The dynamic behavior of the vortex is recorded and evaluated for a number of selected time steps.

7.2 Results

7.2.1 Temperature induced vortex motion

For a first principal investigation of the system, the material parameters are chosen as $\lambda_{GL} = 450$ nm and $\xi_{GL} = 150$ nm resulting in $\kappa = 3$. In a more realistic scenario, one could use the material parameters of Nb, in particular, $\lambda_{GL} = 150$ nm and $\lambda_{GL} = 50$ nm, depending on the purity of the material [44]. However, a reduction of either λ_{GL} or ξ_{GL} was found to deteriorate the numerical accuracy of the results due to increasing levels of numeric noise. A better spatial resolution in the FEM-formalism could resolve this problem. However, operating with such a high-density mesh would substantially increase the computational time. In addition, the principal dynamic behavior of the vortex was not observed to depend on the specific choice of material. Therefore, choosing comparably large values of λ and ξ is convenient. In the following, it is discussed how a local hot spot affects the vortex.

Before the heat source is switched on, the vortex sits at the center of the SC, and the system is in equilibrium. In the here considered case, no external magnetic fields are applied, and a non-equilibrium situation only arises once the temperature is raised in the vicinity of the vortex. In Fig. 7.2, it can be seen that with an increasing value of f_0 , the temperature at the center of the hot spot increases as well. The order parameter adapts to the modified temperature distribution, and, as a result, the vortex is deflected from the coordinate center. The entire dynamic process can be roughly divided into three stages. Shortly after the heat is applied, the deflection ΔX grows linearly, and the vortex moves at an approximately constant speed. As the vortex draws closer to the heat bubble, its velocity increases until a maximum is reached. In the final phase of the process,

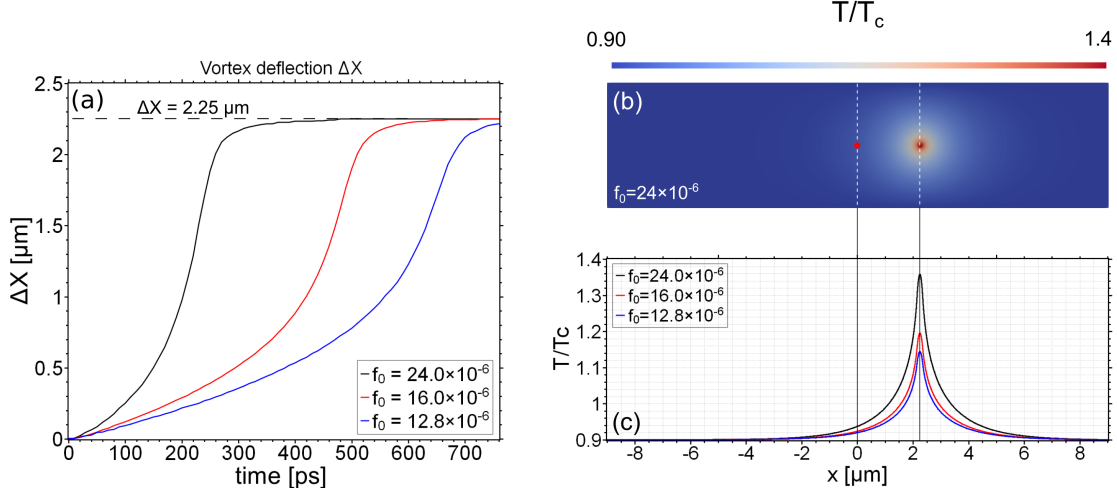


Figure 7.2: (a): Deflection of the vortex from the coordinate center due to a nearby hot spot. For $\Delta X = 2.25 \mu\text{m}$, the vortex finds a new equilibrium position at the center of the heat bubble. (b): Temperature distribution in the SC for $f_0 = 24 \times 10^{-6}$. The red dot at $x = 0$ marks the initial position of the vortex. (c): Temperature profile along the x-axis for different values of f_0 .

the vortex enters the heated region and finds a new equilibrium at $x = 2.25 \mu\text{m}$. The principal character of the heat-induced vortex motion was observed to be independent of the actual value of f_0 . On the other hand, the maximum velocity and the total time of the entire process strongly depend on the heat distribution in the SC. The here-presented results correspond to the case of a perfectly clean SC without material imperfections. For such a material, each nonzero value $f_0 > 0$ is potentially able to trigger vortex motion. However, the transition time of the dynamic process goes to infinity for an ever increasing distance between the vortex and the hot spot.

In order to determine the mechanisms that drive the vortex out of equilibrium, the order parameter is reformulated into its amplitude-phase form $\Psi = \Psi_0 e^{i\theta}$. By inserting this Ansatz into the dimensionless TDGL-equations (3.1)-(3.3) and splitting into real and imaginary parts, the system of partial differential equations takes on the form

$$\eta_1 \frac{\partial \Psi_0}{\partial t} + \Psi_0 \left(\Psi_0^2 - 1 + \frac{T - T_0}{T_c - T_0} \right) - \frac{\Delta \Psi_0}{n^2 \kappa^2} + \Psi_0 \left(\frac{\nabla \theta}{n\kappa} - n\mathbf{A} \right)^2 = 0 \quad (7.8)$$

$$\eta_1 \left(\frac{\partial \theta}{\partial t} + \kappa \phi \right) \Psi_0^2 = \frac{\nabla}{n\kappa} \cdot \mathbf{j}_s \quad (7.9)$$

$$\mathbf{j}_s = \Psi_0^2 \left(\frac{\nabla \theta}{n\kappa} - n\mathbf{A} \right). \quad (7.10)$$

The principal form of the second TDGL-equation (3.2) remains unchanged under the transformation. In the absence of temperature gradients and electric fields, the vortex is at rest, and (7.9) demands that $\nabla \cdot \mathbf{j}_s = 0$. In the here-considered case, electric fields only appear in non-equilibrium situations, e.g., when a vortex is created at the sample boundary or a transport current is injected into the SC. If the material is heated locally,

the condensate field Ψ_0 changes according to (7.8). The modified order parameter then affects the phase field via equation (7.9), and a non-equilibrium situation arises where $\nabla \cdot \mathbf{j}_s \neq 0$. As a consequence, the time evolution of θ is driven in a way that the divergence of \mathbf{j}_s is compensated - the vortex is deflected towards the hot spot. The phase field and the condensate field thereby evolve simultaneously in time, and the vortex core follows the deflected phase singularity. If pinning is strong enough, the temperature-induced driving force can be compensated by the pinning force, and a new equilibrium is established. In the absence of pinning forces, a new equilibrium configuration can only arise once the vortex has entered the heat bubble. With these observations, the temperature-induced divergence of the supercurrent density can be identified as the driving force for the vortex core. In order to get further insight into the problem, equation (7.9) is reformulated into

$$\eta_1 n_s \frac{\partial \theta}{\partial t} = \frac{1}{n\kappa} \nabla n_s \cdot \mathbf{v}_s + n_s \left(\frac{1}{n\kappa} \nabla \cdot \mathbf{v}_s - \eta_1 \kappa \phi \right) \quad (7.11)$$

where $\mathbf{v}_s = 1/(n\kappa) \nabla \theta - n\mathbf{A}$ is the superfluid velocity. Specifically, now it is searched for the condition under which $\nabla \cdot \mathbf{j}_s = 0$ is no longer possible, and the time evolution of θ is inevitable. From equation (7.11), it can be immediately seen that the divergence of \mathbf{v}_s has the form of a scalar electric potential. On the other hand, it is commonly known that an electric current flow associated with $\nabla \phi$ exerts a Lorentz force onto the vortex and drives it out of equilibrium. Therefore, it becomes evident that the temperature-induced modification of n_s leads to a divergence of the supervelocity, which acts on the vortex as a conventional transport current. To elaborate on this point further, one can define the potentials

$$\phi_1 = \frac{1}{n\kappa} \nabla n_s \cdot \mathbf{v}_s \quad (7.12)$$

$$\phi_2 = \frac{1}{n\kappa} n_s \nabla \cdot \mathbf{v}_s \quad (7.13)$$

which in equilibrium have the property $\phi_1 = -\phi_2$. Before the temperature-induced vortex motion is investigated in more detail, it is instructive to analyze how the potentials ϕ_1 and ϕ_2 behave if an electric current drives the vortex.

7.2.2 Current induced vortex motion

An electric current flow in the SC can be simulated by solving (3.1)-(3.4) together with the continuity equation

$$0 = -\eta_2 \nabla \cdot \left(n \frac{\partial \mathbf{A}}{\partial t} + \frac{1}{n} \nabla \phi \right) + \nabla \cdot \mathbf{j}_s \quad (7.14)$$

with the methods described in [210]. That means the SC geometry is now reduced to a very thin film in which the effects of superconducting stray fields can be neglected, i.e., $\mathbf{A}_s = 0$. Additionally the boundary conditions (5.6) - (5.8) are applied with $\partial\Omega_v$ denoting the insulator boundary at $x = \pm 9 \mu\text{m}$. The electrode boundary for current injection is located at $y = \pm 2.25 \mu\text{m}$. For the following discussion, it is sufficient to choose a comparably small transport current $\mathbf{j}_e = j_e \mathbf{e}_y$ with $j_e = 0.01 \sqrt{2} B_{\text{cth}} / (\mu_0 \lambda_{\text{GL}}) = 85.9 \text{ MA/m}^2$. In this way, the vortex is deflected along the positive x-direction due to

the Lorentz-force $\mathbf{F}_L = \mathbf{j}_e \times \mathbf{B}$.

This simple relation no longer predicts the correct dynamics if $\mathbf{A} = 0$ is assumed since it implies $\mathbf{F}_L = 0$. That would mean the vortex remains static under arbitrary transport currents. However, under realistic conditions, the magnetic field of individual vortices is never vanishingly small and therefore $\mathbf{A}_s \neq 0$.

The time-dependent vortex deflection due to \mathbf{j}_e is shown on the left side in Fig. 7.3. As the current is switched on, the vortex experiences a short acceleration phase during

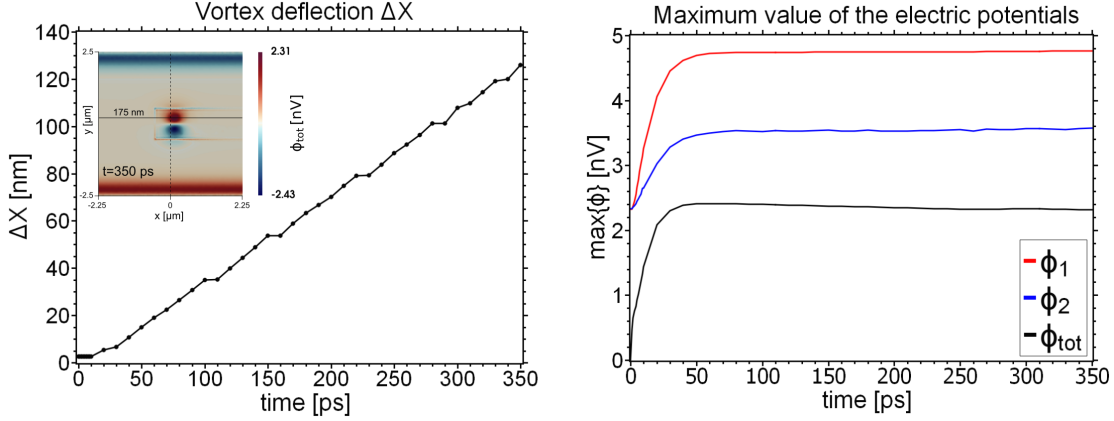


Figure 7.3: Left: Time-dependent deflection ΔX of the vortex along the x-axis due to an external current $\mathbf{j}_e = j_e \mathbf{e}_y$ with $j_e = 8.59 \text{ GA/m}^2$. The inset shows the total electric potential $\phi_{\text{tot}} = \phi_1 + \phi_2$ at $t = 350 \text{ ps}$. Right: Time evolution of the global maximum values of the electric potentials ϕ_1 , ϕ_2 , and ϕ_{tot} . At all simulation times, the maximum of ϕ_{tot} is located on the axis ($x, y = 175 \text{ nm}$).

which it is almost immobile. In this phase, the potentials ϕ_1 and ϕ_2 quickly build up in magnitude. After 50 ps, the system develops a dynamic equilibrium. Here the vortex moves with constant velocity along the x-axis, and the magnitude of the potentials becomes constant as well. Once the system has stabilized, the moving vortex creates its own electric potential $\phi_{\text{tot}} = \phi_1 + \phi_2$, which counteracts the applied electric field. This dynamic electric field is commonly associated with the unwanted energy dissipation of a moving vortex. Technically it is equivalent to the gauge-invariant time evolution of the superconducting phase field, which appears on the left side in equation (7.9).

The spatial distribution of the electric potentials is shown in Fig. 7.4. Before the electric current is applied, the system is at rest and $\phi_1 + \phi_2 = 0$. In an infinitely extending system, both potentials would be initially zero since the supercurrents around the vortex core have only angular components, whereas the condensate gradient has only radial components giving $\nabla n_s \cdot \mathbf{v}_s = 0$. However, the here-presented system has only a semi-infinite geometry since the strip length and width are finite. Specifically, the boundaries closest to the vortex lead to a deformation of the velocity field \mathbf{v}_s due to the imposed boundary condition (7.2). This geometry-induced distortion of the phase field leads to a nonzero initial distribution of the electric potentials. Note, the initial electric fields associated with $\phi_{1,2}$ have no accelerating effect on the vortex since the corresponding Lorentz forces cancel each other (see black arrows in Fig. 7.4(g)).

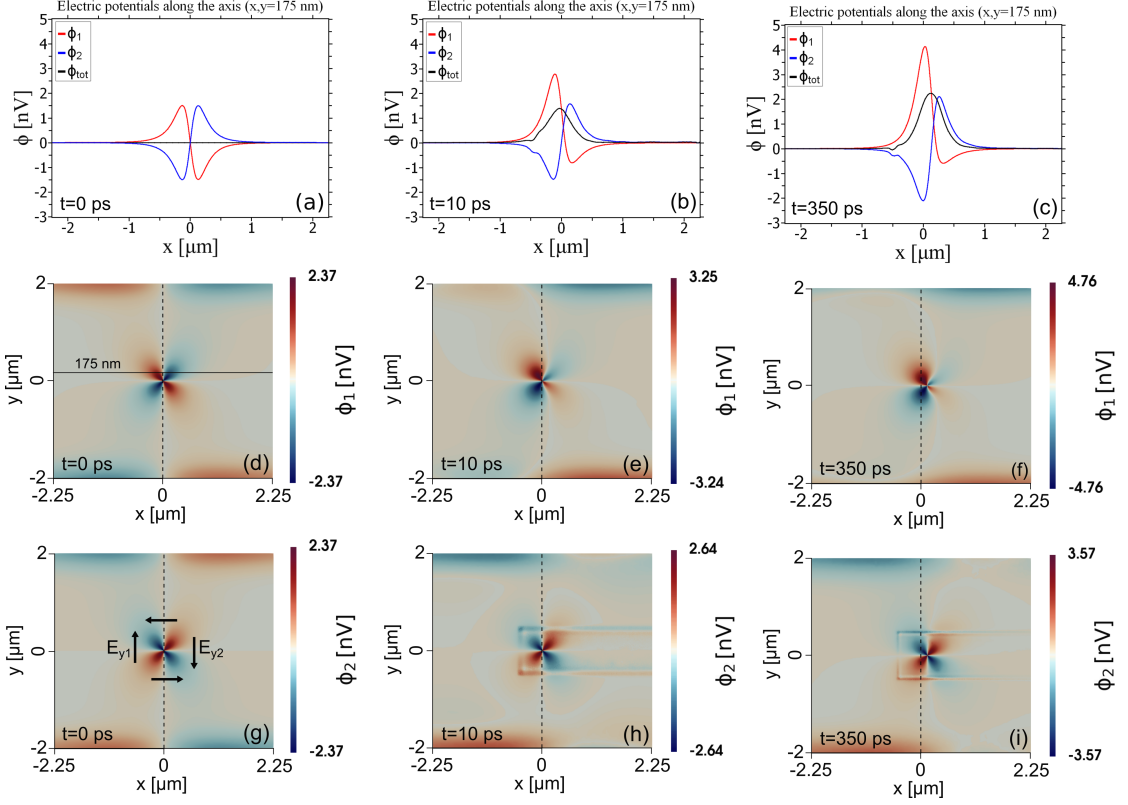


Figure 7.4: Time evolution of the electric potentials ϕ_1 , ϕ_2 and ϕ_{tot} due to an external current $\mathbf{j}_e = j_e \mathbf{e}_y$ with $j_e = 8.59 \text{ GA/m}^2$. (a)-(c): Line plots of the potentials along the axis ($x, y = 175 \text{ nm}$) at selected times. (d)-(f) and (g)-(i) spatial distribution of ϕ_1 and ϕ_2 respectively. The black arrows in (g) correspond to the principal direction of the electric field $\mathbf{E} = -\nabla\phi_2$.

When a transport current is injected into the system, the balance between ϕ_1 and ϕ_2 is disturbed, and the magnitude of the potentials increases. Initially, the system's time evolution is driven by the applied potential. Thereby the time derivative $\partial_t\theta$ tends to counteract the applied electric potential and, as a result, the time evolution of ϕ_1 and ϕ_2 is driven as well. In this process, ϕ_2 remains symmetric around the vortex core, which means it does not accelerate on the vortex. In contrast, the potential ϕ_1 loses its symmetry leading to $E_{y1} > E_{y2}$. Therefore it can be concluded that the deformation of the fields n_s and θ gives rise to an electric potential $\phi_1 \sim \nabla n_s \cdot \mathbf{v}_s$ opposing the current-driven vortex motion. The final velocity of the vortex is limited by the total field $\phi_{\text{tot}} \sim \nabla \cdot \mathbf{j}_s$, which, in return, is coupled to the maximum velocity at which the normal conducting vortex core can move. This velocity depends on the dynamics of the condensate field, i.e., equation (7.8). That means, if the vortex is pinned and the core is immobile, the phase field will adapt such that $\phi_{\text{tot}} = 0$.

7.2.3 Temperature induced vortex motion – interpretation in terms of electric potentials

In the previous section, it was investigated how an applied electric field drives the time evolution of the superconducting phase field. In this process, it was observed that the divergence of \mathbf{j}_s becomes nonzero in response to the deflection of the vortex core, and a dynamic equilibrium is established defined by (7.9). However, if the vortex is solely driven by a temperature gradient, the situation is reversed. Such a temperature-induced

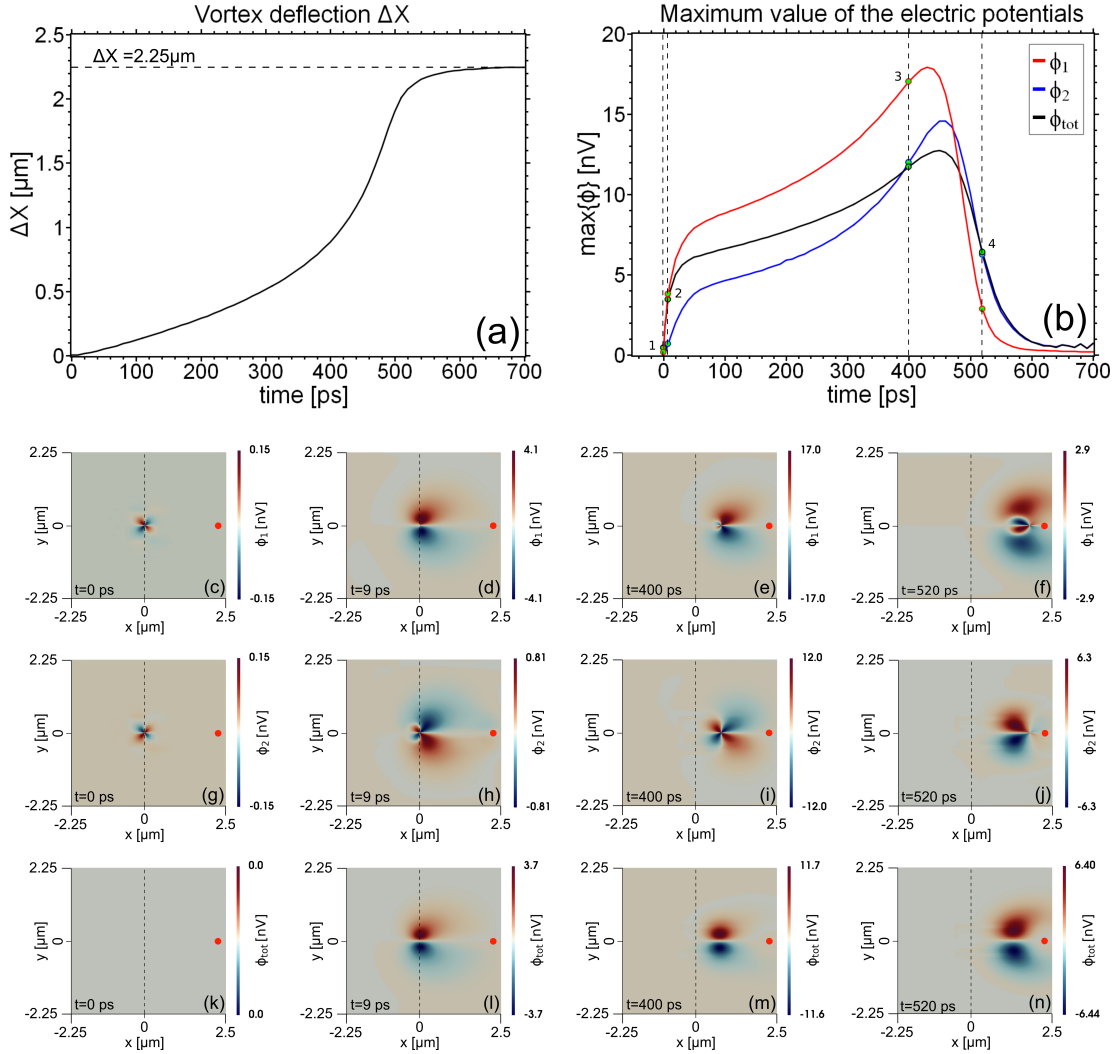


Figure 7.5: (a): Time-dependent deflection ΔX of the vortex along the x-axis due to a hot spot located at $x = 2.25 \mu\text{m}$ with $f_0 = 16 \times 10^{-6}$. (b): Time evolution of the global maximum values of the electric potentials ϕ_1 , ϕ_2 , and ϕ_{tot} . (c)-(n): spatial distribution of ϕ_1 , ϕ_2 , and ϕ_{tot} for times indicated in (b) (green dots). The red dot marks the position of the hot spot.

modification of the condensate field n_s leads to a non-equilibrium situation and, since

now $\phi_{\text{ext}} = 0$, the time evolution of the superconducting phase field θ is driven by $\nabla \cdot \mathbf{j}_s$. In Fig. 7.5, the principal behavior of the system is shown. Initially, the vortex is at rest, and no external electric or magnetic fields are applied. Once the heat source is switched on, the phase field is deformed, and the vortex is deflected along the x-axis (see Fig. 7.5 (a)). Similarly to a transport current, the temperature field leads to a vortex deflection that is initially almost linear. However, the force that acts on the vortex depends now on the distance toward the hot spot, and the vortex experiences a phase of strong acceleration before it enters the center of the heat bubble. This dynamic behavior is also reflected in the time evolution of the scalar potentials ϕ_1 and ϕ_2 .

In Fig. 7.5 (b), it can be seen that the potentials initially grow rapidly in magnitude and $\phi_1 \approx \phi_{\text{tot}}$. The force that drives the vortex out of equilibrium is therefore found to be of the form $\nabla n_s \cdot \mathbf{v}_s$. As the vortex approaches the hot spot, the electric fields continue increasing toward a global maximum. In the final stage of the process, the vortex enters the hot spot, and ϕ_{tot} rapidly goes to zero. In this phase, the potential ϕ_2 plays a dominant role in the fluxon dynamics since now $\phi_2 \approx \phi_{\text{tot}}$. Therefore, close to the hot spot, the vortex is predominantly driven by a strong divergence of the superfluid velocity \mathbf{v}_s , and the driving potential has the form $n_s \nabla \cdot \mathbf{v}_s$.

The temperature-induced dynamics can also be understood by recalling that equation (7.11) has a mathematical form that resembles a convection-diffusion equation for the superconducting phase field θ . Using the London-gauge $\nabla \cdot \mathbf{A} = 0$ one can therefore write

$$\eta_1 n_s \left(\frac{\partial \theta}{\partial t} + \kappa \phi \right) n_s + \frac{1}{n\kappa} (-\nabla n_s) \cdot \left(\frac{1}{n\kappa} \nabla \theta - n \mathbf{A} \right) - \frac{1}{n^2 \kappa^2} n_s \Delta \theta = 0 \quad (7.15)$$

The second term on the left corresponds to $-\phi_1$ and describes the advection of the superconducting phase in response to a change in the condensate field n_s . In this picture, the phase of the vortex tends to "flow" into directions of reduced condensate density (defined by $-\nabla n_s$), provided that $\nabla n_s \cdot \nabla \theta \neq 0$. The ensuing local build-up in phase is counterbalanced by the diffusive nature of θ , which is described by the third term in (7.15). In Fig. 7.5, it can be seen that the corresponding potential $\phi_2 \sim n_s \Delta \theta$ has a strong dependence on the actual state of the condensate field. In regions of reduced order parameter density, the diffusive nature of θ is stronger since the time evolution of the phase is directly coupled to n_s (see the first term in (7.15)). As a result, the phase change due to the moving vortex is also stronger inhibited, and the viscous drag force corresponding to ϕ_2 is enhanced. However, ϕ_2 not only has a phase-equalizing effect. The potential also gives rise to a nonzero force component along the direction of vortex motion, induced by $E_{y1} = -\nabla \phi_2 \sim \mathbf{e}_y$. The electric field E_{y1} is defined in the same way as in Fig. 7.4 (g), i.e., $-\nabla \phi_2$ is evaluated at the "left side" of the vortex. In close vicinity to the heat bubble, this field becomes the actual driving force for the vortex since $E_{y2} = -\nabla \phi_2 \sim -\mathbf{e}_y$ is strongly suppressed inside the hot spot. (see Fig. 7.5 (h)-(j)). By comparison, for a current-driven vortex, ϕ_2 was not observed to play an important role in the dynamics. In the scenario of a current-driven vortex, the condensate field is mostly uniform, and the forces due to $\mathbf{E} = -\nabla \phi_2$ cancel each other.

Vortex dynamics for different sample geometries

In this section, the effect of the sample geometry on the vortex dynamics is discussed. Specifically, the question is addressed of how the SC strip width w affects the temperature-induced vortex motion. For this reason, three different simulations were conducted where the strip width was gradually reduced from $w = 4.5 \mu\text{m}$ down to $w = 2.5 \mu\text{m}$. The system's initial configuration was chosen to be the same as before, i.e., the vortex was placed at the coordinate center, and a hot spot with $f_0 = 16 \times 10^{-6}$ was applied at $x = 2.5 \mu\text{m}$. During the simulation, the vortex location and the local maximum values of the electric pseudo-potentials $\phi_{1,2}$ and ϕ_{tot} were recorded. In Fig. 7.6, one can see that the principal dynamical behavior of the system is the same as before, and the vortex experiences a phase of strong acceleration before it finds a new equilibrium position inside the hot spot. However, in Fig. 7.6 (a), one can see that reducing the strip width still considerably affects the temperature-induced vortex deflection ΔX . For $w = 2.5 \mu\text{m}$, the fluxon acceleration is much smaller than for $w = 4.5 \mu\text{m}$, and the vortex takes considerably longer to reach its final equilibrium position. The reason for this behavior can be found in the time evolution of the pseudo-potentials $\phi_{1,2}$ and ϕ_{tot} (see Fig. 7.6 (b)-(d)). Like the vortex deflection, the time evolution of the potentials is qualitatively the same as before. The dynamic process starts with an initial build-up phase of the potential magnitude, followed by a global maximum value, and finally $\phi_{1,2} = \phi_{\text{tot}} = 0$. It can also again be observed that $\phi_1 \approx \phi_{\text{tot}}$ at the beginning of the simulation and $\phi_2 \approx \phi_{\text{tot}}$ in the final phase. If the strip width w is reduced, the magnitude of the potentials is reduced as well. Specifically, a reduction of ϕ_1 in the initial phase leads to a less effective deflection of the vortex in response to the applied temperature field. In addition, the slower vortex motion leads to a longer build up-phase of the potentials, which is translated back into a less effective vortex acceleration. The reason for the geometry dependence of ϕ_1 can be found in a modified temperature distribution due to the shrinking width of the sample. In Fig. 7.5 (e)-(f), one can see that for a given heat source, the iso-contours of constant temperature become more and more elliptic. Due to the reduced volume-to-surface ratio, the boundary condition for T has a greater effect on the bulk properties of the temperature field. This leads to a less effective temperature increase for a given heat source. Consequently, the temperature at the vortex location and the corresponding condensate deformation ∇n_s are reduced, leading to the previously described effects. It should be noted that the system geometry only slightly affects the supervelocity field \mathbf{v}_s in the bulk material. Although the boundary condition (3.2) enforces $\mathbf{v}_s \cdot \mathbf{n} = 0$ at the sample surface, in the vicinity of the vortex, the flow direction of \mathbf{v}_s is unaffected by the value of w (see red circles in Fig. 7.5 (e)-(f)). Therefore, it can be concluded that the geometry dependence of the temperature distribution in the SC is reflected in a modified condensate field deformation. The following decrease of the potential $\phi_1(T(w))$ leads to a less effective vortex deflection.

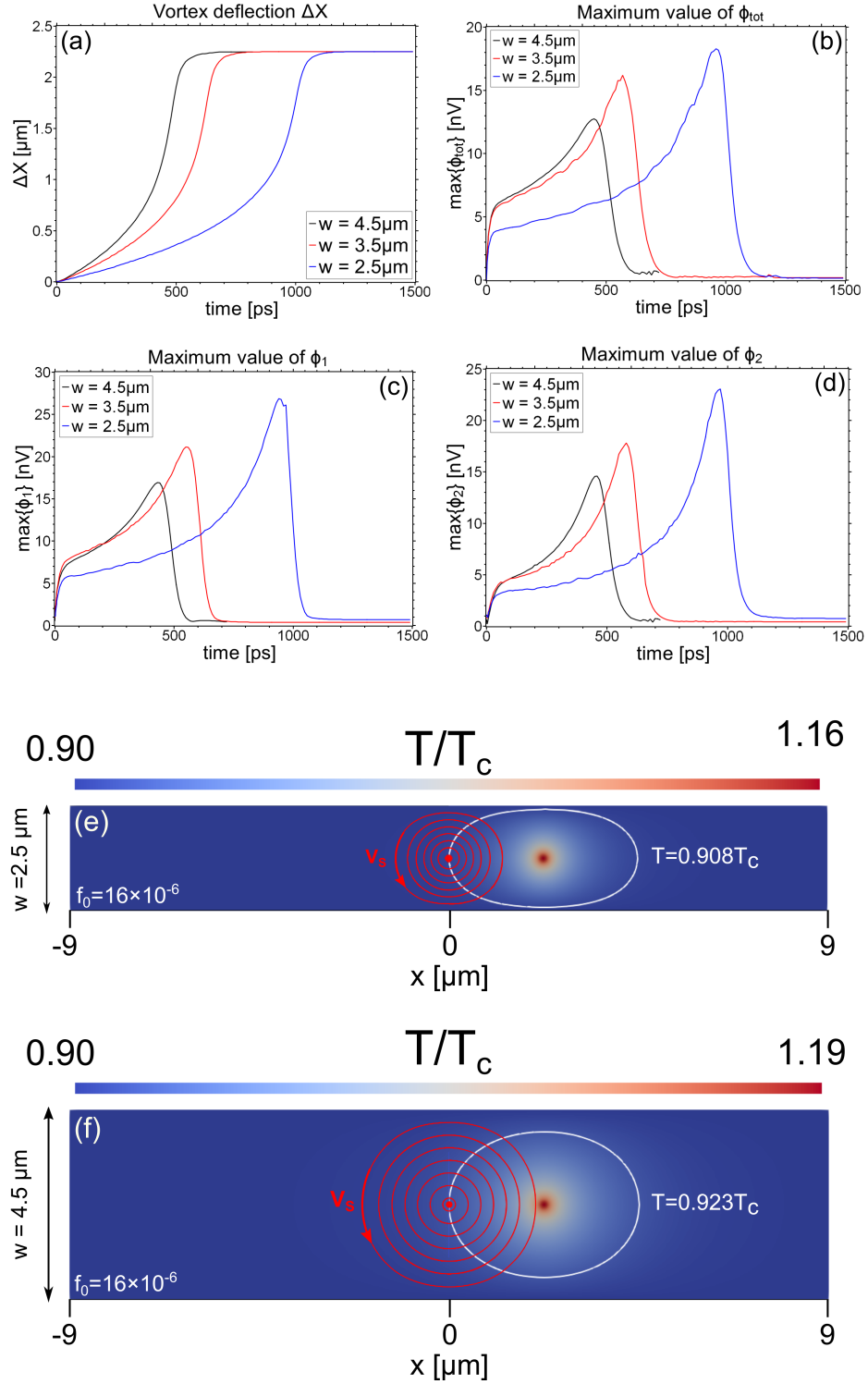


Figure 7.6: (a): Time-dependent deflection ΔX of the vortex along the x -axis due to a hot spot located at $x = 2.25 \mu\text{m}$ for $f_0 = 16 \times 10^{-6}$ and different strip widths w . (b)-(d): Time evolution of the global maximum values of the electric potentials ϕ_1 , ϕ_2 , and ϕ_{tot} . (e)-(f): temperature distribution in the SC for (e): $w = 2.5 \mu\text{m}$ and (f): $w = 4.5 \mu\text{m}$. The white curve corresponds to the iso-contour of T that goes through the center of the vortex. The red curves correspond to the streamlines of \mathbf{v}_s .

7.3 Outlook

In this chapter, it was investigated how isolated fluxons react to the presence of a nearby hot spot. By solving the TDGL equations of superconductivity, it was found that a nonhomogeneous temperature field attracts a nearby vortex and drives the system into non-equilibrium. In this process, the applied temperature gradient enforces a deformation of the condensate field n_s , affecting the supercurrent density such that $\nabla \cdot \mathbf{j}_s \neq 0$. A new interpretation of the diverging current in terms of electric fields allowed a more detailed characterization of the entire dynamic process. Thereby it was found that an interaction of the form $\nabla n_s \cdot \mathbf{v}_s$ acts in an accelerating way on the vortex and draws it closer to the heated region. In close vicinity to the hot spot, the interactions character changes, and now $n_s \nabla \cdot \mathbf{v}_s$ becomes the main driving factor for the fluxon. The here presented results were also interpreted hydrodynamically. In this picture, the deformed condensate field leads to an advection of the superconducting phase driving the vortex into the direction of enhanced temperature. This motion is counterbalanced by the phase field's diffusive nature, avoiding large gradients of the form $\nabla \theta$. The effect of the sample geometry was investigated as well. Thereby it was found that a reduced width of the SC strip hinders the temperature-induced vortex motion. The reason for this behavior is the less effective heating of the sample due to the imposed boundary condition $T = T_0$ simulating effective heat removal from the sample. The effect of other boundary conditions on the system dynamics is still to be investigated.

Another open question regards the presence of external magnetic fields. In the here-presented calculations, $\mathbf{B}_e = 0$ was set, making the vortex state metastable. Applying such a field provides a confining potential for the vortex but can also alter its dynamical behavior. However, even in this case, the results of the main text remain valid. That is because the principle form of the fields \mathbf{v}_s and n_s does not qualitatively change for $\mathbf{B}_e \neq 0$, provided the field is weak enough to prevent additional vortex nucleation. Investigations in this direction are ongoing. In principle, one could also operate with other material parameters. However, as already pointed out, the principle form of the system dynamics is not affected by the specific choice of λ or ξ . The sample geometry is another adjustable parameter. Especially in thin superconducting strips, the interaction of the vortex with the boundary currents could lead to substantial modifications of $\phi_{1,2}$. Finally, it should also be noted that the here-presented results are formally only valid for gapless SCs described by the conventional TDGL equations. For example, in dirty gapped SCs, inelastic electron-phonon scattering can notably alter the vortex dynamics demanding the use of a generalized TDGL-theory [95, 110, 249].

8 Summary and outlook

The overall aim of this research has been to investigate how superconducting vortices behave in closed nanosystems and in the vicinity of a nearby ferromagnet. Specifically, it was searched for novel ways to utilize the fluxons as control elements in FM/SC hybrids, with potential applications in fluxonic memory devices. In addition, the problem of temperature-induced vortex motion was addressed as well. To this end, the following research questions were posed:

- How can a structured FM be used to control superconducting vortices in confined nanosystems;
- How does interfacial Rashba SOC affect the vortex dynamics in a proximity-coupled FM/SC bilayer;
- How can the vortices be utilized to modify the magnonic information flow through the FM/SC hybrid structure;
- How does local heating of the material affect nearby vortices;

The interaction between SCs and FMs is a vast topic with many different aspects. Therefore, four different FM/SC systems were chosen as study objects.

The first research project investigated how the nucleation of superconducting vortices is affected by the presence of a nearby FM. Specifically, the first research question was addressed, i.e., how the FM can be used as a control element for fluxons under strong geometrical confinement. The results of this study indicate that a carefully adjusted FM layer can nucleate well-separated systems of vortices and antivortices in a nearby SC. Thereby the size and orientation of the FM, its distinct domain structure, and its distance from the SC layer strongly affect the distribution and number of generated VAV pairs. Furthermore, it was found that the number and distribution of the fluxons can be precisely controlled under the application of an external magnetic field, allowing basic logic operations.

From a practical point of view, the here investigated system could serve as a precursor for fluxonic memory devices. Thereby, the basic logic operations could be linked to the overall vorticity of the system or the magnetic field distribution above specific locations. The readout could be performed by choosing a suitable vortex imaging technique (see, e.g., [250] and references therein). The here presented results could also find applications in magnonics. For example, the stray field of a fluxon ensemble could be used to modify the spin-wave dispersion in a magnonic waveguide. Thereby, the simultaneous existence of vortices and antivortices could lead to modifications of the band structure that can not be achieved by conventional means. Furthermore, an electric current-assisted, dynamic

modification of the vortex lattice provides an additional way to shape the magnonic dispersion, even in operating mode.

This project is an example of the self-consistent solution of the TDGL equations in extended 3D space and can serve for further studies on coupled FM/SC systems. For example, more realistic results can be achieved by coupling the LLG equation to the TDGL equations allowing a mutual interaction of the system constituents. In this way a dynamic coupling between fluxons and nontrivial magnetic textures, like domain walls or Skyrmions, becomes possible. The here presented results are published in [204].

The second research study addressed how vortex dynamics are affected by interfacial Rashba SOC. Similarly to the first project, this study aimed to use a multiferroic layer to modify and control the vortex dynamics in a superconducting thin film. Thereby both materials were allowed to be in close proximity to each other, allowing a direct coupling of the superconducting phase and the magnetic texture. The resulting supercurrent in the SC was found to be susceptible to changes in the underlying magnetic order of the multiferroic under the application of a small gate voltage. For a first investigation of such a system, TbMnO_3 was chosen, a multiferroic oxide having a Néel-spiral as magnetic texture and a voltage-dependent winding number m . The results of this study indicate that for certain winding numbers, the current-induced vortex motion in the nearby SC is partially inhibited. In contrast, other values of m were observed to foster vortex mobility. Furthermore, by carefully adjusting the winding number m , it was found possible to switch the system from one dynamic regime to the other. The reason for the distinct vortex phases was found in a SOC-induced modification of the energetic barrier for vortex nucleation.

The findings provide a pathway for an all-electrically controlled FM/SC hybrid system with adjustable vortex dynamics. As in the first study, such a structure could find application as a fluxonic memory device. However, in this particular case, the basic logic operations are performed by switching the system from the static to the dynamic regime with the aid of the coupled multiferroic layer. Another interesting observation is a SOC-induced amplification of the critical current of the system. That means that by appropriately adjusting the magnetic layer, it is possible to reduce the energy consumption of the underlying SC.

Note, only the first TDGL equation was solved, which means the effects of the superconducting stray fields are neglected. Future studies should also cover the effects of material impurities and thermal noise since they are expected to affect the here presented results as well. The results of this project are published in [210].

The third research project dealt with the problem of magnon-fluxon interaction in FM/SC hybrids. Specifically, it was investigated how vortices can be utilized to modify the magnonic information flow through the FM/SC hybrid structure (cf. third research question). The idea behind this project was to supplement the recent experimental observation of magnon-fluxon interaction [85] with a theoretical study. To this end, it was attempted to reproduce the experimental results as accurately as possible and to give an interpretation in the framework of micromagnetism. Due to the problem's computational complexity, it was necessary to construct a simplified replacement system where the stray field of a superconducting vortex lattice was replaced with the magnetic field

of an arrangement of ferromagnetic nanodots. The artificial vortex field was then used as input for the LLG equation allowing an insight into the interaction between vortices and spin waves. The results of this study indicate that the static vortex lattice acts as a Bragg grating leading to the formation of forbidden bands in the magnonic spectrum. Furthermore, it was found that the number and width of these bands strongly depend on the strength of the vortex lattice and the geometry of the waveguide. Further findings show that a disordered vortex lattice tends to disrupt the formation of coherent spin waves in the regime of dipolar modes. Also, the stray field of the artificial vortex lattice was observed to confine these modes above the vortex locations leading to a downward shift of the corresponding frequency bands.

The here presented study provides deeper insights into the interaction between magnons and superconducting vortices. However, the experimental results of Dobrovolskiy et al. could not be qualitatively reproduced. It is suspected the main reason for the discrepancy between the numeric results and the experiment lies in a difference between the chosen sample geometries. Solving the LLG equation on a domain of a similar extent as in the experiment would have drastically increased the computation time of the micromagnetic simulations. Therefore the extent of the waveguide had to be reduced. The second important simplification regards the dynamic interaction between the spin waves and the SC system. A more realistic study should consider this interaction by simultaneously solving the LLG and TDGL equations in a realistic setup. In this way also, the interaction of the SC with its own stray field would be adequately taken into account.

Apart from these shortcomings, the here presented study can serve as a foundation for further research on magnon-fluxon interaction. In especially, the construction of the artificial vortex lattice is simple yet effective, allowing even to simulate spin waves in the presence of a current-driven vortex lattice. An extension of this research project in this direction is ongoing. As already discussed, also more complicated vortex patterns, VAV-systems, and superconducting islands can serve as building blocks for magnonic crystals allowing for advanced control of the information flow through the FM/SC hybrid structure. The results of this section are published in [236].

The last research project addressed how an isolated superconducting vortex is affected by the presence of a nearby hot spot. This study was motivated by an existing research gap regarding the dynamic interaction of superconducting vortices with nonhomogenous temperature gradients. In especially, it was investigated how the attractive interaction between the vortex and the heated region manifests itself in the framework of TDGL theory. Thereby, it was found that a local deformation of the superconducting condensate affects the superconducting phase field similarly to a conventional transport current, i.e., the interaction appears in the TDGL equations in the form of a scalar electric potential. Moreover, the corresponding electric field was found to have a complicated space- and time dependency with contributions of the condensate field $n_s(\mathbf{r}, t)$ and the superfluid velocity $\mathbf{v}_s(\mathbf{r}, t)$. The found results can also be interpreted hydrodynamically with the aid of convection-diffusion theory revealing the advection of the superconducting phase as the main driving force for the fluxon. Furthermore, it was found that a reduced width of the chosen SC strip leads to a considerably reduced vortex motion.

The findings of this study are primarily of interest to fundamental research. However, advanced functionalities based on temperature-driven fluxon motion can be easily

conceived. For example, one can consider a scenario where temperature-induced vortex motion affects a nearby system, e.g., a Skyrmion, providing additional control mechanisms for magnetically susceptible systems. In addition, the precise control of individual superconducting vortices is a requirement for applications like fluxonic logic devices. A better insight into the mechanics of temperature-induced vortex motion can help to improve the functionality of such devices.

In this study, no external magnetic fields were applied to the system making the state of an isolated vortex metastable. Also, the material was assumed to be perfectly clean and without structural defects. Future studies should take these problems into account. The effects of different probe geometries and material parameters are also open for future studies. Another way to extend this project would be to investigate the effects of electron-phonon interaction on the vortex motion requiring the solution of a generalized TDGL theory.

Bibliography

- [1] H. K. Onnes, The Superconductivity of Mercury. *Leiden Commun.* **1911**, 120b, 122b, 124c.
- [2] W. Meißner, R. Ochsenfeld, Ein neuer Effekt bei Eintritt der Supraleitfähigkeit. *Naturwissenschaften* **1933**, 21,787-788.
- [3] F. London, H. London, The Electromagnetic equations of the Supraconductor. *Proc. Roy. Soc. Lond.* **1935**, A 149, 71.
- [4] V. L. Ginzburg, L. D. Landau, On the Theory of superconductivity. *Zh. Eksperim. i Theor. Fiz.* **1950**, 20, 1064.
- [5] A. A. Abrikosov, On the magnetic properties of superconductors of the second group. *Sov. Phys. JETP* **1957**, 5, 1174.
- [6] J. Bardeen, L. N. Cooper, and J. R. Schrieffer, Theory of superconductivity. *Phys. Rev.* **1957**, 108, 1175-1204.
- [7] W. S. Corak, B. B. Goodman, C. B. Satterthwaite, A. Wexler, Exponential Temperature Dependence of the Electronic Specific Heat of Superconducting Vanadium. *Phys. Rev.* **1954**, 96, 1442. *Phys. Rev.* **1956**, 102, 656.
- [8] R. E. Glover, M. Tinkham, Conductivity of Superconducting Films for Photon Energies between 0.3 and 40 kT_c . *Phys. Rev.* **1956**, 104, 844. *Phys. Rev.* **1956**, 108, 243.
- [9] R. Doll, M. Näbauer, Experimental Proof of Magnetic Flux Quantization in a Superconducting Ring. *Phys. Rev. Lett.* **1961**, 7, 51.
- [10] B. S. Deaver Jr., W. M. Fairbank, Experimental Evidence for Quantized Flux in Superconducting Cylinders. *Phys. Rev. Lett.* **1961**, 7, 43.
- [11] J. G. Bednorz, K. A. Müller, Possible High T_c Superconductivity in the Ba-La-Cu-O System. *Z. Phys. B* **1986**, 64, 189.
- [12] F. Steglich, J. Aarts, C. D. Bredl, W. Lieke, D. Meschede, W. Franz, H. Schäfer, Superconductivity in the Presence of Strong Pauli Paramagnetism: CeCu_2Si_2 . *Phys. Rev. Lett.* **1979**, 43, 1892–1896.
- [13] Y. Kamihara, H. Hiramatsu, M. Hirano, R. Kawamura, H. Yanagi, T. Kamiya, H. Hosono, Iron-Based Layered Superconductor: LaOFeP . *J. Am. Chem. Soc.* **2006**, 128, 10012–10013.

-
- [14] D. Jerome, A. Mazaud, M. Ribault, K. Bechgaard, Superconductivity in a synthetic organic conductor (TMTSF)₂PF₆. *J. de Phys. Lett.* **1980**, 41.
- [15] Y. Maeno, H. Hashimoto, K. Yoshida, S. Nishizaki, T. Fujita, J. G. Bednorz and F. Lichtenberg, Superconductivity in a layered perovskite without copper. *Nature* **1994**, 372.
- [16] G. R. Steward, Unconventional superconductivity. *Advances in Physics* **2017**, 66:2, 75-196.
- [17] J. Zaanen, S. Chakravarty, T. Senthill, P. Anderson, P. Lee, J. Schmalian, M. Imada, D. Pines, M. Randeria, C. Varma, M. Vojta, M. Rice, Towards a complete theory of high T_c. *Nature Phys.* **2006**, 2, 138–143.
- [18] A. P. Drozdov, P. P. Kong, V. S. Minkov, S. P. Besedin, M. A. Kuzovnikov, S. Mozaffari, L. Balicas, F. F. Balakirev, D. E. Graf, V. B. Prakapenka, E. Greenberg, D. A. Knyazev, M. Tkacz, M. I. Eremets, Superconductivity at 250 K in lanthanum hydride under high pressures. *Nature* **2019**, 569, 528-531.
- [19] M. Somayazulu, M. Ahart, A. K. Mishra, Z. M. Geballe, M. Baldini, Y. Meng, V. V. Struzhkin, R. J. Hemley, Evidence for Superconductivity above 260 K in Lanthanum Superhydride at Megabar Pressures. *Phys. Rev. Lett.* **2019**, 122, 027001.
- [20] C. Yao, Y. Ma, Superconducting materials: Challenges and opportunities for large-scale applications. *iScience* **2021**, 24:6, 102541.
- [21] V. Stanev, C. Oses, A. G. Kusne, E. Rodriguez, J. Paglione, S. Curtarolo, I. Takeuchi, Machine learning modeling of superconducting critical temperature. *npj Computational Materials* **2018**, 4:29.
- [22] A. Y. Aladyshkin, A. V Silhanek, W. Gillijns, V. V. Moshchalkov, Nucleation of superconductivity and vortex matter in superconductor-ferromagnet hybrids. *Supercond. Sci. Technol.* **2009**, 22, 053001.
- [23] A. Y. Aladyshkin, A. I. Buzdin, A. A. Fraerman, A. S. Mel'nikov, D. A. Ryzhov, A. V. Sokolov, Domain-wall superconductivity in hybrid superconductor-ferromagnet structures. *Phys. Rev. B* **2003**, 68, 184508.
- [24] Z. Jing, H. Yong, Y.-H. Zhou, Vortex structures and magnetic domain patterns in the superconductor/ferromagnet hybrid bilayer. *Supercond. Sci. Technol.* **2014**, 27, 10500.
- [25] A. I. Buzdin, Proximity effects in superconductor-ferromagnet heterostructures. *Rev. Mod. Phys.* **2005**, 77, 935.
- [26] D. V. Shopova, D. I. Uzunov, Meissner phases in spin-triplet ferromagnetic superconductors. *Phys. Rev. B* **2005**, 72, 024531.
- [27] O. V. Dobrovolskiy, M. Huth, Crossover from dirty to clean superconducting limit in dc magnetron-sputtered thin Nb films. *Thin Solid Films* **2012**, 520, 5985–5990.

- [28] R. Gross, A. Marx, Festkörperphysik. De Gruyter Oldenbourg, Berlin/Boston, 2. Edition **2014**.
- [29] M. Tinkham, Introduction to superconductivity. Dover Publications, Mineola/New York., Dover, 2. Edition **2004**.
- [30] C. J. Gorter, H. B. G. Casimir, On Superconductivity I. *Physica* **1934**, 1, 306; *Z. Physik*, 35, 963 **1934**, 306; *Z. Techn. Physik*, 15, 539 **1934**.
- [31] F. London, Superfluids. vol I, Wiley, New York, **1950**.
- [32] L. P. Gor'kov, Microscopic derivation of the Ginzburg–Landau equations in the theory of superconductivity. *Sov. Phys. - JETP (Engl. Transl.); (United States)* **1959**, 9:6.
- [33] K. V. Grigorishin, Extended Time-Dependent Ginzburg–Landau Theory. *J. Low. Temp. Phys.* **2021**, 203, 262–308.
- [34] R. A. El-Nabuls, Extended Ginzburg-Landau equations and Abrikosov vortex and geometric transition from square to rectangular lattice in a magnetic field. *Physica C: Superconductivity and its applications* **2021**, 581, 1353808.
- [35] A. A. Shanenko, M. V. Milošević, F. M. Peeters, A. V. Vagov, Extended Ginzburg-Landau Formalism for Two-Band Superconductors. *PRL* **2011**, 106, 047005.
- [36] M. Karmakar, Electrostatic Potential in High-Temperature Superconducting Cuprates: Extended Ginzburg-Landau Theory. *Adv. Cond. Mat.* **2011**, 2011, 493794.
- [37] K. Machida and T. Ohmi, Phenomenological Theory of Ferromagnetic Superconductivity. *Phys. Rev. Lett.* **2001**, 86, 850.
- [38] S. S. Pershoguba, K. Björnson, A. M. Black-Schaffer and A. V. Balatsky, Currents Induced by Magnetic Impurities in Superconductors with Spin-Orbit Coupling. *PRL* **2015**, 115, 116602.
- [39] V. M. Edelstein, The Ginzburg–Landau equation for superconductors of polar symmetry. *J. Phys.: Condens. Matter* **1996**, 8, 339.
- [40] I. S. Aranson and L. Kramer, The world of the complex Ginzburg-Landau equation. *Rev. Mod. Phys.* **2002**, 74, 99.
- [41] V. L. Ginzburg, L. D. Landau, Towards a complete theory of high Tc. *American Journal of Physics* **2019**, 87, 436.
- [42] F. Copie, S. Randoux, P. Suret, The Physics of the one-dimensional nonlinear Schrödinger equation in fiber optics: Rogue waves, modulation instability and self-focusing phenomena. *Reviews in Physics* **2020**, 5, 100037.
- [43] P. G. de Gennes, superconductivity of metals and alloys. W.A. Benjamin, New York **1966**.

-
- [44] A. I. Gubin, K. S. Il'in, S. A. Vitusevich, M. Siegel, N. Klein, Dependence of magnetic penetration depth on the thickness of superconducting Nb thin films. *Phys. Rev. B* **2005**, 72, 064503.
- [45] J. Pearl, Current Distribution in Superconducting Films carrying quantized Fluxoids. *Appl. Phys. Lett.* **1964**, 5, 65.
- [46] Ž. L. Jelić, M. V. Milošević and A. V. Silhanek, Velocimetry of superconducting vortices based on stroboscopic resonances. *Sci. Rep.* **2016**, 6, 35687.
- [47] O. V. Dobrovolskiy, D. Y. Vodolazov, F. Porrati, R. Sachser, V. M. Bevez, M. Y. Mikhailov, A. V. Chumak and M. Huth, Ultra-fast vortex motion in a direct-write Nb-C superconductor. *Nat. Com.* **2020**, 11, 3291.
- [48] F. Antončík, O. Jankovský, T. Hlásek, V. Bartůněk, Nanosized Pinning Centers in the Rare Earth-Barium-Copper-Oxide Thin-Film Superconductors. *Nanomaterials* **2020**, 10, 1429.
- [49] J. I. Martín, M. Vélez, J. Nogués, I. K. Schuller, Flux Pinning in a Superconductor by an Array of Submicrometer Magnetic Dots. *Phys. Rev. Lett* **1997**, 79, 1929.
- [50] V. Metlushko, U. Welp, G. W. Crabtree, Z. Zhang, S. R. J. Brueck, B. Watkins, L. E. DeLong, B. Ilic, K. Chung, P. J. Hesketh, Nonlinear flux-line dynamics in vanadium films with square lattices of submicron holes. *Phys. Rev. B* **1999**, 59, 603.
- [51] L. Civale, A. D. Marwick, T. K. Worthington, M. A. Kirk, J. R. Thompson, L. Krusin-Elbaum, Y. Sun, J. R. Clem, F. Holtzberg, Vortex confinement by columnar defects in $\text{YBa}_2\text{Cu}_3\text{O}_7$ crystals: Enhanced pinning at high fields and temperatures. *Phys. Rev. Lett* **1991**, 67, 648.
- [52] O. Daldini, P. Martinoli, J. L. Olsen, G. Berner, Vortex-Line Pinning by Thickness Modulation of Superconducting Films. *Phys. Rev. Lett* **1974**, 32, 218.
- [53] P. Gammel, Why vortices matter. *Nature* **2001**, 411, 434–435.
- [54] A. Altland, B. Simons, Condensed Matter Field Theory. Cambridge University Press, New York, 2. Edition **2010**.
- [55] D. Varshney, R. K. Singh and S. Shah, Coherence Lengths and Magnetic Penetration Depths in $\text{YBa}_2\text{Cu}_3\text{O}_7$ and $\text{YBa}_2\text{Cu}_4\text{O}_8$ Superconductors. *Journal of superconductivity*, **1996**, 9, 6.
- [56] A. Glatz, V. K. Vlasko-Vlasov, W. K. Kwok, and G. W. Crabtree, Vortex cutting in superconductors. *Phys. Rev. B* **2016**, 94, 064505.
- [57] W. K. Kwok, U. Welp, A. Glatz, A. E. Koshelev, K. J. Kihlstrom and G. W. Crabtree, Vortices in high-performance high-temperature superconductors. *Rep. Prog. Phys.* **2016**, 79, 116501.

- [58] G. R. Berdiyrov, M. M. Doria, A. R. de C. Romaguera, M. V. Milošević, E. H. Brandt, F. M. Peeters, Current-induced cutting and recombination of magnetic superconducting vortex loops in mesoscopic superconductor-ferromagnet heterostructures. *Phys. Rev. B* **2013**, 87, 184508.
- [59] L. Peng, C. Cai, Y. Zhu, L. Sang, Magnetic-Field-Induced Vortices and Antivortices in a Mesoscopic Ferromagnet/Insulator/Superconductor Strip. *J. Low. Temp. Phys.* **2019**, 197, 402-411.
- [60] M. V. Milošević, F. M. Peeters, Vortex–antivortex nucleation in superconducting films with arrays of in-plane dipoles. *Physica C: Superconductivity and its Applications* **2006**, 437–438, 208–212.
- [61] V. N. Gladilin, J. Tempere, J. T. Devreese, W. Gillijns, and V. V. Moshchalkov, Vortex-antivortex pair generation by an in-plane magnetic dipole on a superconducting film. *Phys. Rev. B* **2009**, 80, 054503.
- [62] J. C. Piña, M. A. Zorro, C. C. de Souza Silva, Vortex–antivortex states in nanostructured superconductor–ferromagnet hybrids. *Physica C* **2010**, 470, 762–765.
- [63] M. V. Milošević, F. M. Peeters, Superconducting Wigner vortex molecule near a magnetic disk. *Phys. Rev. B* **2003**, 68, 024509.
- [64] D. A. Frota, A. Chaves, W. P. Ferreira, G. A. Farias, and M. V. Milošević, Superconductor-ferromagnet bilayer under external drive: The role of vortex-antivortex matter. *J. Appl. Phys.* **2016**, 119, 093912.
- [65] R. O. Rezaev, E. I. Smirnova, O. G. Schmidt and V. M. Fomin, Topological transitions in superconductor nanomembranes under a strong transport current. *Com. Phys.* **2020**, 3, 144.
- [66] B. Niedzielski, J. Berakdar, Vortex Ring and Helical Current Formation in Superconductors Driven by a THz-Field-Induced Toroidal Vector Potential. *Phys. Status Solidi (b)* **2022**, 259, 2100622.
- [67] E. H. Fyhn, J. Linder, Controllable vortex loops in superconducting proximity systems. *Phys. Rev. B* **2019**, 100, 214503.
- [68] M. M. Doria, A. R. de C. Romaguera, M. V. Milošević, F. M. Peeters, Threefold onset of vortex loops in superconductors with a magnetic core. *EPL* **2007**, 79, 47006.
- [69] X. H. Chao, B. Y. Zhu, A. V. Silhanek and V. V. Moshchalkov, Current-induced giant vortex and asymmetric vortex confinement in microstructured superconductors. *Phys. Rev. B* **2009**, 80, 054506.
- [70] C. Carballeira, V. V. Moshchalkov, L. F. Chibotaru and A. Ceulemans, Multiquanta Vortex Entry and Vortex-Antivortex Pattern Expansion in a Superconducting Microsquare with a Magnetic Dot. *PRL* **2005**, 95, 237003.

-
- [71] Y. Tanaka, H. Yamamori, T. Yanagisawa, T. Nishio, S. Arisawa, Experimental formation of a fractional vortex in a superconducting bi-layer. *Physica C: Superconductivity and its applications* **2018**, 548, 44-49.
- [72] V. R. Misko, V. M. Fomin, J. T. Devreese and V. V. Moshchalkov, Stable Vortex-Antivortex Molecules in Mesoscopic Superconducting Triangles. *Phys. Rev. Lett.* **2003**, 90, 14.
- [73] G. R. Berdiyrov, M. V. Milošević, F. Kusmartsev, F. M. Peeters, S. Savel'ev, Josephson vortex loops in nanostructured Josephson junctions. *Sci. Rep.*, **2018**, 8, 2733.
- [74] G. Carapella, P. Sabatino, C. Barone, S. Pagano and M. Gombos, Current driven transition from Abrikosov-Josephson to Josephson-like vortex in mesoscopic lateral S/S'/S superconducting weak links. *Sci. Rep.* **2016**, 6, 35694.
- [75] A. Correa, F. Mompeán, I. Guillamón, E. Herrera, M. G.-Hernández, T. Yamamoto, T. Kashiwagi, K. Kadowaki, A. I. Buzdin, H. Suderow and C. Munuera, Attractive interaction between superconducting vortices in tilted magnetic fields. *Com. Phys.* **2019**, 2, 31.
- [76] G.-Q. Zha, F. M. Peeters, S.-P. Zhou, Vortex-antivortex dynamics in mesoscopic symmetric and asymmetric superconducting loops with an applied ac current. *EPL* **2014**, 108, 57001.
- [77] M. V. Milošević, G. R. Berdiyrov, F. M. Peeters, Fluxonic cellular automata. *Appl. Phys. Lett.*, **2007**, 91, 212501.
- [78] T. Golod, A. Iovan and V. M. Krasnov, Single Abrikosov vortices as quantized information bits. *Nat. Commun.*, **2015**, 6, 8628.
- [79] K. Miyahara, M. Mukaida and K. Hohkawa, Abrikosov vortex memory. *Appl. Phys. Lett.*, **1985**, 47, 754-756.
- [80] A. A. Beshpalov, A. S. Mel'nikov, A. I. Buzdin, Magnon radiation by moving Abrikosov vortices in ferromagnetic superconductors and superconductor-ferromagnet multilayers. *Phys. Rev. B*, **2014**, 89, 054516.
- [81] N. I. Polzikova, A. O. Raevskii, Amplification of spin waves by moving magnetic flux vortices in magnet-superconductor layered structure. *Journal of Magnetism and Magnetic Materials*, **1995**, 146, 351-353.
- [82] R. M. Menezes, J. F. S. Neto, C. C. de Souza Silva, M. V. Milošević, Manipulation of magnetic skyrmions by superconducting vortices in ferromagnet-superconductor heterostructures. *Phys. Rev. B*, **2019**, 100, 014431.
- [83] K. M. D. Hals, M. Schechter, M. S. Rudner, Composite Topological Excitations in Ferromagnet-Superconductor Heterostructures. *Phys. Rev. Lett.*, **2016**, 117, 017001.

- [84] S. M. Dahir, A. F. Volkov, I. M. Eremin, Interaction of Skyrmions and Pearl Vortices in Superconductor-Chiral Ferromagnet Heterostructures. *Phys. Rev. Lett.*, **2019**, 122, 097001.
- [85] O. V. Dobrovolskiy, R. Sachser, T. Brächer, T. Böttcher, V. Kruglyak, R. V. Vovk, V. A. Shklovskij, M. Huth, B. Hillebrands, A. V. Chumak, Magnon-fluxon interaction in a ferromagnet/superconductor heterostructure. *Nature Physics* **2019**, 15, 477.
- [86] G. Carneiro, E. H. Brandt, Vortex lines in films: Fields and interactions. *Phys. Rev. B*, **2000**, 61, 6370.
- [87] R. Engel-Herbert, T. Hesjedal. Calculation of the magnetic stray field of a uniaxial magnetic domain. *J. Appl. Phys.*, **2005**, 97, 074504.
- [88] W. A. Little, R. D. Parks, Observation of Quantum Periodicity in the Transition Temperature of a Superconducting Cylinder. *Phys. Rev. Lett.* **1962**, 9, 9.
- [89] R. D. Parks, W. A. Little, Fluxoid Quantization in a Multiply-Connected Superconductor. *Phys. Rev* **1964**, 133, A97.
- [90] B. D. Josephson, Possible New Effects in Superconductive Tunnelling. *Phys. Lett.* **1962**, 1, 251-253.
- [91] A. I. Buzdin, H. Kachkachi, Generalized Ginzburg-Landau theory for non-uniform FFLO superconductors. *Phys. Lett. A* **1997**, 225, 341-348.
- [92] L. Tewordt, Generalized Ginzburg-Landau Theory of Superconducting Alloys. *Phys. Rev.* **1965**, 137, A1745.
- [93] S. Acharjee, U. D. Goswami, Current induced magnetization dynamics and magnetization switching in superconducting ferromagnetic hybrid (F—S—F) structures. *J. Appl. Phys.* **2016**, 120, 243902.
- [94] L. P. Gorkov, G. M. Eliashberg, Generalization of the ginzburg-landau equations for non-stationary problems in the case of alloys with paramagnetic impurities. *Phys. JETP.* **1968**, 27, 16-22.
- [95] R. J. Watts-Tobin, Y. Krähenbühl, L. Kramer, Nonequilibrium theory of dirty, current-carrying superconductors: phase-slip oscillators in narrow filaments near T_c . *J. Low. Temp. Phys.* **1981**, 42(5), 459-501.
- [96] A. Schmid, A time dependent ginzburg-landau equation and its application to the problem of resistivity in the mixed state. *Physik der kondensierten Materie* **1966**, 5(4), 302-317.
- [97] H. Kaper, J. Fleckinger-Pellé, Gauges for the ginzburg-landau equations of superconductivity. *ZAMM - Journal of Applied Mathematics and Mechanics / Zeitschrift für Angewandte Mathematik und Mechanik* **1996**, 76(S2), 305-355.

-
- [98] W. Singer, A. Ermakov, X. Singer, RRR-Measurement Techniques on High Purity Niobium. *TTC-report* **2010**, 02, 305-355.
- [99] C. A. Aguirre, H. B. Achic, J. Barba-Ortega, Inhomogeneous Ginzburg-Landau Parameter in a 2D Mesoscopic Superconductor. *J. Low. Temp. Phys.* **2019**, 195, 124-137.
- [100] C. A. Aguirre, Q. D. Martins, A. S. de Arruda, J. Barba-Ortega, Influence of an applied current on the vortex matter in a superconducting sample with structural defects. *Heliyon* **2019**, 5, 5, e01570.
- [101] A. R. Pack, J. Carlson, S. Wadsworth and M. K. Transtrum, Vortex nucleation in superconductors within time-dependent Ginzburg-Landau theory in two and three dimensions: Role of surface defects and material inhomogeneities. *Phys. Rev. B* **2020**, 101, 144504.
- [102] H. M. Jafri, X. Ma, C. Zhao, H. Huang, T. Anwar, Z. Liu, L.-Q. Chen, Numerical Simulation of Phase Transitions in Type-II Annular Superconductor Using Time-dependent Ginzburg-Landau Equations. *J. Supercond. Nov. Magn.* **2018**, 31, 3445-3451.
- [103] I. Bogush and V. M. Fomin, Topological defects in open superconducting nanotubes after gradual and abrupt switching of the transport current and magnetic field. *Phys. Rev. B* **2022**, 105, 094511.
- [104] V. M. Fomin, R. O. Rezaev and O. G. Schmidt, Tunable Generation of Correlated Vortices in Open Superconductor Tubes. *Nano Lett.* **2012**, 12, 3, 1282-1287.
- [105] I. Mowgood, G. Melkonyan, R. Dulal, S. Teknowijoyo, S. Chahid and A. Gulian, Violation of magnetic flux conservation by superconducting nanorings. *Supercond. Sci. Technol.* **2022**, 35, 045006.
- [106] T. S. Alstrøm, M. P. Sørensen, N. F. Pedersen, S. Madsen, Magnetic Flux Lines in Complex Geometry Type-II Superconductors Studied by the Time Dependent Ginzburg-Landau Equation. *Acta Appl. Math.* **2011**, 115, 63-74.
- [107] J. Tempere, V. N. Gladilin, I. F. Silvera, J. T. Devreese, and V. V. Moshchalkov, Coexistence of the Meissner and vortex states on a nanoscale superconducting spherical shell. *Phys. Rev. B* **2009**, 79, 134516.
- [108] Q. Du, L. Ju, Numerical simulations of the quantized vortices on a thin superconducting hollow sphere. *J. Comp. Phys.* **2004**, 201, 511-530.
- [109] L. Peng, C. Cai, Finite Element Treatment of Vortex States in 3D Cubic Superconductors in a Tilted Magnetic Field. *J. Low. Temp. Phys.* **2017**, 188, 39-48.
- [110] L. B. Horn, pyTDGL: Time-dependent Ginzburg-Landau in Python. *cond-mat.supr-con* **2023**, arXiv:2302.03812.
- [111] V. N. Gladilin, J. Tempere, J. T. Devreese and V. V. Moshchalkov, Aharonov-Bohm oscillations in the vortex dynamics in superconducting hollow cylinders.

- [112] G. R. Berdiyrov, X. H. Chao, F. M. Peeters, H. B. Wang, V. V. Moshchalkov and B. Y. Zhu, Magnetoresistance oscillations in superconducting strips: A Ginzburg-Landau study. *Phys. Rev. B* **2012**, 86, 224504.
- [113] M. Ögren, M. P. Sørensen, N. F. Pedersen, Self-consistent Ginzburg–Landau theory for transport currents in superconductors. *Physica C: Superconductivity*, **2012**, 479, 157-159.
- [114] A. I. Blair, D. P. Hampshire, Time-Dependent Ginzburg–Landau Simulations of the Critical Current in Superconducting Films and Junctions in Magnetic Fields. *IEEE Transactions on Applied Superconductivity*, **2018**, 28, 4.
- [115] R. Rezaev, E. Posenitskiy, E. Smirnova, E. Levchenko, O. G. Schmidt, V. M. Fomin, Voltage Induced by Superconducting Vortices in Open Nanostructured Microtubes. *Phys. Stat. Sol. RRL*, **2019**, 13, 1800251.
- [116] A. V. Silhanek, V. N. Gladilin, J. Van de Vondel, B. Raes, G. W. Ataklti, W. Gillijns, J. Tempere, J. T. Devreese and V. V. Moshchalkov, Local probing of the vortex–antivortex dynamics in superconductor/ferromagnet hybrid structures. *Supercond. Sci. Technol.*, **2011**, 24, 024007.
- [117] Pedro S.-Lotero, D. Domínguez and J. A. Aguiar, Flux flow in current driven mesoscopic superconductors: size effects. *Eur. Phys. J. B*, **2016**, 89, 141.
- [118] A. He, C. Xue, H. Yong and Y. Zhou, The guidance of kinematic vortices in a mesoscopic superconducting strip with artificial defects. *Supercond. Sci. Technol.*, **2016**, 29, 065014.
- [119] J. Barba-Ortega, E. Sardella, J. A. Aguiar, Vortex–Antivortex Dynamics in a Mesoscopic Superconducting Prism with a Centered Antidot. *J. Supercond. Nov. Magn.*, **2011**, 24, 97–100.
- [120] O. V. Dobrovolskiy, C. González-Ruano, A. Lara , R. Sachser, V. M. Bevez, V. A. Shklovskij, A. I. Bezuglyj, R. V. Vovk, M. Huth and F. G. Aliev, Moving flux quanta cool superconductors by a microwave breath. *Com. Phys.*, **2020**, 3, 64.
- [121] J.-Y. Ge, J. Gutierrez, V. N. Gladilin, J. T. Devreese and V. V. Moshchalkov, Bound vortex dipoles generated at pinning centres by Meissner current. *Nat. Com.*, **2015**, 6, 6573.
- [122] G. R. Berdiyrov, S. E. Savel’ev, M. V. Milošević, F. V. Kusmartsev and F. M. Peeters, Synchronized dynamics of Josephson vortices in artificial stacks of SNS Josephson junctions under both dc and ac bias currents. *Phys. Rev. B*, **2013**, 87, 184510.
- [123] G. R. Berdiyrov, M. V. Milošević, A. D. Hernández-Nieves, F. M. Peeters and D. Domínguez, Microfluidic manipulation of magnetic flux domains in type-I superconductors: droplet formation, fusion and fission. *Sci. Rep.*, **2017**, 7, 12129.

-
- [124] Y.-Y. Lyu, J. Jiang, Y.-L. Wang, Z.-L. Xiao, S. Dong, Q.-H. Chen, M.V. Milošević, H. Wang, R. Divan, J. E. Pearson, P. Wu, F. M. Peeters and W.-K. Kwok, Superconducting diode effect via conformal-mapped nanoholes. *Nat. Com.*, **2021**, 12, 2703.
- [125] A. I. Bezuglyj, V. A. Shklovskij, B. Budinská, B. Aichner, V. M. Bevez, M. Yu. Mikhailov, D. Yu. Vodolazov, W. Lang, and O. V. Dobrovolskiy, Vortex jets generated by edge defects in current-carrying superconductor thin strips. *Phys. Rev. B*, **2022**, 105, 214507.
- [126] G. Grimaldi, A. Leo, P. Sabatino, G. Carapella, A. Nigro, S. Pace, V. V. Moshchalkov and A. V. Silhanek Speed limit to the Abrikosov lattice in mesoscopic superconductors. *Phys. Rev. B*, **2015**, 92, 024513.
- [127] A. Al Luhaibi, A. Glatz and J. B. Ketterson, Driven responses of periodically patterned superconducting films. *Phys. Rev. B*, **2022**, 106, 224516.
- [128] S. Savel'ev and F. Nori, Experimentally realizable devices for controlling the motion of magnetic flux quanta in anisotropic superconductors. *Nat. Mat.*, **2002**, 1, 179–184.
- [129] C.-S. Lee, B. Jankó, I. Derényi and A.-L. Barabási, Reducing vortex density in superconductors using the ‘ratchet effect’. *Nature*, **1999**, 400, 337–340.
- [130] A. Kremen, S. Wissberg, N. Haham, E. Persky, Y. Frenkel and B. Kalisky, Mechanical Control of Individual Superconducting Vortices. *Nano Lett.*, **2016**, 16, 3, 1626–1630.
- [131] L. V. Belevtsov, Superconducting vortex-latticed memories. *Microelectronic Engineering*, **2003**, 69, 501-504.
- [132] J. F. Wambaugh, C. Reichhardt, C. J. Olson, F. Marchesoni and F. Nori, Superconducting Fluxon Pumps and Lenses. *Phys. Rev. Lett.*, **2003**, 83, 5106.
- [133] H. M. Jafri, X. Ma, H. Huang, C. Zhao, H. I. A. Qazi, S. B. F. Kazmi, Z. Liu, L. Liu, S.-Q. Shi, Y. Li and L.-Q. Chen, Current assisted memory effect in superconductor–ferromagnet bilayers: a potential candidate for memristors. *Supercond. Sci. Technol.*, **2019**, 32, 095002.
- [134] A. N. Zotova and D. Y. Vodolazov, Photon detection by current-carrying superconducting film: A time-dependent Ginzburg-Landau approach. *Phys. Rev. B*, **2012**, 85, 024509.
- [135] E. D. V. Niño, A. Díaz-Lantada, J. Barba-Ortega, Vortex Matter in a Superconducting Square Under 2D Thermal Gradient. *J. Low. Temp. Phys.*, **2019**, 195, 202–210.
- [136] E. Sardella, A. L. Malvezzi, P. N. Lisboa-Filho and W. A. Ortiz, Temperature-dependent vortex motion in a square mesoscopic superconducting cylinder: Ginzburg-Landau calculations. *Phys. Rev. B*, **2006**, 74, 014512.

- [137] E. C. S. Duarte, A. Presotto, D. Okimoto, E. Sardella and R. Zadorosny, Influence of thermal gradient in vortex states of mesoscopic superconductors. *J. Phys.: Conf. Ser.*, **2014**, 568, 022011.
- [138] E. C. S. Duarte, A. Presotto, D. Okimoto, V. S. Souto, E. Sardella and R. Zadorosny, Use of thermal gradients for control of vortex matter in mesoscopic superconductors. *J. Phys.: Conf. Ser.*, **2019**, 31, 405901.
- [139] I. Shapiro, E. Pechenik and B. Ya. Shapiro, Recovery of superconductivity in a quenched mesoscopic domain. *Phys. Rev. B*, **2001**, 63, 184520.
- [140] I. S. Aranson, N. B. Kopnin and V. M. Vinokur, Nucleation of Vortices by Rapid Thermal Quench. *Phys. Rev. Lett.*, **1999**, 83, 2600.
- [141] J.-Y. Ge, V. N. Gladilin, J. Tempere, C. Xue, J. T. Devreese, J. Van de Vondel, Y. Zhou and V. V. Moshchalkov, Nanoscale assembly of superconducting vortices with scanning tunnelling microscope tip. *Nat. Com.*, **2016**, 7, 13880.
- [142] J. Deang, Q. Du and M. D. Gunzburger, Modeling and Computation of Random Thermal Fluctuations and Material Defects in the Ginzburg–Landau Model for Superconductivity. *J. Comp. Phys.*, **2002**, 181, 45–67.
- [143] G. E. Volovik, Defect formation in inhomogeneous second-order phase transition: theory and experiment. *Physica B*, **2000**, 280, 122-127.
- [144] I. S. Veshchunov, W. Magrini, S. V. Mironov, A. G. Godin, J.-B. Trebbia, A. I. Buzdin, Ph. Tamarat and B. Lounis, Optical manipulation of single flux quanta. *Nat. Com.*, **2016**, 7, 12801.
- [145] A. Rochet, V. Vadimov, W. Magrini, S. Thakur, J.-B. Trebbia, A. Melnikov, A. Buzdin, P. Tamarat and B. Lounis, On-Demand Optical Generation of Single FLUX Quanta. *Nano Lett.*, **2020**, 20, 6488-6493.
- [146] I. S. Burmistrov and N. M. Chitchev, Domain wall effects in ferromagnet-superconductor structures. *Phys. Rev. B*, **2005**, 72, 144520.
- [147] M. V. Milošević and F. M. Peeters, Interaction between a superconducting vortex and an out-of-plane magnetized ferromagnetic disk: Influence of the magnet geometry. *Phys. Rev. B*, **2003**, 68, 094510.
- [148] M. V. Milošević and F. M. Peeters, Vortex-Antivortex Nucleation in Magnetically Nanotextured Superconductors: Magnetic-Field-Driven and Thermal Scenarios. *Phys. Rev. Lett.*, **2005**, 94, 227001.
- [149] A. V. Silhanek, W. Gillijns, M. V. Milošević, A. Volodin, V. V. Moshchalkov and F. M. Peeters, Optimization of superconducting critical parameters by tuning the size and magnetization of arrays of magnetic dots. *Phys. Rev. B*, **2007**, 76, 100502(R).
- [150] A. V. Kapra, V. R. Misko and F. M. Peeters, Controlling magnetic flux motion by arrays of zigzag-arranged magnetic bars. *Supercond. Sci. Technol.*, **2013**, 26, 025011.

-
- [151] M. V. Milošević, F. M. Peeters, Commensurate vortex configurations in thin superconducting films nanostructured by square lattice of magnetic dots. *Physica C: Superconductivity*, **2004**, 404, 246–250.
- [152] S. Kim, C.-R. Hu and M. J. Andrews, Creation and pinning of vortex-antivortex pairs. *Phys. Rev. B*, **2006**, 74, 214511.
- [153] A. Yu. Aladyshkin, D. A. Ryzhov, A. V. Samokhvalov, D. A. Savinov, A. S. Mel'nikov and V. V. Moshchalkov, Localized superconductivity and Little-Parks effect in superconductor/ferromagnet hybrids. *Phys. Rev. B*, **2007**, 75, 184519.
- [154] N. Schildermans, A. Yu. Aladyshkin, A. V. Silhanek, J. Van de Vondel and V. V. Moshchalkov, Different regimes of nucleation of superconductivity in mesoscopic superconductor/ferromagnet hybrids. *Phys. Rev. B*, **2008**, 77, 214519.
- [155] A. Yu. Aladyshkin, A. I. Buzdin, A. A. Fraerman, A. S. Mel'nikov, D. A. Ryzhov and A. V. Sokolov, Domain-wall superconductivity in hybrid superconductor-ferromagnet structures. *Phys. Rev. B*, **2003**, 68, 184508.
- [156] J. D. González, J. L. Aguilar and J. Barba-Ortega, Ferromagnetic/superconducting interface in a hybrid nanoscopic disc. *J. Phys.: Conf. Ser.*, **2015**, 574, 012141.
- [157] A. Buzdin, V. Rayazanov, Inhomogeneous superconductivity in superconductor/ferromagnet heterostructures. *Physica C: Superconductivity and its Applications*, **2007**, 460–462, 238-241.
- [158] M. A. Zorro, T. Saraiva and C. C de Souza Silva, Nucleation of superconductivity in multiply connected superconductor–ferromagnet hybrids. *Supercond. Sci. Technol.*, **2014**, 27, 055002.
- [159] M. V. Milošević, G. R. Berdiyrov and F. M. Peeters, Stabilized vortex-antivortex molecules in a superconducting microdisk with a magnetic nanodot on top. *Phys. Rev. B*, **2007**, 75, 052502.
- [160] Q. Chen, C. Carballeira and V. V. Moshchalkov, Symmetry-breaking effects and spontaneous generation of vortices in hybrid superconductor-ferromagnet nanostructures. *Phys. Rev. B*, **2006**, 74, 214519.
- [161] Q. H. Chen, C. Carballeira and V. V. Moshchalkov, Vortex matter in a hybrid superconducting/ferromagnetic nanostructure. *Phys. Rev. B*, **2009**, 79, 104520.
- [162] D. J. Priour, Jr. and H. A. Fertig, Vortex States of a Superconducting Film from a Magnetic Dot Array. *Phys. Rev. Lett.*, **2004**, 93, 057003.
- [163] Z. Jing, H. Yong and Y. H. Zhou, Vortex structures and magnetic domain patterns in the superconductor/ferromagnet hybrid bilayer. *Supercond. Sci. Technol.*, **2014**, 27, 105005.
- [164] B. Oripov and S. M. Anlage, Time-dependent Ginzburg-Landau treatment of rf magnetic vortices in superconductors: Vortex semiloops in a spatially nonuniform magnetic field. *Phys. Rev. E*, **2020**, 101, 033306.

- [165] A. D. Hernández and D. Domínguez, Dissipation spots generated by vortex nucleation points in mesoscopic superconductors driven by microwave magnetic fields. *Phys. Rev. B*, **2008**, 77, 224505.
- [166] B. Niedzielski, D. Schulz, J. Berakdar, Spatio-temporal superconducting dynamics driven by THz fields from topological spintronic terahertz emitters. *Sci. Rep.*, **2022**, 12, 15610.
- [167] A. Lara , F. G. Aliev, A. V. Silhanek and V. V. Moshchalkov, Microwave-stimulated superconductivity due to presence of vortices. *Sci. Rep.*, **2015**, 5, 9187.
- [168] M. D. Croitoru, S. V. Mironov, B. Lounis and A. I. Buzdin, Toward the Light-Operated Superconducting Devices: Circularly Polarized Radiation Manipulates the Current-Carrying States in Superconducting Rings. *Adv. Quantum. Technol.*, **2022**, 5, 2200054.
- [169] L. Komendová, M. V. Milošević, A. A. Shanenko and F. M. Peeters, Different length scales for order parameters in two-gap superconductors: Extended Ginzburg-Landau theory. *Phys. Rev. B* **2011**, 84, 064522.
- [170] Nigel Goldenfeld, Lectures on Phase Transitions And The Renormalization Group. CRC Press, Boca Raton, 1. Edition **1992**.
- [171] G. Bertotti, I. D. Mayergoyz, C. Serpico, Nonlinear magnetization dynamics in nanosystems. Elsevier Series in Electromagnetism, Elsevier, Oxford, **2009**.
- [172] T. Moriya, Anisotropic Superexchange Interaction and Weak Ferromagnetism. *Phys. Rev.* **1960**, 120, 91.
- [173] A. Aharoni, Introduction to the Theory of Ferromagnetism. Oxford University press, **2007**.
- [174] Y. Tan, K. Liang, Z. Mei, P. Zhou, Y. Liu, Y. Qi, Z. Ma, T. Zhang, Strain induced magnetic anisotropy of high epitaxial Ni thin films grown on different oriented PMN-PT substrates. *Ceramics International* **2018**, 44, 5564-5568.
- [175] F. Nasirpouri, M. R. Sanaeian, A. S. Samardak, E. V. Sukovatitsina, A. V. Ognev, L. A. Chebotkevich, M. G. Hosseini, M. Abdolmaleki, An investigation on the effect of surface morphology and crystalline texture on corrosion behavior, structural and magnetic properties of electrodeposited nanocrystalline nickel films. *Appl. Surf. Sci.* **2014**, 292, 795–805.
- [176] R. C. Wayne, G. A. Samara, R. A. Lefever, Effects of Pressure on the Magnetization of Ferrites: Anomalies Due to Strain-Induced Anisotropy in Porous Samples. *J. Appl. Phys.* **1970**, 41, 633.
- [177] H. C. Siegmann, J. Stöhr, Magnetism - From Fundamentals to Nanoscale Dynamics. Springer-Verlag Berlin Heidelberg **2006**.
- [178] J. M. D. Coey, Magnetism and Magnetic Materials. Cambridge University Press **2010**.

-
- [179] L. D. Landau, E. M. Lifshitz, On the theory of the dispersion of magnetic permeability in ferromagnetic bodies. *Physik. Zeits. Sowjetunion* **1935**, 8, 153–169.
- [180] T. L. Gilbert, A Phenomenological Theory of Damping in Ferromagnetic Materials. *IEEE Trans. Magn.* **2004**, 40, 3443–3449.
- [181] D. D. Stancil, A. Prabhakar, Spin waves - Theory and Applications. Springer New York, NY **2009**.
- [182] S. Neusser, D. Grundler, Magnonics: Spin Waves on the Nanoscale. *Adv. Mater.* **2009**, 21, 2927–2932.
- [183] A. Barman, G. Gubbiotti, S. Ladak, A. O. Adeyeye, M. Krawczyk, J. Gräfe, C. Adelman, S. Cotofana, A. Naeemi, V. I. Vasyuchka et al., The 2021 Magnonics Roadmap. *J. Phys.: Condens. Matter* **2021**, 33, 413001.
- [184] R. A. Gallardo, T. Schneider, A. Roldán-Molina, M. Langer, J. Fassbender, K. Lenz, J. Lindner, and P. Landeros, Dipolar interaction induced band gaps and flat modes in surface-modulated magnonic crystals. *Phys. Rev. B* **2018**, 97, 144405.
- [185] F. Ma, Y. Zhou, H. B. Braun and W. S. Lew, Skyrmion-Based Dynamic Magnonic Crystal. *Nano Lett.* **2015**, 15, 6, 4029–4036.
- [186] R. A. Gallardo, D. Cortés-Ortuño, T. Schneider, A. Roldán-Molina, F. Ma, R. E. Troncoso, K. Lenz, H. Fangohr, J. Lindner, P. Landeros, Flat Bands, Indirect Gaps, and Unconventional Spin-Wave Behavior Induced by a Periodic Dzyaloshinskii-Moriya Interaction. *Phys. Rev. L* **2019**, 122, 067204.
- [187] M. Krawczyk, D. Grundler, Review and prospects of magnonic crystals and devices with reprogrammable band structure. *Journal of Physics: Condensed Matter* **2014**, 26, 123202.
- [188] A. V. Chumak, A. A. Serga and B. Hillebrands, Magnonic crystals for data processing. *J. Phys. D: Appl. Phys.* **2017**, 50, 244001.
- [189] J. Rychły, P. Gruszecki, M. Mruczkiewicz, J. W. Kłos, S. Mamica and M. Krawczyk, Magnonic crystals—Prospective structures for shaping spin waves in nanoscale. *Low Temperature Physics* **2015**, 41, 745–759.
- [190] J. D. Joannopoulos, S. G. Johnson, J. N Winn, R. D. Meade, *Photonic Crystals: Molding the Flow of Light*, 2nd ed.; Dover Publications: **2008** (Princeton, NJ: Princeton University Press).
- [191] M. A. Butt, S. N. Khonina, N. L. Kazanskiy, Recent advances in photonic crystal optical devices: A review. *Optics and Laser Technology* **2021**, 142, 107265.
- [192] W. D. Gropp, H. G. Kaper, G. K. Leaf, D. M. Levine, M. Palumbo, V. M. Vinokur, Numerical Simulation of Vortex Dynamics in Type-II Superconductors. *J. Comp. Phys.* **1996**, 123, 254–266.

- [193] V. V. Baranov, A. G. Balanov, and V. V. Kabanov Current-voltage characteristic of narrow superconducting wires: Bifurcation phenomena *Phys. Rev. B* **2011**, 84, 094527.
- [194] H. Gao, W. Sun, An efficient fully linearized semi-implicit galerkin-mixed fem for the dynamical ginzburg-landau equations of superconductivity. *J. Comp. phys.* **2015**, 294, 329-345.
- [195] M. Alnares, J. Blechta, J. Hake, A. Johansson, B. Kehlet, A. Logg, C. Richardson, J. Ring, M. Rognes, G. Wells, The fenics project version 1.5. *Archive of Numerical Software* **2015**, 3.
- [196] I. A. Sadovskyy, A. E. Koshelev, C. L. Phillips, D. A. Karpeyev, A. Glatz, Stable large-scale solver for Ginzburg–Landau equations for superconductors. *J. Comp. Phys.* **2015**, 294, 639-654.
- [197] C. Geuzaine and J.-F. Remacle, Gmsh: A 3-d finite element mesh generator with built-in pre- and post-processing facilities. *International Journal for Numerical Methods in Engineering* **2009**, 79, 1309-1331.
- [198] A. Logg, K.-A. Mardal, G. Wells, Automated Solution of Differential Equations by the Finite Element Method. Springer Verlag Berlin, Heidelberg, 1. Edition **2012**.
- [199] D. Boffi, F. Brezzi, M. Fortin, Mixed Finite Element Methods and Applications. Springer Verlag Berlin, Heidelberg, 1. Edition **2013**.
- [200] A. Vansteenkiste, J. Leliaert, M. Dvornik, M. Helsen, F. Garcia-Sanchez, B. Waeyenberge, The design and verification of MuMax3. *AIP Advances* **2014**, 4, 107133.
- [201] J. D. Hunter, Matplotlib: A 2D Graphics Environment. *Computing in Science and Engineering* **2007**, 9,3,90-95.
- [202] D. Kumar, O. Dmytriiev, S. Ponraj, A. Barman, Numerical calculation of spin wave dispersions in magnetic nanostructures. *J. Phys. D: Appl. Phys.* **2012**, 45, 015001.
- [203] C. R. Harris, K. J. Millman, S. J. van der Walt, R. Gommers, P. Virtanen, D. Cournapeau, E. Wieser, J. Taylor, S. Berg, N. J. Smith et al., Array programming with NumPy. *Nature* **2020**, 585, 357–362.
- [204] B. Niedzielski, J. Berakdar, Controlled Vortex Formation at Nanostructured Superconductor/Ferromagnetic Junctions. *Phys. Status Solidi (b)* **2020**, 257, 1900709.
- [205] Q. Chen, A. Konrad, A review of finite element open boundary techniques for static and quasi-static electromagnetic field problems. *IEEE Transactions on Magnetics* **1997**, 33 ,663-676.
- [206] M. Iavarone, A. Scarfato, F. Bobba, M. Longobardi, G. Karapetrov, V. Novosad, V. Yefremenko, F. Giubileo, A. M. Cucolo, Imaging the spontaneous formation

- of vortex-antivortex pairs in planar superconductor/ferromagnet hybrid structures. *Phys. Rev. B* **2011**, 84, 024506.
- [207] F. Bobba, C. Di Giorgio, A. Scarfato, M. Longobardi, M. Iavarone, S. A. Moore, G. Karapetrov, V. Novosad, V. Yefremenko, A. M. Cucolo, Vortex-antivortex coexistence in Nb-based superconductor/ferromagnet heterostructures. *Phys. Rev. B* **2014**, 89, 214502.
- [208] M. V. Milošević, F. M. Peeters, Vortex–antivortex molecules induced by a magnetic disk on top of a superconducting film—influence of the magnet geometry. *Physica C* **2004**, 404, 281–284.
- [209] V. V. Moshchalkov, Symmetry-induced vortex patterns. *Europhysics News* **2001**, 32, 176-177.
- [210] B. Niedzielski, C. Jia, J. Berakdar, Supercurrent Induced by Chiral Coupling in Multiferroic/Superconductor Nanostructures. *Nanomaterials* **2021**, 11, 148.
- [211] M. Lange, M. J. Van Bael, V. V. Moshchalkov, Y. Bruynseraede, Magnetic-domain-controlled vortex pinning in a superconductor/ferromagnet bilayer. *Appl. Phys. Lett* **2002**, 81, 322.
- [212] L. N. Bulaevskii, E. M. Chudnovsky, M. P. Maley, Magnetic pinning in superconductor-ferromagnet multilayers. *Appl. Phys. Lett* **2000**, 76, 2594.
- [213] G. R. Berdiyrov, L. R. E. Cabral, F. M. Peeters, Surface barrier for flux entry and exit in mesoscopic superconducting systems. *J. Math. Phys.* **2005**, 46, 095105.
- [214] E. H. Brandt, Geometric edge barrier in the Shubnikov phase of type-II superconductors. *Low Temperature Physics* **2001**, 27, 723.
- [215] A. Benfenati, A. Maiani, F. N. Rybakov, E. Babaev, Vortex nucleation barrier in superconductors beyond the Bean-Livingston approximation: A numerical approach for the sphaleron problem in a gauge theory. *Phys. Rev. B* **2020**, 101, 220505(R).
- [216] G. J. Kimmel, A. G. Glatz, V. M. Vinokur, I. A. Sadovskyy, Edge effect pinning in mesoscopic superconducting strips with nonuniform distribution of defects. *Sci. Rep.* **2019**, 9, 211.
- [217] G. T. Kimura, T. Goto, H. Shintani, K. Ishizaka, T. Arima, Y. Tokura, Magnetic control of ferroelectric polarization. *Nature (London)* **2003**, 426, 55.
- [218] C. Jia, J. Berakdar, Electrically controlled persistent spin currents at the interface of multiferroic oxides. *Phys. Rev. B* **2009**, 80, 014432.
- [219] Y. Yamasaki, H. Sagayama, T. Goto, M. Matsuura, K. Hirota, T. Arima, Y. Tokura, Electric Control of Spin Helicity in a Magnetic Ferroelectric. *Phys. Rev. Lett* **2007**, 98, 147204.
- [220] V. M. Edelstein, Magnetoelectric Effect in Polar Superconductors. *Phys. Rev. Lett.* **1995**, 75, 2004.

- [221] S. K. Yip, Two-dimensional superconductivity with strong spin-orbit interaction. *Phys. Rev. B* **2002**, 65, 144508.
- [222] K. V. Samokhin, Magnetic properties of superconductors with strong spin-orbit coupling. *Phys. Rev. B* **2004**, 70, 104521.
- [223] J. Baumard, J. Cayssol, F. S. Bergeret, A. Buzdin, Generation of a superconducting vortex via Néel skyrmions. *Phys. Rev. B* **2019**, 99, 014511.
- [224] J. W. A. Robinson, A. V. Samokhvalov, A. I. Buzdin, Chirality-controlled spontaneous currents in spin-orbit coupled superconducting rings. *Phys. Rev. B* **2019**, 99, 180501(R).
- [225] L. A. B. O. Olthof, X. Montiel, J. W. A. Robinson, I. A. Buzdin, Superconducting vortices generated via spin-orbit coupling at superconductor/ferromagnet interfaces. *Phys. Rev. B* **2019**, 100, 220505(R).
- [226] E. B. Sonin, Comment on “Ferromagnetic film on a superconducting substrate”. *Phys. Rev. B* **2002**, 66, 136501.
- [227] K. M. D. Hals, Magnetoelectric coupling in superconductor-helomagnet heterostructures. *Phys. Rev. B* **2017**, 95, 134504.
- [228] B. L. T. Plourde, D. J. Van Harlingen, D. Y. Vodolazov, R. Besseling, M. B. S. Hesselberth, P. H. Kes, Influence of edge barriers on vortex dynamics in thin weak-pinning superconducting strips. *Phys. Rev. B* **2000**, 64, 014503.
- [229] C. P. Bean, J. D. Livingston, Surface Barrier in Type-II Superconductors. *Phys. Rev. Lett* **1964**, 12, 14.
- [230] E. Zeldov, A. I. Larkin, V. B. Geshkenbein, M. Konczykowski, D. Majer, B. Khaykovich, V. M. Vinokur, H. Shtrikman, Geometrical Barriers in High-Temperature Superconductors. *Phys. Rev. Lett* **1994**, 73, 1428.
- [231] D. Y. Vodolazov, I. L. Maksimov, E. H. Brandt, Vortex entry conditions in type-II superconductors. Effect of surface defects. *Physica C* **2003**, 384, 211.
- [232] A. D. Hernández, D. Domínguez, Surface barrier in mesoscopic type-I and type-II superconductors. *Phys. Rev. B* **2002**, 65, 144529.
- [233] J. Salafranca and S. Okamoto, Unconventional Proximity Effect and Inverse Spin-Switch Behavior in a Model Manganite-Cuprate-Manganite Trilayer System. *Phys. Rev. Lett.* **2010**, 105, 256804.
- [234] A. Ikushima, T. Mizusaki, Superconductivity in Niobium and Niobium-Tantalum alloys. *J. Phys. Chem. Solids* **1969**, 30, 873-879.
- [235] O. V. Dobrovolskiy, Q. Wang, D. Yu. Vodolazov, B. Budinska, R. Sachser, A. V. Chumak, M. Huth, and A. I. Buzdin, Cherenkov radiation of spin waves by ultra-fast moving magnetic flux quanta. ArXiv:2103.10156.

- [236] B. Niedzielski, C. L. Jia, J. Berakdar, Magnon-Fluxon Interaction in Coupled Superconductor/Ferromagnet Hybrid Periodic Structures. *Phys. Rev. Applied* **2023**, 19, 024073.
- [237] V. K. Vlasko-Vlasov, F. Colauto, A. A. Buzdin, D. Carmo, A. M. H. Andrade, A. A. M. Oliveira, W. A. Ortiz, D. Rosenmann, and W.-K. Kwok, Crossing fields in thin films of isotropic superconductors. *Phys. Rev. B* **2016**, 94, 184502.
- [238] S. J. Chapman, M. D. Gunzburger, and J. S. Peterson, Simplified Ginzburg-Landau type models of superconductivity in the high kappa, high field limit. *Adv. Math. Sci. Appl.* **1995**, 5, 193.
- [239] G. Venkat, D. Kumar, M. Franchin, O. Dmytriiev, M. Mruczkiewicz, H. Fangohr, A. Barman, M. Krawczyk, A. Prabhakar, Proposal for a standard micromagnetic problem: Spin wave dispersion in a magnonic waveguide. *IEEE Transactions on Magnetics* **2013**, 49, 524–529.
- [240] F. R. Morgenthaler, An overview of electromagnetic and spin angular momentum mechanical waves in ferrite media. *Proceedings of the IEEE* **1988**, 76, 138–150.
- [241] H. Puzskarski, M. Krawczyk, Magnonic crystals—the magnetic counterpart of photonic crystals. *Solid State Phenomena* **2003**, 94, 125-134.
- [242] K. Y. Guslienko, B. Hillebrands, S. O. Demokritov, A. N. Slavin, Effective dipolar boundary conditions for dynamic magnetization in thin magnetic stripes. *Phys. Rev. B* **2002**, 66, 132402.
- [243] K. Y. Guslienko, R. W. Chantrell, A. N. Slavin, Dipolar localization of quantized spin-wave modes in thin rectangular magnetic elements. *Phys. Rev. B* **2003**, 68, 024422.
- [244] K.-S. Lee, D.-S. Han, and S.-K. Kim, Physical Origin and Generic Control of Magnonic Band Gaps of Dipole-Exchange Spin Waves in Width-Modulated Nanostrip Waveguides. *Phys. Rev. Lett.* **2009**, 102, 127202.
- [245] S.-K. Kim, K.-S. Lee, D.-S. Han, A gigahertz-range spin-wave filter composed of width-modulated nanostrip magnonic-crystal waveguides. *Appl. Phys. Lett.* **2009**, 95, 082507.
- [246] V. N. Gladilin, J. Gutierrez, M. Timmermans, V. Vondel, J. Tempere, J. T. Devreese, V. V. Moshchalkov, Vortices in a wedge made of a type-I superconductor. *New J. Phys.* **2015**, 17, 063032.
- [247] I. A. Golovchanskiy, N. N. Abramov, V. S. Stolyarov, V. V. Ryazanov, A. A. Golubov, A. V. Ustinov, Modified dispersion law for spin waves coupled to a superconductor. *J. Appl. Phys.* **2018**, 124, 233903.
- [248] I. A. Golovchanskiy, N. N. Abramov, V. S. Stolyarov, V. V. Bolginov, V. V. Ryazanov, A. A. Gobulov, A. V. Ustinov, Ferromagnet/Superconductor Hybridization for Magnonic Applications *Adv. Funct. Mater.* **2018**, 28, 1802375.

- [249] L. Kramer, R. J. Watts-Tobin, Theory of dissipative Current-Carrying states in superconducting filaments. *Phys. Rev. Lett.* **1978**, 40, 1041.
- [250] L. Embon, Y. Anahory, Ž. L. Jelić, E. O. Lachman, Y. Myasoedov, M. E. Huber, G. P. Mikitik, A. V. Silhanek, M. V. Milošević, A. Gurevich and E. Zeldov, Imaging of super-fast dynamics and flow instabilities of superconducting vortices. *Nat. Com.* **2017**, 8, 85.

Curriculum Vitae

Education

- 1998–2002: Primary school
- 2002–2008: Regular school, Petrischule Mühlhausen
- 2008–2011: Grammar school, Thilesius-Gymnasium Mühlhausen
- 2011 -2012: Voluntary social year in a retirement home

Academic Education

- 2012–2015: Physics BSc. Martin-Luther-Universität Halle-Wittenberg
Bachelor Thesis: In-situ Röntgenbeugung an halbleitenden Chalkogenidschichten für die Photovoltaik
(In-situ x-ray diffraction on semiconducting chalcogenide films for photovoltaics)
- 2014 -2015: Semester abroad at the University of Surrey (UK)
- 2015–2018: Physics MSc. Martin-Luther-Universität Halle-Wittenberg
Master Thesis: Dynamics of magnetic/superconducting heterostructures
- since 2018: PhD student at the Martin-Luther-Universität Halle-Wittenberg
- since 2018: Member of the International Max Planck Research School for Science and Technology of Nano-Systems

Halle (Saale), 27.05.2023

List of Publications

1. B. Niedzielski, J. Berakdar, Controlled Vortex Formation at Nanostructured Superconductor/Ferromagnetic Junctions. *Phys. Status Solidi (b)*, **2020**, 257, 1900709.
2. B. Niedzielski, C. Jia, J. Berakdar, Supercurrent Induced by Chiral Coupling in Multiferroic/Superconductor Nanostructures. *Nanomaterials*, **2021**, 11, 148.
3. B. Niedzielski, J. Berakdar, Vortex Ring and Helical Current Formation in Superconductors Driven by a THz-Field-Induced Toroidal Vector Potential. *Phys. Status Solidi (b)*, **2022**, 259, 2100622.
4. B. Niedzielski, D. Schulz, J. Berakdar, Spatio-temporal superconducting dynamics driven by THz fields from topological spintronic terahertz emitters. *Sci. Rep.*, **2022**, 12, 15610.
5. B. Niedzielski, C.L. Jia, J. Berakdar, Magnon-Fluxon Interaction in Coupled Superconductor/Ferromagnet Hybrid Periodic Structures. *Phys. Rev. Applied*, **2023**, 19, 024073.

Acknowledgements

At this point, I want to express my gratitude to everybody who supported me in accomplishing this work.

First, I sincerely thank Prof. Jamal Berakdar, who has already supervised my Master's thesis. He not only provided me with a fascinating research topic but also gave me the opportunity to step into the field of programming and computer simulations. Without his constant support and inspiring ideas, I would not have accomplished this work. I am also very grateful for the high degree of freedom I had in conducting my research.

I want to thank Chenglong Jia for collaborating on several of my research projects. His insights into the physics of micromagnetism and multiferroics were very helpful.

Special thanks also to Huadong Gao and Weiwei Sun, who provided me with a basic code and the solution method for solving the time-dependent Ginzburg-Landau equations. This piece of code helped me a lot in learning the basics of FEniCS and the finite-element method. Moreover, it enabled me to finish not only my Master's thesis but also this project.

I am also thankful for the opportunity to be part of the International Max Planck Research School for Science and Technology of Nano-Systems. I appreciated its support and its various learning opportunities.

Furthermore, I want to thank Siegrid Thon for always being ready to save me from perilous situations, no matter the time of the day.

Finally, I acknowledge the aid from my family. Without their unconditional help and support, this work would have never been finished. They literally saved my life.

Eidesstattliche Erklärung

Hiermit erkläre ich, dass ich die vorliegende Arbeit mit dem Titel "Vortex states in superconducting/ferromagnetic hybrid systems" selbstständig und ohne fremde Hilfe angefertigt habe. Ich habe keine anderen als die von mir gekennzeichneten Quellen und Hilfsmittel verwendet.

Die den verwendeten Werken wörtlich oder sinngemäß entnommenen Stellen wurden als solche gekennzeichnet. Die vorliegende Arbeit wurde noch keiner anderen wissenschaftlichen Einrichtung vorgelegt, weder in der gegenwärtigen Form noch einer anderen.

Weiterhin erkläre ich keine weiteren Promotionsversuche zuvor unternommen zu haben. Gegen mich liegen weder Vorstrafen vor, noch wurden Ermittlungsverfahren eingeleitet.

Halle (Saale), den 27.05.2023

Björn Niedzielski